Beamforming for Radio Astronomy

by

Vereesé van Tonder

Thesis presented in partial fulfilment of the requirements for the degree of Master of Engineering in Electronic Engineering in the Faculty of Engineering at Stellenbosch University

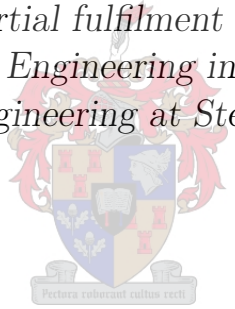

Department of Electrical and Electronic Engineering,
University of Stellenbosch,
Private Bag X1, Matieland 7602, South Africa.

Supervisor: Prof. David B. Davidson

December 2014

Declaration

By submitting this thesis electronically, I declare that the entirety of the work contained therein is my own, original work, that I am the sole author thereof (save to the extent explicitly otherwise stated), that reproduction and publication thereof by Stellenbosch University will not infringe any third party rights and that I have not previously in its entirety or in part submitted it for obtaining any qualification.

Date: 2014/11/24 .....

Abstract

Beamforming for Radio Astronomy

V. van Tonder

Department of Electrical and Electronic Engineering,
University of Stellenbosch,
Private Bag X1, Matieland 7602, South Africa.

Thesis: MEng (Electronic)

December 2014

Beamforming is a technique used to combine signals from an array of antennas to effectively synthesize a single aperture and beam. In the Radio Astronomy community the technique is used to obtain a desirable beam pattern as well as to electronically point the beam of an array. Next generation radio telescopes such as the Square Kilometre Array (SKA) surpass current technology and will extensively make use of beamforming techniques.

Various factors determine the output of a beamformer; however, given an array with a fixed configuration only the weights applied to the incoming signals affect the synthesized aperture and beam. Furthermore, the incoming data must be processed in real-time, at a rate equal to the input-output rate of the processor. Both the weighting function and the real-time implementation of beamforming, are the primary subjects of this thesis.

In this thesis various deterministic weighting functions are investigated. The algorithms are implemented in a MATLAB program, serving as a simulation tool for investigating the techniques. The program is verified by comparing the expected theoretical outcomes to the simulated output. For the program the following functionalities are included: a steering technique, spectral weighting, Dolph-Chebychev, and the Least Square Error algorithm. Applications of these techniques is investigated and their prominence in the Radio Astronomy community is established.

For the real-time beamformer implementation, the UniBoard platform configured with beamformer firmware, is investigated. This is important as the UniBoard is an excellent example of a beamformer implementation within the Radio Astronomy community. The architecture is used to emulate a linear array by implementing a PYTHON control script, where the output corresponded accurately with the expected theoretical values.

The thesis also constitutes the design and implementation of a digital frequency domain beamformer on the ROACH board. This processing board is employed by the Karoo Array Telescope (KAT-7) in South Africa. This work is therefore important as it demonstrates a beamformer implementation on an architecture in use by the Radio Astronomy community. An antenna array is designed and built for the verification of the beamformer design. Results with a good degree of accuracy were obtained and where errors exist they are discussed.

Uittreksel

Bundelvorming vir Radio Astronomie

("Beamforming for Radio Astronomy")

V. van Tonder

Departement Elektriese en Elektroniese Ingenieurswese,
Universiteit van Stellenbosch,
Privaatsak X1, Matieland 7602, Suid Afrika.

Tesis: MIng (Elektroniese)

Desember 2014

Bundelvorming is 'n tegniek waarmee die seine van 'n antenna samestelling gekombineer word om 'n enkele effektiewe stralingsvlak en stralingspatroon te sintiseer. In die Radio Astronomie gemeenskap word die tegniek gebruik om 'n gewenste stralingspatroon te sintiseer sowel as om die rigting van die patroon elektronies te beheer. Die *Square Kilometre Array* (SKA) is 'n toekomstige radioteleskoop en sal grootliks gebruik maak van bundelvorming tegnieke.

Die uitset van bundelvormers word geaffekteer deur verskeie faktore, maar vir 'n gegewe samestelling is dit net die gewigsfunksies wat toegepas word op die inkomende seine wat die gesintiseerde patroon kan beheer. Verder moet die inkomende data verwerk word teen 'n tempo gelykstaande aan die inset-en-uitsetkoers van die verwerker. Die gewigsfunksie so wel as die implementasie van die bundelvormer is albei primêre onderwerpe van die tesis.

'n Verskeindenheid van deterministiese bundelvormingstegnieke sal ondersoek word in hierdie tesis. Die algoritmes is in 'n MATLAB program geïmplementeer vir simulasie doeleindes. Die program is geverifieër deur die uitset te vergelyk met die verwagte teoretiese waardes. Die program sluit die volgende funksies in: 'n rigting beheer algoritme, spektraalgewigte, Dolph-Chebychev, en die minste vierkantsfout algoritme. Hierdie tegnieke is van belang weens hul toepassing in die Radio Astronomie gemeenskap.

Vir die implementasie van 'n bundelvormer is die UniBoard hardeware, geprogrameer in 'n bundelvormings modus, van gebruik gemaak. Hierdie aspek is belangrik omdat die UniBoard 'n goeie voorbeeld van 'n geïmplementeerde bundelvormer in die Radio Astronomie gemeenskap is. Die UniBoard word gebruik om 'n lineêre samestelling te emuleer deur in PYTHON 'n beheer skrip te skryf, waar die uitset van die emuleerder akkuraat ooreenstem met die verwagte waardes.

Die tesis behels ook die ontwerp en implementasie van 'n digitale frekwensiegebied bundelvormer op die ROACH platform. Hierdie verwerker word tans gebruik in die *Karoo Array Telescope* (KAT-7) in Suid-Afrika. Hierdie werk is dus belangrik omdat dit die implementasie van 'n bundelvormer op tegnologie wat huidiglik in die Radio Astronomie gemeenskap gebruik word demonstreer. Daarbenewens is 'n antenna samestelling ontwerp en gebou om die bundelvormer te verifieër. Die resultate is akkuraat tot 'n redelike mate. Waar daar 'n fout onstaan het word dit in die tesis bespreek.

Acknowledgements

I hereby acknowledge and thank the following people and institutions for their contribution, support and advice throughout the project execution,

- My supervisor, Prof David B Davidson, without whom I would have not been able to complete and enjoy my Masters as I did. Specifically for all the insightful and life-broadening experiences I encountered during the execution of the project. I am forever grateful for these as I have learned numerous aspects to a broad range of fields. Furthermore, thank you for providing my funding and for the support and advice throughout the project.
- Jacki Gilmore, soon to be Dr Gilmore, for her invaluable advice on completing Masters, whilst remaining sane. Additionally, for proof-reading the thesis and providing overall support during the execution of the project.
- Dr André Young, for his advice on writing style as well as for proof-reading the thesis. Furthermore, I am thankful for the discussions on beamforming techniques, which provided me with a greater insight of the field.
- Anneke Bester, for her technical support, advice, and assisting me with my measurements.
- Wessel Croukamp, for realizing my antenna array design, twice.
- Dr Dirk IL De Villiers, for his advice on the antenna array configuration and baluns.
- From the DBE team at the SKA SA offices, I want to extend my gratitude toward: Jason Manley, Andrew Martens, Paul Prozesky, Jason Van Aardt, Wesley New and Francois Kapp for their advice, assistance and patiently answering all my 101 questions. Furthermore, for inviting me to their offices and allowing me to use their equipment such that I could conduct my experiments.

- The entire CASPER community for developing the open source software and gateware libraries, which I extensively made use of during the execution of the project.

- I am very grateful to have been able to participate in the MIDPREP exchange program with ASTRON, which I owe to the efforts of Prof Davidson, Dr Jan Geralt bij de Vaate, Truus van den Brink, André van Es, Arno Gregoor and Karin Spijkerman. I truly enjoyed the experience on both a technical and personal level.

- From the DESP department at ASTRON I am appreciative for the assistance I obtained from Leon Hiemstra, Dr Stefan Wijnholds, Harm-Jan Pepping, André Gunst, Eric Kooistra, Gijs Schoonderbeek and Daniel van der Schuur who all ensured I had a successful research visit.

- My ROACH predecessors at Stellenbosch University, Juan-Pierre Jansen van Rensburg and Nicholas Christopher Thompson, for their advice and support on getting started with ROACH.

- Dr Ben Stappers and Prof Davidson, for providing me with funding to attend the CASPER 2013 workshop at the Jodrell Bank Observatory. The workshop enhanced my knowledge of parallel signal processing techniques and its use to overcome the challenges faced by the Radio Astronomy community.

- My friends and colleagues for their advice and support throughout the project.

- My parents, Naomi and Jacques van Tonder, who have worked tirelessly such that I may obtain a good education. Thank you for the unconditional love and support throughout my project.

- My sister, Geomarr van Tonder, for the confidence and enthusiasm she showed toward my project, which encouraged me to work hard when I could not see the light at the end of the tunnel.

- Denzil Büchner, my novio, who always lend an ear and shared his thoughts, aiding me to overcome both technical and personal challenges.

Dedications

I dedicate this thesis to my parents, Jacques and Naomi van Tonder

Contents

Declaration i

Abstract ii

Uittreksel iii

Acknowledgements iv

Dedications vi

Contents vii

List of Figures ix

List of Tables xii

Nomenclature xiii

1 Introduction 1
- 1.1 Background . . . 1
- 1.2 Overview . . . 4

2 Theoretical Framework 6
- 2.1 Introduction . . . 6
- 2.2 Basic Radio Telescope Components . . . 6
- 2.3 Classical Array Theory . . . 12
- 2.4 Beamformer Implementations . . . 24
- 2.5 Conclusion . . . 26

3 Beamforming Techniques 27
- 3.1 Introduction . . . 27
- 3.2 Array Steering Weighting Functions . . . 28
- 3.3 Spectral Weighting . . . 30
- 3.4 Dolph-Chebychev Weighting . . . 41
- 3.5 Least Square Error . . . 45
- 3.6 Applications in Radio Astronomy . . . 48

3.7 Conclusion 50

4 Uniform Linear Array Emulation **51**
4.1 Introduction 51
4.2 APERTIF Project and UniBoard 51
4.3 Implementation Methodology 57
4.4 Verification, Results, and Analysis 59
4.5 Conclusion 63

5 Digital Beamformer Implementation **65**
5.1 Introduction 65
5.2 Antenna Array Design 65
5.3 CASPER Tools for Developing Radio Astronomy Instrumentation 72
5.4 Beamformer Design 77
5.5 Verification, Results, and Analysis 82
5.6 Conclusion 98

6 Conclusion **101**
6.1 Summary 101
6.2 User Perspective on ROACH and UniBoard 102
6.3 Contributions 102
6.4 Recommendations for Future Work 104

Appendices **105**

A Mathematical Definitions **106**
A.1 Modified Bessel Function of the First Kind 106
A.2 Binomial Series Expansion 106
A.3 Complex Gradient 107

B Electromagnetic Theory **108**
B.1 Image Theory 108

List of References **110**

List of Figures

1.1 Electromagnetic spectrum: not to scale . . . 2
1.2 The Lovell radio telescope . . . 2
1.3 The EMBRACE aperture array . . . 4

2.1 Radio telescope components . . . 7
2.2 Bandpass sampling . . . 9
2.3 Comparison of FFT and PFB for channelization . . . 12
2.4 Arbitrary array in the conventional coordinate system . . . 14
2.5 Beamformer topology . . . 16
2.6 Linear array configuration convention . . . 17
2.7 Beam pattern performance metrics . . . 19
2.8 Antenna array network . . . 20
2.9 Effect of array parameters . . . 21
2.10 Effective inter-element spacing . . . 22
2.11 Array steering in θ domain . . . 23
2.12 Array steering in u domain . . . 23

3.1 Overview of deterministic beamforming techniques . . . 28
3.2 Normalized beam pattern for uniform and cosine weighting function 32
3.3 Uniform and cosine weighting functions . . . 32
3.4 Normalized beam pattern for raised cosine weighting functions . . . 33
3.5 Raised cosine weighting functions . . . 34
3.6 Normalized output for cosine^m weighting functions . . . 34
3.7 Cosine^m weighting functions . . . 35
3.8 Normalized beam pattern for Hann, Hamming, and Blackman-Harris weighting functions . . . 36
3.9 Hann, Hamming, and Blackman-Harris weighting functions . . . 36
3.10 Normalized beam pattern for a rectangular array with uniform weights . . . 37
3.11 Normalized output for DPSS weighting functions . . . 38
3.12 DPSS weighting functions . . . 39
3.13 Normalized beam pattern for DPSS and Kaiser weighting functions 40
3.14 Normalized beam pattern for Kaiser weighting functions . . . 40
3.15 Kaiser weighting functions . . . 41

3.16 Broadside linear array . . . 42
3.17 Normalized beam patterns for Dolph-Chebychev weighting functions 44
3.18 Dolph-Chebychev weighting functions . . . 44
3.19 Normalized beam patterns for null constraints . . . 47
3.20 Null-steering weighting functions . . . 48

4.1 The WSRT in the Netherlands . . . 52
4.2 UniBoard hardware layout . . . 54
4.3 Node connections via the high speed mesh . . . 55
4.4 UniBoard beamformer firmware description . . . 56
4.5 Interfaces between the client, UniServer, and UniBoard . . . 57
4.6 Flowchart of emulated beamformer . . . 60
4.7 Varying the inter-element spacing . . . 62
4.8 Varying the direction of the incoming signal . . . 62
4.9 Varying the operating frequency . . . 63

5.1 Helix antenna radiation pattern at 600MHz in $\phi = 90°$ direction . . . 67
5.2 Dipole with $\frac{\lambda}{4}$ balun . . . 69
5.3 Half wavelength dipole antenna radiation pattern at 600MHz in $\phi = 90°$ direction . . . 69
5.4 Three dimensional radiation pattern of the antenna array . . . 70
5.5 Antenna array radiation pattern at 600MHz in $\phi = 90°$ direction . . . 70
5.6 Antenna array steered towards $\theta = \pm 20°$ . . . 71
5.7 Antenna array configuration . . . 72
5.8 Block diagram of KATADC . . . 74
5.9 Block diagram of ROACH . . . 76
5.10 Nyquist zones for $f_s = 800$MHz sampling rate . . . 78
5.11 Beamformer pipeline design . . . 80
5.12 Flowchart of beamformer steering . . . 83
5.13 Top view of anechoic chamber . . . 85
5.14 Active reflection coefficient of elements with $l = 250$mm . . . 86
5.15 Coupling between elements with $l = 250$mm . . . 86
5.16 Active reflection coefficient of elements with $l = 230$mm . . . 87
5.17 Coupling between elements with $l = 230$mm . . . 87
5.18 Measured gain of antenna array . . . 89
5.19 Measured beam pattern of antenna array . . . 90
5.20 Measured DBE gain . . . 91
5.21 Measured DBE SFDR . . . 92
5.22 Beamformer output for different inter-element spacings . . . 93
5.23 Experimental setup for design verification . . . 94
5.24 Beamformer output for different source directions . . . 94
5.25 Wide-band frequency profile of noise source . . . 95
5.26 Wide-band beamformer output . . . 95
5.27 A side view of the experimental setup in the anechoic chamber . . . 96

5.28 Beamformer output for three source directions 97
5.29 Experiment one results 98
5.30 Beamformer output for three beamformer pointing directions 99
5.31 Experiment two results 99

B.1 Electric sources above a PEC and their equivalent systems 109

List of Tables

2.1 Summary of domain definitions 17

4.1 Hardware setup 58
4.2 Default parameters 59
4.3 Calculated and measured quantities 61

5.1 Helix antenna dimensions 67
5.2 Half wavelength dipole antenna dimensions 69
5.3 Antenna array dimensions 71
5.4 KATADC component details 73
5.5 ROACH component details 74
5.6 Gain measurement setup 88
5.7 Measured beam pattern results 89
5.8 Beamformer output results 92
5.9 Cable phase introduced with corresponding lengths 93

Nomenclature

Acronyms

2-PAD	2-Polarization All Digital
ADC	Analogue-to-Digital Converter
AFE	Analogue Front-End
ALMA	Atacama Large Millimeter Array
APERTIF	Aperture Tile In Focus
ASKAP	Australian SKA Pathfinder
BEE	Berkeley Emulation Engine
BN	Back Node
BORPH	Berkeley Operating system for Re-Programmable Hardware
BRAM	Block Random Access Memory
BSN	Block Sequence Number
BW_{NN}	Beamwidth between first Nulls
CMBR	Cosmic Microwave Background Radiation
CASPER	Collaboration for Astronomy Signal Processing and Electronics Research
CLB	Configurable Logic Block
CMAC	Complex Multiplication and Accumulation
CMT	Clock Management Tile
DBE	Digital Back-End
DCM	Digital Clock Manager
DDR	Double Data Rate
DFT	Discrete Fourier Transform
DIMM	Dual In-line Memory Module
DPSS	Discrete Prolate Spheroidal Sequence
DSP	Digital Signal Processing
EBC	External Bus Control
EMBRACE	Electronic Multi-Beam Radio Astronomy ConcEpt
FFT	Fast Fourier Transform
FIR	Finite Impulse Response

FPGA	Field Programmable Gate Array
FN	Front Node
GOPS	Giga Operations per Second
GPIO	General Purpose Input output
GPU	Graphics Processing Unit
HPBW	Half-Power Beamwidth
IBOB	Interconnect Break-Out Board
IO	Input-Output
JIVE	Joint Institute for VLBI in Europe
KATCP	Karoo Array Telescope Control Protocol
LCU	Local Control Unit
LNA	Low Noise Amplifier
LOFAR	Low Frequency Array
LPDA	Log-Periodic Dipole Antenna
LSE	Least Square Error
LUT	Look Up Table
LVDS	Low-Voltage Differential Signaling
MeerKAT	Meer-Karoo Array Telescope
MoM	Method of Moment
MWA	Murchison Wide-field Array
NRAO	National Radio Astronomy Observatory
PAF	Phased Array Feed
PD	Power Divider
PEC	Perfect Electrical Conductor
PFB	Polyphase Filter Bank
PLL	Phase Locked Loop
PPS	Pulse Per Second
PTFE	Polytetrafluoroethylene
QDR	Quad Data Rate
RF	Radio Frequency
RFI	Radio Frequency Interference
ROACH	Reconfigurable Open Architecture Computing Hardware
RX	Receive
SDR	Software Defined Radio
SFDR	Spurious Free Dynamic Range
SG	Signal Generator
SKA	Square Kilometre Array

SLL	Side Lobe Level
SNR	Signal-to-Noise Ratio
SODIMM	Small Outline Dual In-line Memory Module
SPF	Single Pixel Feed
SRAM	Static Random Access Memory
TCP	Transmission Control Protocol
TMAC	Tera Multiplications and Accumulations
TX	Transmit
UDP	User Datagram Protocol
UniBoard	Universal Board
VLBI	Very Long Baseline Interferometry
VNA	Vector Network Analyzer
VSWR	Voltage Standing Wave Ratio
WSRT	Westerbork Synthesis Radio Telescope
XPS	Xilinx Platform Studio

Constants

c =	$2.998\frac{\mathrm{m}}{\mathrm{s}}$
π =	3.141592654

Notations

A_{eff}	Effective aperture area
a_r	Antenna wire radius
$\mathbf{a}_n$	Antenna element position
AF	Array factor
$\mathbf{b}$	Source direction
b_d	Number of bits used to digitize the signal
b_r	Number of bits used to re-quantize the signal
bl	Beamlet
B	Beam pattern
B_e	Element beam pattern
BW	Bandwidth
C	Circumference
d	Inter-element spacing
d_a	Distance between transmit and receive antennas
D	Directivity
E	Electric field

e_a	Antenna efficiency factor
f	Frequency
f_b	Frequency bin
FoV	Field of view
G	Gain
h	Height
ib	Iblet
I_m	Modified Bessel function of the first kind
$\mathbf{k}$	Wavenumber
l	Length
L	Losses
n	Element index
N	Number of elements
N_{acc}	Number of accumulations
N_b	Number of beams
N_S	Number of samples
N_{tap}	Number of taps
P	Power
q	Time domain signal
q_d	Time series signal
Q	Frequency domain signal
Q_d	Frequency series signal
$\mathbf{S}$	Scattering matrix
SS	Survey speed
t	Time
t_d	Discrete time
T_m	Dolph-Chebyshev polynomial function
T_{sync}	Minimum sync period
T_{sys}	System temperature
T	Period
U	Radiation Intensity
$\boldsymbol{u}$	Directional cosine unit
$\mathbf{v}$	Array manifold vector
$\mathbf{w}$	Weight vector
x	Rectangular coordinate
y	Rectangular coordinate
Y	Output signal

z	Rectangular coordinate
Z	Impedance
β	Phase
ε	Error function
δ	Impulse function
τ	Time delay
θ	Polar angle
ϕ	Azimuth angle
λ	Wavelength
λ_e	Eigenvalue
$\boldsymbol{\lambda}$	Lagrange multiplier
ω	Frequency
Ω	Solid angle
Γ	Reflection coefficient
^{H}	Hermitian transpose
*	Complex conjugate

Chapter 1

Introduction

1.1 Background

Radio Astronomy is the science of studying celestial objects radiating electromagentic energy at radio wavelengths. The radio window, accessible for ground based Radio Astronomy, extends approximately from 30MHz to 3THz as depicted in Figure 1.1. Many astronomers and physicists in the late 19^{th} century predicted the existence of extraterrestrial radio sources. However, it was not until 1932 when Karl Jansky inadvertently discovered the first radio waves from cosmic sources. Jansky discovered electromagnetic radiation from the Milky Way whilst conducting research on transatlantic interference for Bell Telephone Laboratories. His discovery, published in his classic paper titled *Electrical Disturbances Apparently of Extraterrestrial Origin* [1], sparked an interest in the field which only escalated after WWII [2].

A wide range of phenomena have been discovered since, including the presence of hydrogen in outer space. When an electron in a hydrogen atom changes its spinning direction, relative to the proton, energy is radiated at 1420.406MHz. By mapping the universe's hydrogen, astronomers affirmed that some galaxies have spiral structures. Another exciting astronomical breakthrough was the discovery of pulsars by Dame Jocelyn Bell-Burnell in 1967. Pulsars are extremely dense neutron stars which rotate rapidly with an accurate period. Due to their accuracy, pulsars are used as a timing tool and in the future may act as a navigational system for spacecraft [3]. Furthermore, remnants of the big bang, referred to as Cosmic Microwave Background Radiation (CMBR), have been detected [2]. Behind these scientific discoveries lies a radio telescope, the instrument responsible for capturing the cosmic signals.

Traditional radio telescopes consists of large dish antennas, such as the 76m Lovell radio telescope at Jodrell Bank, seen in Figure 1.2. Large diameters are required to resolve radio sources at longer wavelengths. Celestial radio sources are very faint and a large collecting area is needed to detect the signals. The infeasibility of constructing larger dishes and the demand for higher resolution

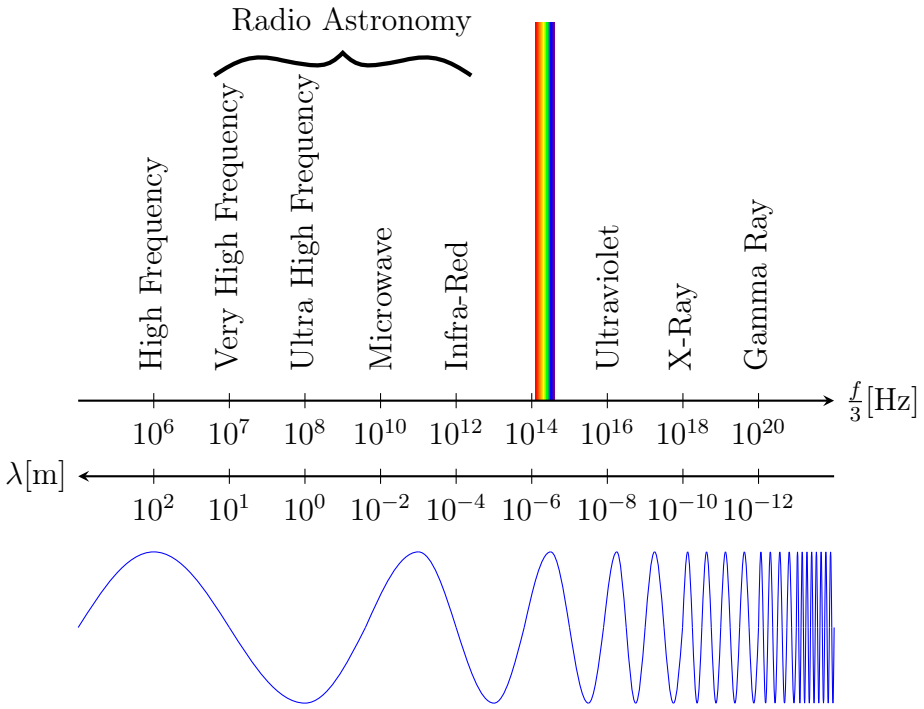

Figure 1.1: Electromagnetic spectrum: not to scale

and sensitivity led to the development of interferometric techniques.

Figure 1.2: The Lovell radio telescope

Interferometry uses an array of antennas to effectively synthesize a large aperture with an increased sensitivity and resolution. Antenna elements in the array detect a source signal and by making use of digital signal processing algorithms, the signals from individual antennas are combined. The recently constructed Atacama Large Millimeter Array (ALMA), is based on this technique. ALMA consists of 54×12m and 12×7m steerable dish antennas and operates at the higher frequency edge of the radio window [4].

At lower frequencies (longer wavelengths), it becomes increasingly difficult to construct steerable radio telescopes due to mechanical limitations. Antennas are electrically smaller due to construction constraints and therefore have wider beams. Wider beams are beneficial, since they allow for electronic steering. Therefore, at lower frequencies fixed omni-directional antennas along with algorithms to electronically steer a synthesized beam, are used. These algorithms are termed beamforming techniques and the Low Frequency Array (LOFAR) is an example of a radio telescope which makes use of the technique [5].

The LOFAR radio telescope is one of the pathfinders for the Square Kilometre Array (SKA), which is an international endeavor to construct the world's largest radio telescope. Full system requirements include a collecting area of one square kilometre in the frequency range $0.7-30$GHz. This will be achieved by constructing four radio telescopes: a high frequency dish array fitted with Single Pixel Feeds (SPF); a dish array fitted with Phased Array Feed (PAF) technology; a mid-frequency dense aperture array; and a low-frequency sparse aperture array. These radio telescopes will be constructed in two phases where precursor projects are currently underway [6].

For the SKA phase one high frequency dish array, 254 reflector-type antennas will be constructed in the Karoo region of South Africa. This will include the Meer-Karoo Array Telescope (MeerKAT) pathfinder, which will consist of 64 Offset Gregorian antennas each fitted with a wide-band SPF [7] [8]. The Australian SKA Pathfinder (ASKAP) is a radio telescope consisting of 36 dish antennas, fitted with PAF technology. ASKAP is located in the Murchison region of Australia and will be extended to 96 dishes, serving as a survey instrument for SKA phase one [8] [9].

Also to be located in the Murchison region is the low-frequency sparse aperture array. Current specifications are set to include 250 arrays each with a 180m diameter operating across a frequency range of $70 - 450$MHz [10]. Furthermore, the dense aperture array will be situated in the Karoo region and according to [10] will operate in the mid-frequency range between $0.4-1.4$GHz. A total of 250 arrays will be constructed, where each station will have a 56m diameter and be fitted with 75 000 dual polarized elements [10].

From these figures the processing demands of the SKA is evident, especially for the low and mid-frequency arrays. Both the aperture arrays will therefore extensively make use of beamforming strategies to reduce the data output. This will be achieved by hierarchically combing data at a tile level before

combination at a station level [10]. The feasibility of beamforming techniques is currently being demonstrated by various SKA pathfinders such as LOFAR [5], the Murchison Wide-field Array (MWA) [11], and the Electronic Multi-Beam Radio Astronomy Concept (EMBRACE) aperture array [12], see Figure 1.3.

Figure 1.3: The EMBRACE aperture array

A beamformer configures, and optionally directs, the beam of an array. Beamforming is achieved by appropriately weighting and summing the signals from the antennas in the array. The subject of beamforming consists of *a*) computing the necessary weights, for example as demonstrated by [13] and [14] for PAF technology; and *b*) processing data in real-time. The large amounts of data produced by a radio telescope is the primary motivation for research into accelerating real-time processes such as beamforming. Beamformers have been implemented in both analog and digital domains where the aspects of these are detailed in [15]. Research showed the viability of implementing beamformer topologies on Graphics Processing Units (GPU) [16], fixed-point digital signal processors, and Field Programmable Gate Arrays (FPGA) [17]. A subset of both the beamforming aspects discussed above, with respect to Radio Astronomy, will be investigated throughout the thesis.

1.2 Overview

The main aim of this work was to establish expertise with beamforming for Radio Astronomy at Stellenbosch University. To this end, this thesis will address both theoretical issues regarding beamforming, as well as practical issues including the Analogue Front-End (AFE) and Digital Back-End (DBE). The latter in particular is heavily dependent on current technology, and one of the main aims of the thesis was to comprehensively investigate implementations using two contemporary FPGA based DBEs, namely the Universal Board

(UniBoard) and the Reconfigurable Open Architecture Computing Hardware (ROACH) board. As such, specifications will not be tied to a specific system, but the focus will rather be on establishing the capability of current representative DBE FPGA technology. A complete four channel system including both the AFE and DBE is also implemented and measured to evaluate the capability developed.

The theoretical framework needed throughout the thesis will first be developed in Chapter 2. In this Chapter the basic radio telescope components will be considered as well as classical array theory and concludes by discussing the various beamformer implementations. Additionally, the Chapter provides a motivation for the scope of the thesis and defines the conventions which will be employed.

In Chapter 3 the simulation and theory of appropriate weighting functions will be discussed. This includes beam steering, as well as techniques to obtain a desirable synthesized beam. An overview of the applications of these techniques will also be provided, with respect to the Radio Astronomy community.

The implementations discussed in Chapters 4 and 5 are concerned with the real-time data processing techniques employed by beamformers. Initially the UniBoard is considered and is an example of cutting edge beamformer technology developed by the Radio Astronomy community. In this thesis, the UniBoard is used to emulate a linear array which is detailed in Chapter 4. A beamformer topology is then designed and implemented using the ROACH board, which is an example of technology currently in use by radio observatories. Additionally, an antenna array is used for the verification of the beamformer implemented on ROACH. The design and verification of both the antenna array and the beamformer will be detailed in Chapter 5.

The thesis concludes with a summary in Chapter 6. Additionally, the differences and similarities between the ROACH and UniBoard will be discussed from a user perspective. This Chapter also lists the contributions of the project. Finally, recommendations for future work will be considered.

Chapter 2

Theoretical Framework

2.1 Introduction

This Chapter serves as a theoretical framework, as well as a motivation for the scope of the thesis. Motivations for the scope will be highlighted in the relevant Sections. Additionally, this Chapter develops the theory and defines the conventions which will be used throughout the thesis.

Initially, an overview of the primary components of a radio telescope will be presented in Section 2.2. For this thesis, the DBE of a radio telescope is of more importance. Therefore Section 2.2 will focus primarily on the DBE components, relevant to this thesis.

Section 2.3 discusses classical array theory for both an arbitrary and linear array configuration. Various performance metrics, employed by later Chapters of the thesis, will be defined and analyzed in this Section.

The various beamformer implementation strategies will be discussed in Section 2.4 and motivation for the chosen strategy will be provided.

2.2 Basic Radio Telescope Components

Figure 2.1 depicts the basic components of a radio telescope. Modern day radio telescopes makes use of an array of antennas, to effectively synthesize a much larger instrument. As mentioned earlier, the fundamental concepts of array theory will be developed in Section 2.3.

Electromagnetic radiation from celestial sources induce a current distribution across the antenna elements. Thereafter the signals are transmitted to the AFE chain via coaxial or optical fiber cables.

The AFE consists of Low Noise Amplifiers (LNA) and filters, providing frequency selectivity and amplification of the faint astronomical signals. Radio sources are typically broad-band noise signals, with statistical properties similar to the noise generated in the AFE. Therefore radio telescopes must be cooled to ensure a low system temperature.

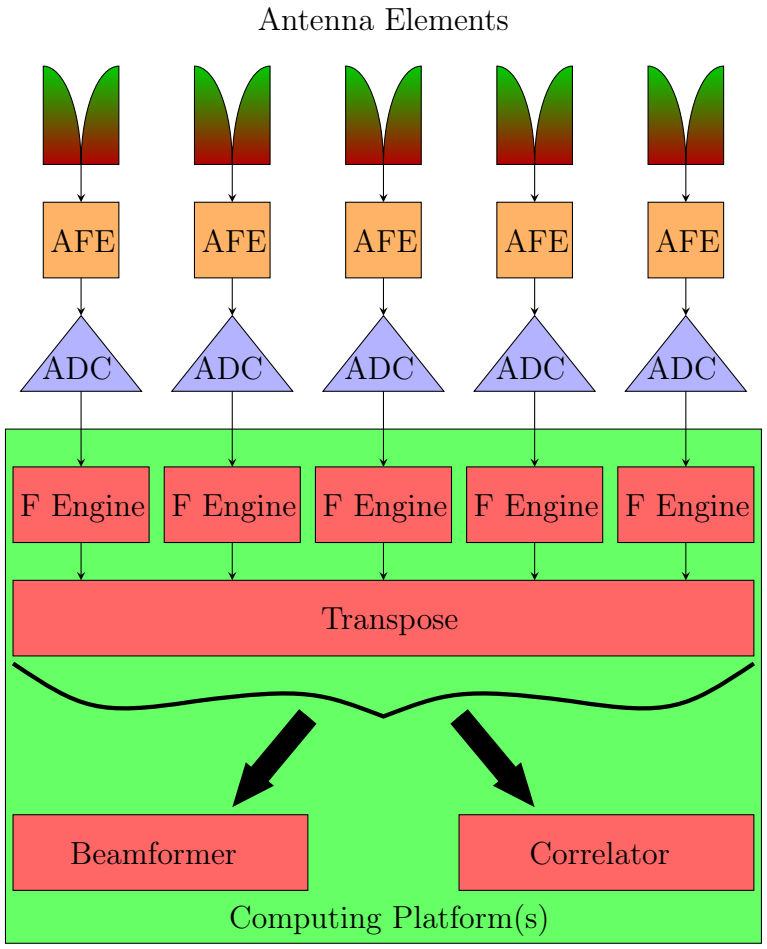

Figure 2.1: Radio telescope components

The signals must be down-converted to a lower frequency, prior to digitization using an Analog-to-Digital Converter (ADC). Traditionally this consists of multiplying the incoming signals with a local oscillator to mix the signal down to a lower frequency. However, some modern day radio telescopes employ bandpass sampling for down-converting the source signal. The MeerKAT radio telescope will use this down-conversion scheme to digitize signals at the feed [18]. This concept was used during the execution of the project. The underlying theory of bandpass sampling will therefore be discussed in Subsection 2.2.1.

After digitization the signals are transmitted to a computing platform, for digital signal processing (DSP). Various hardware platforms are used within the Radio Astronomy community and the cores of the architectures will be discussed in Subsection 2.2.2.

Channelization is one of the first components within the digital signal processing chain and is referred to as the *F Engine* in Figure 2.1. The data is split

into multiple frequency sub-bands for further processing. This may be accomplished using the Fast Fourier Transform (FFT). A more efficient approach is the Polyphase Filter Bank (PFB) technique and most radio telescopes make use of this method. The PFB approach to channelization was employed during project execution and is therefore discussed in Subsection 2.2.3.

Radio Astronomy instrumentation has the need to transpose data between full bandwidth for one antenna, to a subset of channelized data for all antennas. Consider the following hypothetical example. There are five antennas, with each respective *F Engine* node producing five sub-bands. The sub-bands must be transposed to a node, which contains one sub-band but for five antennas. This action may be completed on the computing platform, or between multiple platforms using backplanes or 10GbE switches [19].

Further processing depends on the science case behind the observation. However, most science cases requires that the signals from the antennas be combined. Two widely used combination methods for Radio Astronomy are correlation and beamforming. A correlator multiplies each incoming signal, with every other incoming signal. Therefore, correlation is typically used to produce a two dimensional image of the sky. Beamforming is the coherent summation of the incoming signals, resulting in a single beam. This may be done multiple times, forming multiple artificial beams on the sky [20]. Beamforming is not limited to the frequency domain as depicted in Figure 2.1 and alternative beamformer implementations will be discussed in Section 2.4.

2.2.1 Bandpass Sampling

Bandpass sampling uses the inherit down-conversion properties of an ADC to translate an incoming signal to a lower frequency. Figure 2.2 depicts the process for a source signal at $f_{RF} = 1.4$GHz with a 400MHz bandwidth BW, sampled at $f_s = 800$MHz.

Sampling at Nyquist rate requires very high sampling rates, due to the Nyquist criterion

$$f_s = 2f_u\,, \tag{2.2.1}$$

where f_u is the highest frequency component in the signal. This also results in unmanageable data rates. Bandpass sampling reduces the data rate by sampling at a rate less than the Nyquist rate. Therefore the incoming signal and information bandwidth is intentionally aliased [21].

A source with its lower frequency edge f_l positioned at

$$f_l = i(f_u - f_l), \quad i = 0, 1, 2, \cdots\,, \tag{2.2.2}$$

where i is an integer value from the origin, has a minimum bandpass sampling rate of $f_{s_{min}}$ given by

$$f_{s_{min}} = 2BW\,. \tag{2.2.3}$$

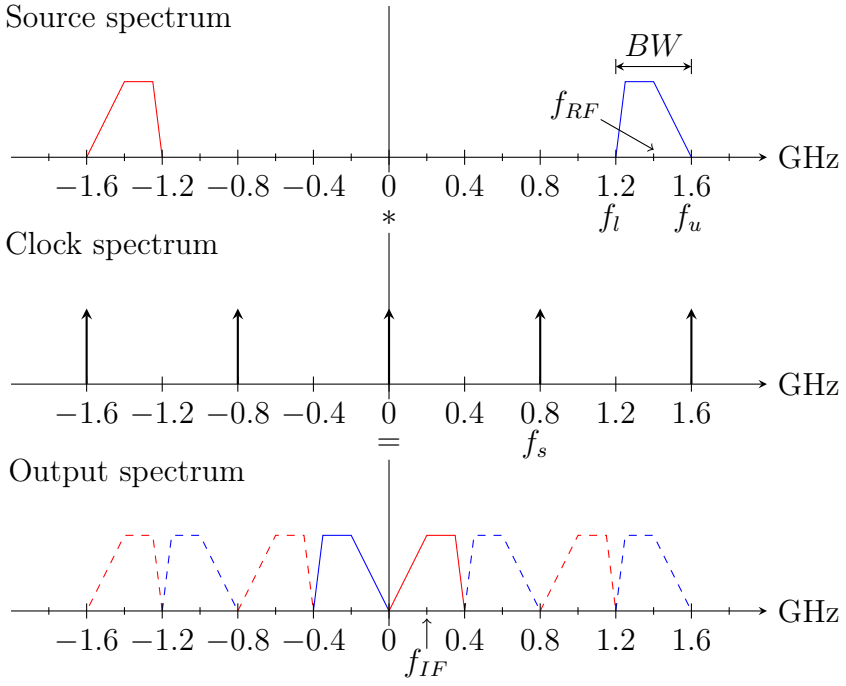

Figure 2.2: Bandpass sampling

To use $f_{s_{min}}$, the signal may not have frequency components at f_l or f_u. For an even integer positioned band, the positive frequency content is translated to baseband. As for the case depicted in Figure 2.2, the negative frequency content is translated to baseband because the band is positioned at an odd integer from the origin [21].

Furthermore, for signals not integer-positioned, the frequency content will be translated to an intermediate frequency f_{IF} according to,

$$\text{floor}\left(\frac{f_{RF}}{\frac{f_s}{2}}\right) = \begin{cases} \text{even} \implies f_{IF} = \text{rem}\left(\dfrac{f_{RF}}{f_s}\right) \\ \text{odd} \implies f_{IF} = f_s - \text{rem}\left(\dfrac{f_{RF}}{f_s}\right), \end{cases} \tag{2.2.4}$$

where $\text{floor}(a.bcd) = a$ and rem is the remainder after division. However, for the entire information band of the signal to be sampled, the constraints

$$\begin{aligned} 0 &\leq f_{IF} - \frac{BW}{2} \\ f_{IF} + \frac{BW}{2} &\leq \frac{f_s}{2}, \end{aligned} \tag{2.2.5}$$

must be met [22].

To employ bandpass sampling, the frequency content of the Radio Frequency (RF) signal must fall within the analog bandwidth of the ADC. Ad-

ditionally, the incoming signals must be filtered prior to sampling. This is required as all frequency content, including noise, within the analog bandwidth of the ADC are folded on top of the sampled spectra. Therefore a bandpass filter with a steep roll-off is required to prevent noise folding onto the information band and thereby degrading the Signal-to-Noise Ratio (SNR) [22].

2.2.2 Computing Platforms

In modern radio telescopes, the mechanical cost of constructing a large dish is traded for processing cost by using an array of antennas. The amount of data produced by a radio telescope increases linearly with the number of antennas in the array. This data rate further increases for dish antennas fitted with PAF technology. Furthermore, advances in microwave electronics have led to the production of wide-band receivers, even further increasing the amount of data to be processed [19].

Due to the large amounts of data produced the required Input-Output (IO) and computational rate increases. The amount of Complex Multiplications and Accumulations (CMAC) per second for a beamformer scale approximately as

$$\text{CMAC/s} \propto BW \times N \times N_b\,, \tag{2.2.6}$$

where BW is the bandwidth to be processed, N is the number of elements in the array and N_b is the number of beams to be produced [19].

The real-time signal processing algorithms for Radio Astronomy observations exhibit highly parallel characteristics. Therefore the hardware platforms used are primarily based around parallel processors such as FPGAs and GPUs.

GPUs have a parallel architecture and are good at floating point operations. Therefore GPUs are used for computationally expensive algorithms. However, as shown by [19], GPUs have low IO rates, causing data to bottleneck at the IO. FPGAs have greater bandwidth capability than GPUs and an IO rate of 250Gb/s vs 13Gb/s has been achieved by [23] for FPGAs and GPUs respectively. A GPU's capability, is not fully exploited if the processing time does not exceed the IO time. Another drawback of GPUs are the power consumption. It has been shown by [23] that for the same processing capability, GPUs may use between $3 - 20$ times more power than FPGAs.

The unit cost of a GPU is cheaper than the unit cost for an FPGA. However, a study on the processing needs for the MeerKAT's L-Band correlator, conducted by [24] shows a higher implementation cost for GPUs than for FPGAs. This is because more GPUs than FPGAs are needed to meet the same processing requirements. The study shows that as semi-conductor technology advances, less units have to be used, therefore decreasing the implementation cost. Furthermore, the study shows that when compared to GPUs, FPGAs have a longer operational life before it becomes more cost-effective to replace

the currently employed, but outdated technology, with more recent technology of the same architecture [24]. Note that this does not imply that GPU technology would have to be replaced more regularly.

Due to the advantages of FPGA technology, highlighted above, the scope of this thesis is limited to investigating beamformer implementations on FPGA based architectures.

2.2.3 Polyphase Filter Bank

The theory discussed within this Subsection, is based on [25]. The implementation of a Discrete Fourier Transform (DFT) for signal channelization causes leakage and scalloping loss.

The occurrence of leakage is seen from the definition of a DFT:

$$Q(f_b) = \sum_{t_d=0}^{N_S-1} q(t_d) e^{\frac{-j2\pi f_b t_d}{N_S}}, \tag{2.2.7}$$

where $Q(f_b)$ and $q(t_d)$ represents the discrete frequency and time series of the signal, respectively. It is seen that the time series is the multiplication of an infinite time series with an uniform window function, with a width equal to N_S. Therefore, the DFT of the finite time series, is the convolution of the Fourier transform of the infinite time series, with a sinc function. The sinc function transfers energy from the input frequency bin to other frequency bins. This energy transfer is referred to as leakage.

Additionally, because the sinc function is non-uniform across the frequency bin, energy is only preserved at the frequency bin center. This is known as scalloping loss.

To reduce leakage and scalloping loss, the Fourier transform of the infinite time series should rather be convolved with an uniform window instead of a sinc function. In the time domain this is equivalent to multiplication with a sinc function.

The concepts discussed above is the underlying principles of a PFB. A time series signal with a length $P \times M$, is multiplied by a windowing function and then split into P taps of length M each. Further, the P taps are added point by point to form a $1 \times M$ time series which may be Fourier transformed to complete the channelization procedure. For computational efficiency, the DFT is implemented with a FFT. Therefore, a PFB consists of a P tap Finite Impulse Response (FIR) filter along with a M-point FFT.

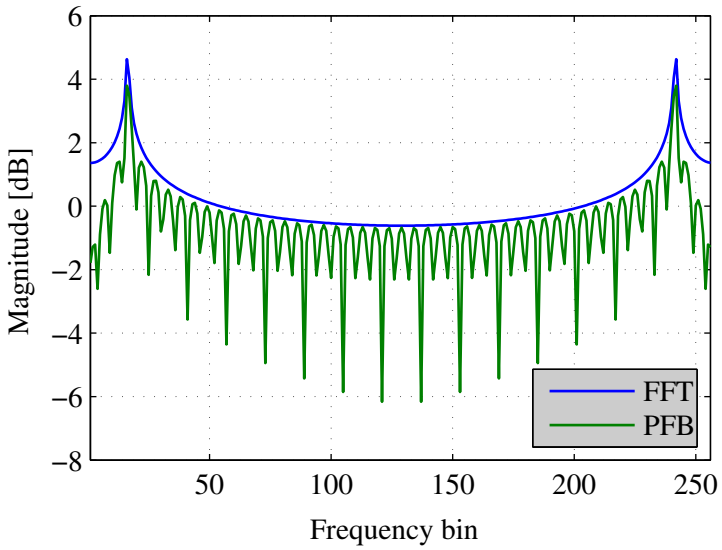

Figure 2.3: Comparison of FFT and PFB for channelization

Figure 2.3 depicts the MATLAB simulated, channelized response of a 50MHz signal sampled at 800MHz. A 256-point FFT, and a PFB consisting of a 4-tap sinc windowing function along with a 256-point FFT was used to channelize the sinusoid. From Figure 2.3 it is verified that the PFB implementation results in a more desirable way. Furthermore, due to symmetry in the output of the FFT and PFB only half of the channelized response requires further processing.

2.3 Classical Array Theory

An array is used to constructively add signals from directions of interest and destructively in other directions. Therefore an array is classified as a spatial filter because the array filters incoming signals based on their spatial relation to the array. The array effectively synthesizes an aperture and beam pattern which samples the incoming signals. The theory discussed in this Section is adapted from [26, Chapter 2].

The size and shape of the synthesized aperture and beam of an antenna array determines the spatial filtering characteristics of the array. A desired response may be obtained by correctly designing the array according to the following considerations:

- The number of antennas in the array, denoted by N
- The array configuration
- The beam pattern of individual elements
- Beamformer weights applied to the incoming signal

By appropriately setting the above parameters, a desirable beam may be synthesized [26].

Initially, the response of an arbitrary array of isotropic elements is determined in Subsection 2.3.1. The *pattern multiplication theorem* is also established in this Subsection. In Subsection 2.3.2 the isotropic array is constricted to a linear configuration. Thereafter, Subsection 2.3.3 defines certain performance metrics used throughout the thesis. Furthermore, the performance of an array is evaluated, with respect to the array parameters.

2.3.1 Array Response

Figure 2.4 depicts an arbitrary array configuration with N elements, where the elements are positioned at

$$\mathbf{a}_n = \begin{bmatrix} a_{xn} \\ a_{yn} \\ a_{zn} \end{bmatrix} . \tag{2.3.1}$$

Furthermore, a source signal $q(t)$ has an incoming direction $\mathbf{b}$, with respect to the origin as given by

$$\begin{aligned} \mathbf{b} &= \begin{bmatrix} b_x \\ b_y \\ b_z \end{bmatrix} \\ &= \begin{bmatrix} -\sin\theta\cos\phi \\ -\sin\theta\sin\phi \\ -\cos\theta \end{bmatrix} . \end{aligned} \tag{2.3.2}$$

For notational purposes, a directional cosine unit vector $\mathbf{u}$, is defined as

$$\begin{aligned} \mathbf{u} &= \begin{bmatrix} u_x \\ u_y \\ u_z \end{bmatrix} \\ &= \begin{bmatrix} \sin\theta\cos\phi \\ \sin\theta\sin\phi \\ \cos\theta \end{bmatrix} \\ &= -\mathbf{b} \end{aligned} \tag{2.3.3}$$

and will be used extensively in Chapter 3.

From Figure 2.4, it is evident that the source signal arrives at the elements at different times. A geometrical time delay τ_n is defined to account for this. The delay is determined with respect to the origin and for the n^{th} element in the array, τ_n is given by

$$\begin{aligned} \tau_n &= \frac{\mathbf{b}^T\mathbf{a}_n}{c} \\ &= -\frac{1}{c}\begin{bmatrix} a_{xn}\sin\theta\cos\phi & a_{yn}\sin\theta\sin\phi & a_{zn}\cos\theta \end{bmatrix} . \end{aligned} \tag{2.3.4}$$

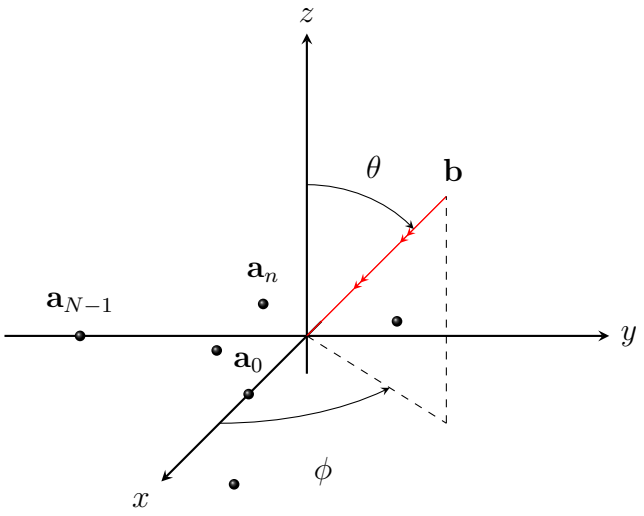

Figure 2.4: Arbitrary array in the conventional coordinate system

Therefore, the source signal arriving at the antenna elements can be described in terms of the delay as follows,

$$q_n(t) = q(t - \tau_n)\,. \tag{2.3.5}$$

From Fourier transform theory, a time delay corresponds to a phase shift in the frequency domain. Therefore, the frequency domain signal $Q_n(\omega)$, at the n^{th} element in the array is:

$$Q_n(\omega) = \int_{\infty}^{\infty} e^{-j\omega t} q(t - \tau_n)\, dt = e^{-j\omega\tau_n} Q(\omega)\,, \tag{2.3.6}$$

where $Q(\omega)$ is the Fourier transform of the source signal $q(t)$.

For a plane wave traveling in a homogeneous medium, the wavenumber $\mathbf{k}$ is defined by

$$\begin{aligned} \mathbf{k} &= -\frac{2\pi}{\lambda}\mathbf{u} \\ &= \frac{2\pi}{\lambda}\mathbf{b}\,. \end{aligned} \tag{2.3.7}$$

Given this definition of a wavenumber, the factor $\omega\tau_n$ in Equation 2.3.6 may also be expressed in terms of the element position and source wavenumber such as

$$\begin{aligned} \omega\tau_n &= \omega\frac{\mathbf{b}^T\mathbf{a}_n}{c} \\ &= 2\pi f\frac{\mathbf{b}^T\mathbf{a}_n}{f\lambda} \\ &= \mathbf{k}^T\mathbf{a}_n\,. \end{aligned} \tag{2.3.8}$$

The spatial characteristics of an array, with respect to a source with a specific wavenumber, can be described by the array manifold vector $\mathbf{v_k}(\mathbf{k})$,

$$\mathbf{v_k}(\mathbf{k}) = \begin{bmatrix} e^{-j\mathbf{k}^T\mathbf{a}_0} \\ e^{-j\mathbf{k}^T\mathbf{a}_1} \\ \vdots \\ e^{-j\mathbf{k}^T\mathbf{a}_{N-1}} \end{bmatrix} . \tag{2.3.9}$$

Therefore the signals at each element, in the frequency domain, can be written in vector form as follows,

$$\mathbf{Q}(\omega) = Q(\omega)\mathbf{v_k}(\mathbf{k}) . \tag{2.3.10}$$

Figure 2.5 depicts the beamformer process, given a unit incoming plane wave. The variable w_n^* represents the complex conjugate of the weight w_n. Depending on the application w_n can either be real or complex-valued. The output signal $Y(\omega, \mathbf{k})$, is the weighted sum of the incoming signals expressed as

$$Y(\omega, \mathbf{k}) = \sum_{n=0}^{N-1} w_n^* e^{-j\mathbf{k}^T\mathbf{a}_n} . \tag{2.3.11}$$

This is the response of the array to a unit plane wave incident along $\mathbf{k}$ and is referred to as the array factor AF, which may be written more compactly as

$$\begin{aligned} AF &= Y(\omega, \mathbf{k}) \\ &= \mathbf{w}^H\mathbf{v_k}(\mathbf{k}) . \end{aligned} \tag{2.3.12}$$

The above discussion assumed that the array consisted of isotropic elements. In order to determine the total array response $B(\theta, \phi)$, the beam patterns of individual antennas in the array must be accounted for. For an array with identical non-isotropic elements, the total array beam pattern is the multiplication of the array factor and the element beam pattern $B_e(\theta, \phi)$ as given by

$$B(\theta, \phi) = AF \times B_e(\theta, \phi) . \tag{2.3.13}$$

This principle is known as the *pattern multiplication theorem*.

2.3.2 Linear Array

For a linear array configuration, with the antennas placed along the y axis as depicted in Figure 2.6, the antenna positions simplify to,

$$\mathbf{a}_n = \begin{bmatrix} 0 \\ d\left(n - \frac{N-1}{2}\right) \\ 0 \end{bmatrix} , \quad n = 0, 1, ..., N-1 . \tag{2.3.14}$$

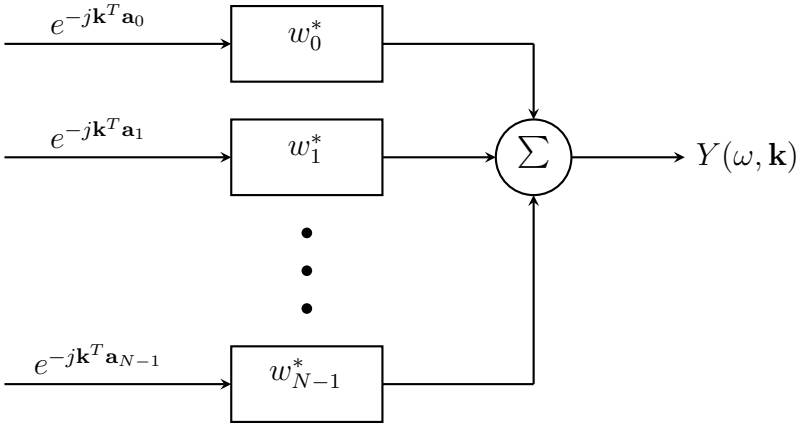

Figure 2.5: Beamformer topology

Additionally, for the remainder of this Section it is assumed, without any loss in generality, that the source has a $\phi = 90°$ component for which the wavenumber then reduces to

$$\mathbf{k} = -\frac{2\pi}{\lambda}\begin{bmatrix} 0 \\ \sin\theta \\ \cos\theta \end{bmatrix}. \tag{2.3.15}$$

For the antenna configuration and source direction depicted in Figure 2.6, the corresponding array manifold vector is given by

$$\mathbf{v}_\mathbf{k}(k_y) = \begin{bmatrix} e^{j(\frac{N-1}{2})k_y d} \\ e^{j(\frac{N-1}{2}-1)k_y d} \\ \vdots \\ e^{-j(\frac{N-1}{2})k_y d} \end{bmatrix}, \quad k_y = -\frac{2\pi}{\lambda}\sin\theta\,, \tag{2.3.16}$$

and is only dependent on the y component of the wavenumber.

The beam pattern is defined at physical angles, which corresponds to the visible region in space where signals can propagate. Signals outside the visible region decay at an exponential rate and are referred to as *evanescent signals*. For details on *evanescent signals* the reader is referred to [27]. The beam pattern, for an array of isotropic elements, in the k_y space is given by,

$$\begin{aligned} B(k_y) &= \mathbf{w}^H\mathbf{v}_\mathbf{k}(k_y) \\ &= \sum_{n=0}^{N-1} w_n^* e^{-j(n-\frac{N-1}{2})k_y d} \end{aligned} \tag{2.3.17}$$

and the corresponding visible region is defined across $-\frac{2\pi}{\lambda} \leq k_y \leq \frac{2\pi}{\lambda}$. In addition to the k_y space, the array manifold vector and beam pattern may be

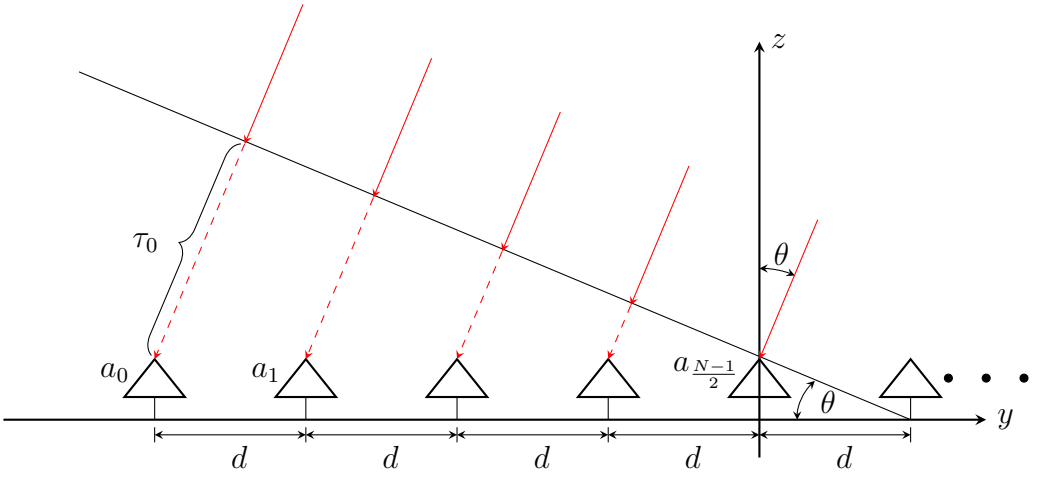

Figure 2.6: Linear array configuration convention

Table 2.1: Summary of domain definitions

Array Manifold Vector	Beam Pattern	Visible Region
$[\mathbf{v}_\theta(\theta)]_n = e^{j(n-\frac{N-1}{2})\frac{2\pi d}{\lambda}\sin\theta}$	$B_\theta(\theta) = \mathbf{w}^H\mathbf{v}_\theta(\theta)$	$-\frac{\pi}{2} \leq \theta \leq \frac{\pi}{2}$
$[\mathbf{v}_u(u)]_n = e^{j(n-\frac{N-1}{2})\frac{2\pi d}{\lambda}u}$	$B_u(u) = \mathbf{w}^H\mathbf{v}_u(u)$	$-1 \leq u \leq 1$

defined in the θ and u spaces as given in Table 2.1. Also listed in Table 2.1 are the visible regions, across which the beam patterns are defined.

From Equation 2.3.17, it can be seen that the beam pattern depends upon the complex weighting of the incoming signals. Additionally, it is evident that the synthesized beam pattern is dependent on the number of elements, as well as the configuration of the elements in the array. For a linear array configuration as depicted in Figure 2.6, the array can only steer the beam in the θ direction. The result is independent of ϕ, due to the symmetry of the array.

2.3.3 Performance Metrics

In this Subsection, performance metrics with respect to the beam pattern of a broadside array will be discussed. The array in consideration have equal spacings between elements which are uniformly weighted. Additionally, the functionality of an antenna array as a microwave network will be established and the appropriate network theory performance metrics will be defined. Furthermore, the array performance with respect to array and network theory, will be evaluated against the array parameters. The majority of the theory discussed in this Subsection has been adapted from [26, Chapter 2] and [28, Chapter 6].

The far-field radiation transmitted by an array is a function of angular direction. By reciprocity, this function is equivalent to the radiation received, when the array operates in receive mode. The function is defined as the radiation intensity $U(\theta, \phi)$ and is given by

$$U(\theta, \phi) \simeq \frac{1}{2\eta}[|E_\theta(\theta, \phi)|^2 + |E_\phi(\theta, \phi)|^2], \tag{2.3.18}$$

where η is the intrinsic impedance of the medium and E_θ, and E_ϕ are the far-field electric field components. By integrating the radiation intensity over a 4π solid angle, the radiated power P_{rad} is obtained and the result is as follows,

$$P_{rad} = \int_0^{2\pi} \int_0^{\pi} U(\theta, \phi) \sin\theta \, d\theta d\phi . \tag{2.3.19}$$

Furthermore, to measure the directive properties of an array the directivity $D(\theta, \phi)$ is defined,

$$D(\theta, \phi) = \frac{4\pi U(\theta, \phi)}{P_{rad}} . \tag{2.3.20}$$

As the array does not radiate all input power an efficiency factor e_a, given by

$$e_a = \frac{P_{rad}}{P_{in}} \tag{2.3.21}$$

is defined, to quantify the ratio of the radiated power to the input power. These terms are introduced to define the antenna array gain $G(\theta, \phi)$,

$$G(\theta, \phi) = e_a D(\theta, \phi) . \tag{2.3.22}$$

Array gain is an important performance metric because it accounts for both the efficiency and directive properties of the array.

Maximum radiation of an array is transmitted or received via the main lobe of the beam pattern. However, the main lobe decays as a function of angle. The angular extent across which radiation from the main lobe is above half of the maximum radiation, is defined as the Half-Power Beamwidth (HPBW). This is an important performance metric as it defines the minimum angular distance between two sources, such that they may be resolved by the array. The HPBW for a linear array is given by

$$\text{HPBW} = 2\sin^{-1}\left(0.446\frac{\lambda}{Nd}\right) . \tag{2.3.23}$$

Another measure of main lobe width is the angular extent between the first nulls in the beam pattern (BW_{NN}). The following equation,

$$\text{BW}_{NN} = 2\sin^{-1}\left(\frac{\lambda}{Nd}\right) \tag{2.3.24}$$

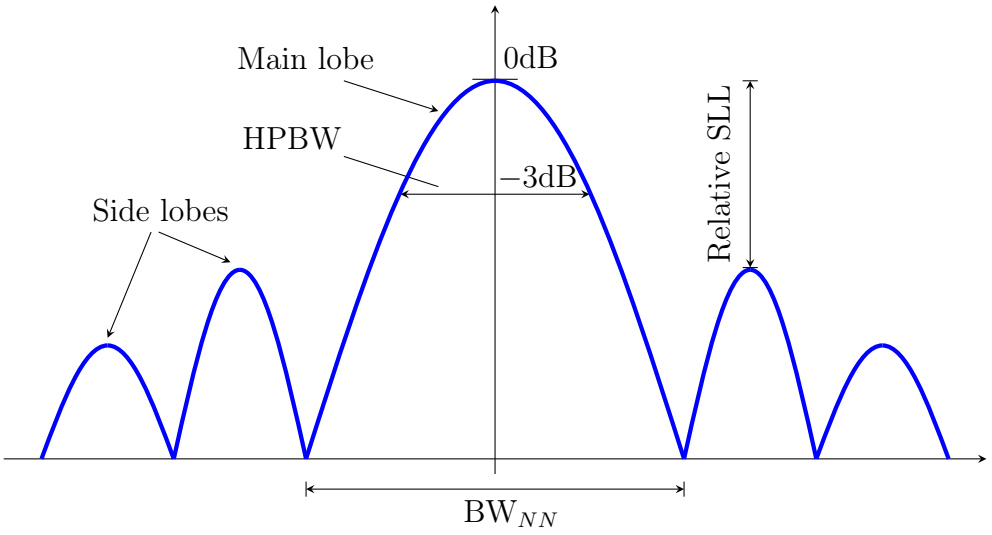

Figure 2.7: Beam pattern performance metrics

defines the BW$_{NN}$ for a linear array. Figure 2.7 provides a graphical definition of the HPBW and BW$_{NN}$ performance metrics.

For a $N \times M$ rectangular array steered to (θ_0, ϕ_0), the HPBW is given in terms of the beam solid angle Ω_A. The beam solid angle is the product of two HPBWs, defined in planes perpendicular to each other. One of the planes must contain the origin, broadside and the steering direction (θ_0, ϕ_0). The solid angle is given by

$$\Omega_A = \theta_H \Psi_H \tag{2.3.25}$$

where Ψ_H and θ_H are defined as

$$\Psi_H = \sqrt{\frac{1}{\theta_{x0}^{-2} \sin^2 \phi_0 + \theta_{y0}^{-2} \cos^2 \phi_0}} \tag{2.3.26}$$

$$\theta_H = \sqrt{\frac{1}{\cos^2 \theta_0 [\theta_{x0}^{-2} \cos^2 \phi_0 + \theta_{y0}^{-2} \sin^2 \phi_0]}}\,. \tag{2.3.27}$$

Furthermore the terms θ_{x0} and θ_{y0} are the HPBWs of a linear array with N and M elements respectively.

The rate at which the side lobes in the beam pattern degrades SL$_{degr}$ can be used to determine the height of the side lobes relative to the main lobe. It indicates the relative power level at which signals directed at the side lobes produce the same response as signals directed at the main lobe. For example, if the relative Side Lobe Level (SLL) is −13dB, the array will respond equivalently to a signal directed at the side lobes with a power level of 13dBm and a signal directed at the main lobe with a power level of 0dBm. The SL$_{degr}$ for

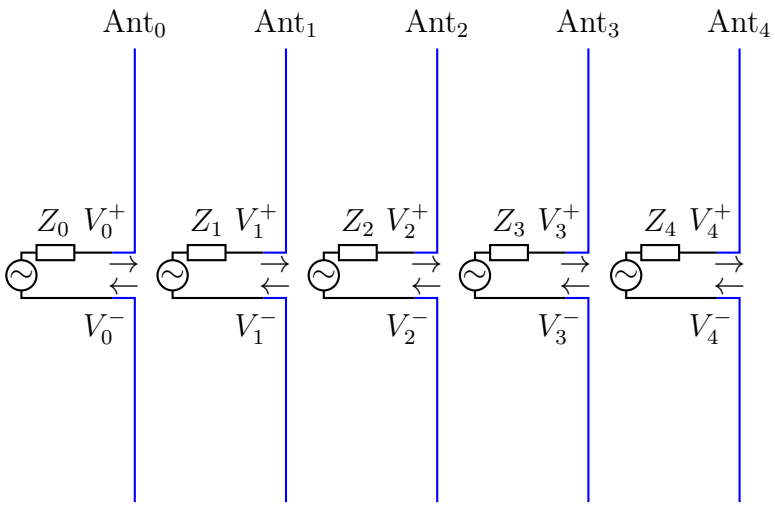

Figure 2.8: Antenna array network

a linear array is described by

$$\mathrm{SL}_{degr} = 20\log\left(\frac{1}{(N\sin(\frac{3\pi}{2N}))(2m+1)}\right), \quad m = 0, 1, 2, \ldots, \tag{2.3.28}$$

where m indicates the side lobe order. Refer to Figure 2.7 for a graphical depiction of the relative SLL.

An analysis of the array as a microwave network will now be considered. The relation between the incident and reflected waves, at antenna terminals, is described by the scattering matrix $\mathbf{S}$. Figure 2.8 depicts the incident V_n^+ and reflected voltage waves V_n^- at five antenna terminals. The $(ij)^{\text{th}}$ component of the scattering matrix is defined as

$$S_{ij} = \frac{V_i^-}{V_j^+}, \tag{2.3.29}$$

and relates the voltage wave at terminal i due to the voltage wave at terminal j [29].

The reflection coefficient Γ_i is given by,

$$\Gamma_i = S_{ii} \tag{2.3.30}$$

which is the reflected voltage wave at terminal i due to the incident voltage wave at terminal i. From the reflection coefficient, the Voltage Standing Wave Ratio (VSWR) can be determined,

$$\mathrm{VSWR} = \frac{1+|\Gamma|}{1-|\Gamma|}. \tag{2.3.31}$$

Furthermore, the scattering matrix provides the mutual coupling terms between the i^{th} and j^{th} antenna elements in an array. The mutual coupling terms increase as the inter-element spacing between the antennas decreases.

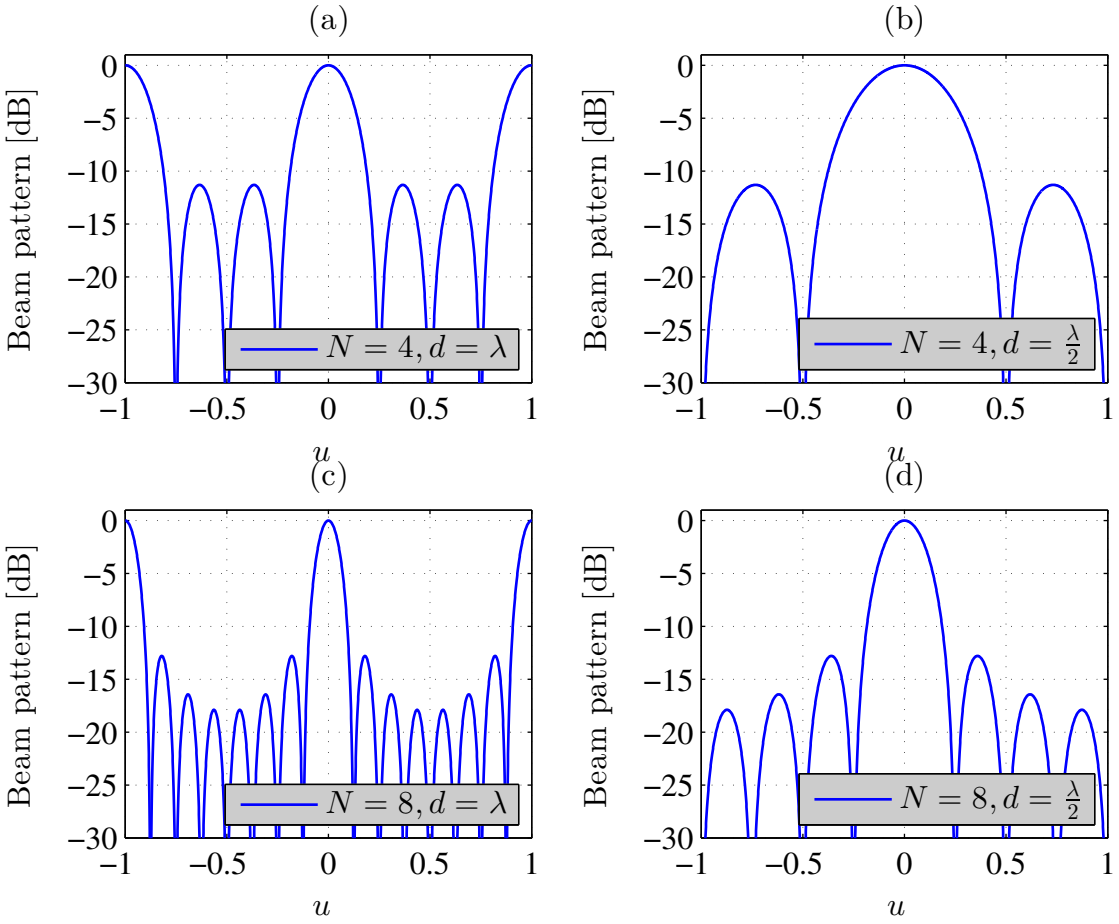

Figure 2.9: Effect of array parameters

Effect of Array Configuration on Beam Pattern

An array samples a source signal at the spatial rate set by the inter-element spacing. For an inter-element spacing $d \geq \lambda$, spatial aliasing occurs in the form of grating lobes. A grating lobe is a side lobe, within the visible region of the array factor, with the same height as the main lobe. Therefore, the response of the main lobe and grating lobes are equivalent. For a beam pattern containing grating lobes, the source direction must be known, in order to distinguish between desired and undesired signals.

Figure 2.9 depicts the resulting beam patterns for four different linear array configurations. A narrower HPBW increases the resolution of an array and can be obtained by increasing the electrical length. This is done by either increasing the element spacing or by using more elements in the array.

By increasing d from $\frac{\lambda}{2}$ to λ a narrower beam is synthesized, refer to Figures 2.9(a) and (b) as well as (c) and (d). However, grating lobes appear at $u = \pm 1$ when $d = \lambda$.

A resolution, equivalent to that in Figure 2.9(a), can be obtained by main-

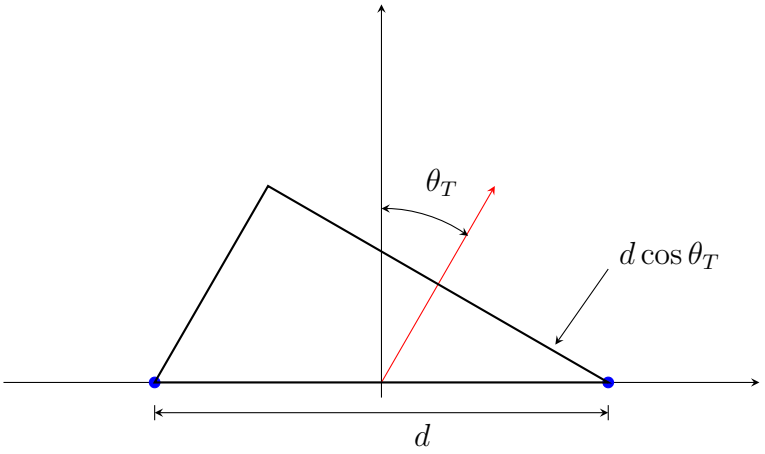

Figure 2.10: Effective inter-element spacing

taining $d = \frac{\lambda}{2}$ and increasing the number of elements from four to eight, as depicted in Figure 2.9(d). By comparison of Figures 2.9(a) and (d), it is verified that both cases yield the same resolution, however case (d) does not result in grating lobes as $d < \lambda$.

Effect of Steering an Array and Scan Limit

By choosing appropriate antenna weights, the beam of an array may be steered in different directions. The means by which these weighting functions are determined, in order to obtain a desirable beam pattern, are termed beamforming techniques and will be discussed in Chapter 3. In the following discussion the array is steered using weights which consist of a linear phase.

Assuming negligible mutual coupling terms, each element in the array radiates energy according to its beam pattern. However, by controlling the signal amplitude and phase at each element, the total array far-field radiation can add constructively and destructively in desired directions. The angular extent across which the array will be able to do this, is limited by the HPBW of a single element in the array. This is a direct result of the *pattern multiplication theorem*. Therefore an array cannot effectively steer the beam past half the HPBW of a single element in the array [30].

By steering the beam to θ_T, the effective inter-element spacing is reduced by a factor of $\cos\theta_T$, as indicated in Figure 2.10. The effective inter-element spacing is reduced more for larger scan angles. Mutual coupling terms between the elements also increase because the effective spacings are smaller.

Furthermore, as the inter-element spacing is smaller when the beam is steered, the main lobe broadens resulting in larger HPBWs. Figure 2.11 depicts the resulting beam patterns for an eight element linear array with the beam steered to $\theta_T = -45°$, $\theta_T = 0°$, and $\theta_T = 45°$. In the directional cosine

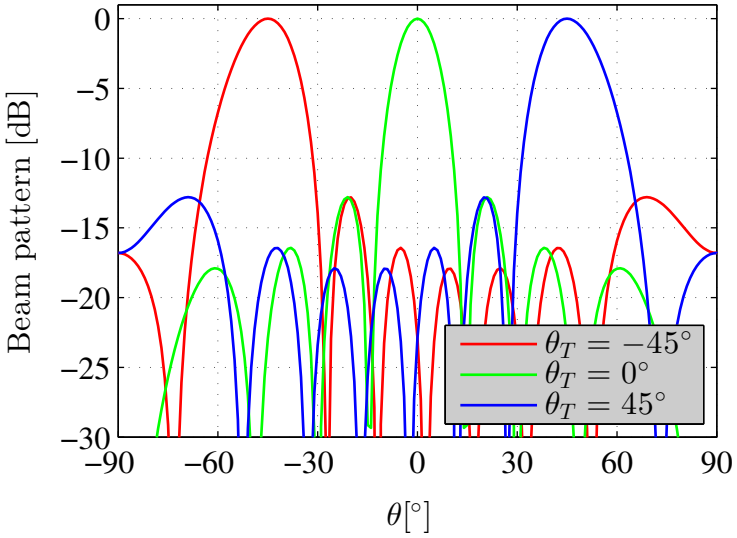

Figure 2.11: Array steering in θ domain

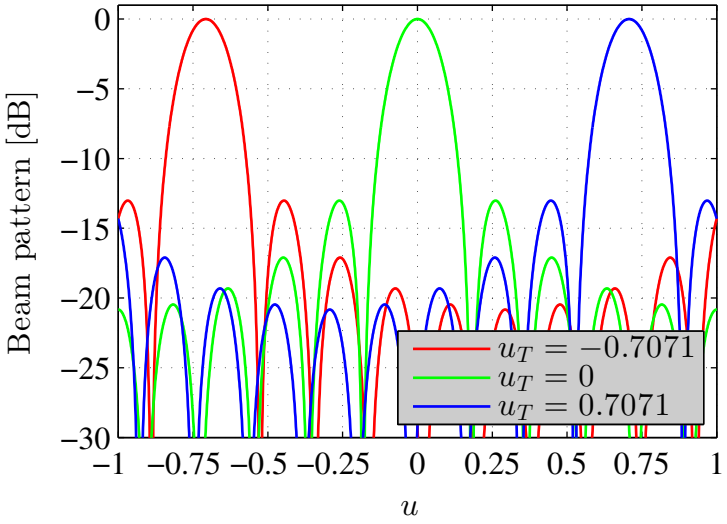

Figure 2.12: Array steering in u domain

coordinate system the beam pattern dependence on $\sin\theta$ is removed. This allows the beam pattern to retain its shape when the array is steered. This is useful in order to investigate the effect of a weighting function on the beam pattern, independent of the steering direction. By comparison of Figures 2.11 and 2.12 it is evident that the main lobe broadens for a larger scan angle in the θ space and that the beam pattern is not distorted in the u domain.

According to [26], an array reaches its scan limit when the left half-power point ceases to exist due to a significant increase in main lobe width. The left

half-power point θ_L can be obtained from,

$$\cos\theta_L = \cos\theta_T + 0.45\frac{\lambda}{Nd}\,, \tag{2.3.32}$$

and the scan limit occurs when $\theta_L = 0$.

Steering an array causes the grating lobes to shift, possibly to a position within the visible region of the beam pattern. Given a maximum scan angle θ_{max}, the condition

$$\frac{d}{\lambda} \leq \frac{1}{1 + |\sin\theta_{max}|} \tag{2.3.33}$$

must be satisfied, in order to ensure that grating lobes will not shift into the visible region once the array is steered. From Equation 2.3.33, it is clear that for a steering range $-\frac{\pi}{2} \leq \theta \leq \frac{\pi}{2}$, the inter-element spacing must be $d \leq \frac{\lambda}{2}$.

In the ideal case, one desires to synthesize a beam pattern which can scan in the range $-\frac{\pi}{2} \leq \theta \leq \frac{\pi}{2}$, with a high angular resolution and low side lobes. For such specifications it is necessary to have a large number of elements with omni-directional beam patterns, spaced $d = \frac{\lambda}{2}$ apart.

2.4 Beamformer Implementations

A beamformer may be implemented in either the time or frequency domain. The classification depends upon the domain in which summation occurs. The theory discussed in this Section is based on research conducted by [15].

2.4.1 Time Domain

As mentioned earlier, the source signal arrives at the antennas at different times. The geometric time delay can be compensated for by appropriately delaying the signals at the antennas. Time domain beamforming is inherently wide-band as the technique is based on compensating for the true time delay undergone by the signal.

Analog Implementation

In analog circuitry, the signals can be delayed using physical transmission lines. The signal undergoes a time delay, determined by the length and dielectric constant ϵ of the transmission line.

Each time delay therefore requires additional transmission lines for each antenna. The circuitry must be able to switch between the different transmission lines, in order to steer the beam and the number of transmission line combinations available, determines the resolution.

Furthermore, more hardware is needed if additional polarizations or multiple beams are desired. Therefore an analog time domain beamformer is expensive to implement.

Digital Implementation

Time domain beamforming in the digital domain may be accomplished by buffering the data from the signals which needs to be delayed. The data can only be delayed by an amount equal to a multiple of sample time.

To obtain higher resolutions the data needs to be interpolated. The effect of interpolating data points on the beamformer performance has not been thoroughly researched.

2.4.2 Frequency Domain

As mentioned earlier, a time delay corresponds to a phase shift in the frequency domain. A frequency domain beamformer is realized by applying appropriate phase shifts to the incoming signals.

By applying a phase shift to the incoming signals, the delay becomes dependent on frequency. This arises because a phase shift corresponds to a specific time delay for a specific frequency. Therefore, signals at the top of the band will be delayed less than the signals at the bottom of the band. Only a signal component at the center frequency will undergo the correct time delay.

Analog Implementation

Phase-shifters, based on vector modulators, are used to implement analog frequency domain beamformers. The vector modulator contains a set of linearly independent phases, which are weighted and combined to produce the phase corresponding to the time delay required. The number of polarizations processed and beams produced are limited and fixed by hardware.

Digital Implementation

To implement digital frequency domain beamforming, the incoming data must be channelized. After channelization, each sub-band is multiplied by a unique complex weight to account for the time delay. Errors occur because the phase shift only approximates the time delay over the sub-band. These errors become negligible for sufficiently narrow sub-bands.

Digital beamformers are flexible and can produce a reconfigurable number of beams. However, the maximum number of beams which can be synthesized is constrained by the output data rate and processing capability of the computing platform.

Due their flexibility and scalability, digital architectures are an attractive solution to beamforming. Digital beamforming is widely used throughout the Radio Astronomy community. The EMBRACE aperture array makes use of both analog and frequency domain beamformers. Two analog beams are produced at tile level and eight digital beams can be formed [12]. Furthermore,

the 2-Polarization All Digital (2-PAD) aperture array, is a demonstrator for the SKA, employing a digital frequency domain beamforming strategy [31].

For the reasons stated above, the scope of this thesis is limited to investigating digital frequency domain beamforming.

2.5 Conclusion

The basic components of a radio telescope were discussed in this Chapter. Specifically, the hardware platforms used within the Radio Astronomy community was considered. Further, the underlying theory of real-time processes such as bandpass sampling and channelization, used throughout the thesis, were developed.

Fundamental array theory and the conventions employed in the thesis, were also discussed in this Chapter. Both the response of an arbitrary and linear array were determined after which a number of performance metrics were defined. The effect of various array parameters on the performance of the array was established.

The Chapter concluded by discussing physical realizations of beamformers. Both time and frequency domain beamformers, implemented using either analog or digital techniques, were discussed.

Overall, the Chapter provided the necessary theory and motivation for the scope of this thesis. The importance of the complex weight multiplication was established and provides the motive for Chapter 3. Furthermore, reasons for limiting the scope of this thesis to investigating FPGA based frequency domain beamformers were highlighted throughout the Chapter.

Chapter 3

Beamforming Techniques

3.1 Introduction

As discussed in Chapter 2, an array filters incoming signals based on their spatial relations with the array. An array synthesizes a beam and the shape of the beam is dependent on the antennas in the array, the number of elements in the array and the array configuration. The effect of these parameters on the synthesized beam was discussed in Chapter 2. It was also mentioned that the synthesized beam may be modified, in a desirable manner, by beamforming techniques. Beamforming is the process of adding all incoming signals, weighted by appropriate values.

Depending on the mathematical and statistical models used, a beamformer may be classified as deterministic, optimum, or adaptive. Optimum beamformers assume certain statistical properties, such as the correlation coefficient matrix, of the incoming signal are known. The corresponding weight vector is determined from these assumed values. A beamformer is classified as adaptive if the statistical properties of the signal are measured from the incoming data, and the corresponding weight vector is adapted using the information obtained [26, Chapter 6]. This chapter is concerned with the effects of deterministic beamformers, as optimum and adaptive beamforming techniques are outside the scope of this thesis.

Deterministic techniques are used to optimize the beam pattern of an array. In addition to electronically pointing the beam of an array, which will be discussed in Section 3.2, the techniques may be used to maximize a certain array performance metric. The phase of the complex weights are used to steer the beam whereas the magnitude is used to control the relative SLL and beamwidth. Furthermore, null constraints may be imposed on the weight vector, to obtain a more favorable synthesized beam.

Figure 3.1 provides an overview of the beamforming algorithms which will be investigated. The spectral weighting, Dolph-Chebychev, and Least Square Error (LSE) algorithms will be discussed in Sections 3.3, 3.4, and 3.5 respec-

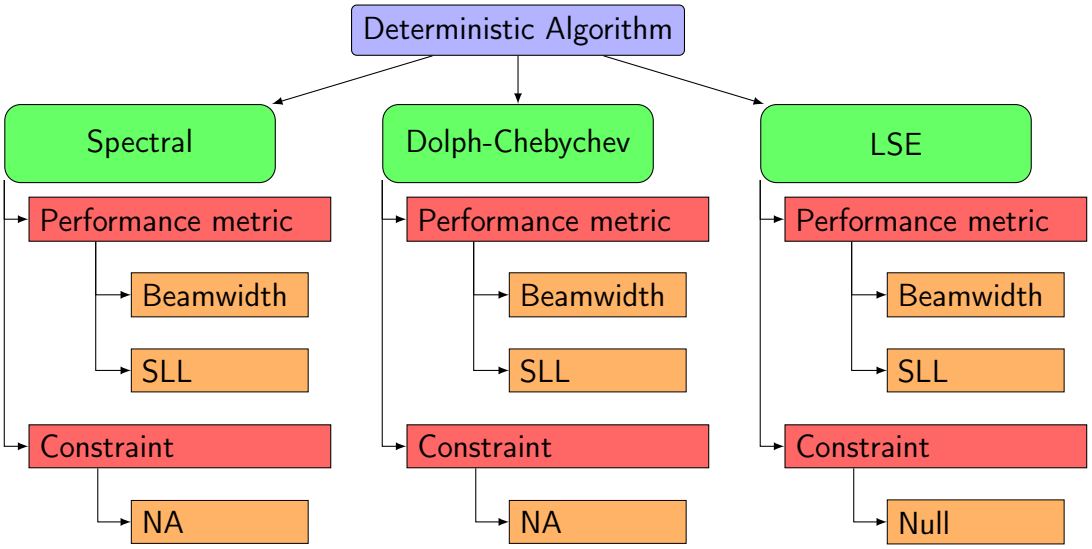

Figure 3.1: Overview of deterministic beamforming techniques

tively.

These algorithms were implemented in MATLAB for a linear array configuration with equal element spacing. Additionally, a subset of the program functionality was extended to account for rectangular planar array configurations. The theory discussed in this Chapter is adapted from [26, Chapters 3 and 4].

Furthermore, Section 3.6 discusses the Radio Astronomy applications of the implemented beamforming techniques.

3.2 Array Steering Weighting Functions

For an uniform linear array the output Y, of a beamformer is determined by,

$$Y = \mathbf{w}^H \mathbf{Q} \,. \tag{3.2.1}$$

In the θ domain the vector $\mathbf{Q}$ is defined as,

$$\mathbf{Q} = \mathbf{v}_\theta(\theta) Q \tag{3.2.2}$$

where the array manifold vector $\mathbf{v}_\theta(\theta)$ was defined in Chapter 2.

Steering is achieved by setting the $N \times 1$ weight vector $\mathbf{w}$, equal to an array

manifold vector with a target direction θ_T, therefore

$$\begin{aligned} \mathbf{w} &= \mathbf{v}_\theta(\theta_T) \\ &= \begin{bmatrix} e^{j(-\frac{N-1}{2})\frac{2\pi d}{\lambda}\sin\theta_T} \\ e^{j(1-\frac{N-1}{2})\frac{2\pi d}{\lambda}\sin\theta_T} \\ \vdots \\ e^{j(\frac{N-1}{2})\frac{2\pi d}{\lambda}\sin\theta_T} \end{bmatrix} . \end{aligned} \tag{3.2.3}$$

By substituting Equations 3.2.3 and 3.2.2 into Equation 3.2.1 the output Y is written as,

$$\begin{aligned} Y &= \mathbf{w}^H\mathbf{Q} \\ &= \mathbf{v}_\theta^H(\theta_T)\mathbf{v}_\theta(\theta)Q \\ &= \begin{bmatrix} (e^{j(-\frac{N-1}{2})\frac{2\pi d}{\lambda}\sin\theta_T})^* \\ (e^{j(1-\frac{N-1}{2})\frac{2\pi d}{\lambda}\sin\theta_T})^* \\ \vdots \\ (e^{j(\frac{N-1}{2})\frac{2\pi d}{\lambda}\sin\theta_T})^* \end{bmatrix}^T \begin{bmatrix} e^{j(-\frac{N-1}{2})\frac{2\pi d}{\lambda}\sin\theta} \\ e^{j(1-\frac{N-1}{2})\frac{2\pi d}{\lambda}\sin\theta} \\ \vdots \\ e^{j(\frac{N-1}{2})\frac{2\pi d}{\lambda}\sin\theta} \end{bmatrix} Q . \end{aligned} \tag{3.2.4}$$

From the substitution above, it can be seen that the output magnitude obtains a maximum when $\theta = \theta_T$.

For a $N \times M$ rectangular array with a target direction (θ_T, ϕ_T), an array manifold matrix is defined:

$$\begin{aligned} \mathbf{v}(\theta_T, \phi_T) &= \begin{bmatrix} \mathbf{v}_0 & \mathbf{v}_1 & \cdots & \mathbf{v}_{M-1} \end{bmatrix} \\ &= \begin{bmatrix} 1 & e^{j\psi_y} & \cdots & e^{j(M-1)\psi_y} \\ e^{j\psi_x} & e^{j(\psi_x+\psi_y)} & \cdots & e^{j(M-1)\psi_y} \\ \vdots & \vdots & \vdots & \vdots \\ e^{jn\psi_x} & e^{j(n\psi_x+\psi_y)} & \cdots & e^{j(n\psi_x+(M-1)\psi_y)} \\ \vdots & \vdots & \vdots & \vdots \\ e^{j(N-1)\psi_x} & e^{j((N-1)\psi_x+\psi_y)} & \cdots & e^{j((N-1)\psi_x+(M-1)\psi_y)} \end{bmatrix} , \end{aligned} \tag{3.2.5}$$

where ψ_x and ψ_y is given by,

$$\begin{aligned} \psi_x &= \frac{2\pi}{\lambda} d_x \sin\theta_T \cos\phi_T , \\ \psi_y &= \frac{2\pi}{\lambda} d_y \sin\theta_T \sin\phi_T . \end{aligned} \tag{3.2.6}$$

The rectangular array is steered to the target direction by setting the weight vector equal to an $NM \times 1$ array manifold vector which is obtained by stacking the columns of the manifold matrix as follows,

$$\text{vec}\left[\mathbf{v}(\theta_T, \phi_T)\right] = \begin{bmatrix} \mathbf{v}_0 \\ \mathbf{v}_1 \\ \vdots \\ \mathbf{v}_{M-1} \end{bmatrix} . \tag{3.2.7}$$

Subsequent Sections will investigate the effect of the weight vector magnitude, on the beam pattern. The beam pattern will therefore be plotted in the directional cosine coordinate system. Thereby by restricting the investigation, to the effect of the weight vector on the beam pattern.

3.3 Spectral Weighting

Spectral weightings exploit the Fourier transform relationship between the beam pattern, and the array weighting function. The Fourier relationship between the beam pattern and the weighting function will therefore be developed first.

For a continuous linear aperture of length l, situated on the y-axis, the far-field radiation is given by

$$B(k_y) = \int_{-\frac{l}{2}}^{\frac{l}{2}} w_a^*(y) e^{-jk_y y}\, dy\,, \tag{3.3.1}$$

where $w_a^*(y)$ is the current or voltage distribution across the aperture, referred to as the aperture weighting function. As $w_a^*(y) = 0$ for $|y| > \frac{l}{2}$ the integral in Equation 3.3.1 may be expressed from $-\infty$ to ∞. Therefore the far-field radiation pattern and aperture weighting function are Fourier duals,

$$B(k_y) \iff w_a^*(y)\,. \tag{3.3.2}$$

In order to replace the aperture with an equivalent array, the aperture weighting function is represented as samples of the array weighting function,

$$w_a^*(y) = \sum_{n=0}^{N-1} w_n^* \delta\left(y - d\left(n - \frac{N-1}{2}\right)\right)\,. \tag{3.3.3}$$

The far-field pattern $B(k_y)$ is then obtained by taking the inverse Fourier transform of the aperture weighting function, which simplifies as follows,

$$\begin{aligned} B(k_y) &= \int_{-\infty}^{\infty} w_a^*(y) e^{-jk_y y}\, dy \\ &= \int_{-\infty}^{\infty} \sum_{n=0}^{N-1} w_n^* \delta\left(y - d\left(n - \frac{N-1}{2}\right)\right) e^{-jk_y y}\, dy \\ &= \sum_{n=0}^{N-1} w_n^* e^{-j(n-\frac{N-1}{2})k_y d} \\ &= \mathbf{w}^H \mathbf{v_k}(k_y)\,. \end{aligned} \tag{3.3.4}$$

For an inter-element spacing kept at $d \leq \frac{\lambda}{2}$, grating lobes and spatial aliasing will not occur. Consequently, the Fourier transform properties may be applied to obtain a desirable beam pattern, hence the term spectral weighting.

An eleven element, broadside linear array with spacing $d = \frac{\lambda}{2}$ will be used here, to investigate uniform and sinusoidal weighting functions, followed by prolate spheroidal functions and Kaiser weightings. Additionally, the uniform and sinusoidal functions were extended for a rectangular planar array configuration. The weighting function will be denoted by w_n, where $n \in [0, 10]$ for the linear configuration and $|w_n|$ represents the magnitude of the weighting function.

3.3.1 Uniform and Sinusoidal Weighting Functions

An uniform weighting function applies identical weight magnitudes to all antennas in an array and is referred to as the conventional beamformer. It may be normalized with respect to the number of elements in the array as given by

$$w_n = \frac{1}{N}. \tag{3.3.5}$$

Uniform weighting results in large relative side lobes which may be decreased by using a cosine weighting function. For an odd number of elements in an array, the cosine weighting function may be calculated using

$$w_n = \sin\left(\frac{\pi}{2N}\right)\cos\left(\frac{\pi}{N}\left(n - \frac{N-1}{2}\right)\right). \tag{3.3.6}$$

Figure 3.2 and 3.3 respectively depicts the normalized beam pattern and weighting functions for both uniform and cosine weights. It can be seen that a cosine weighting function results in lower relative SLL but the width of the main lobe increases. In general it is desirable to obtain a weighting function which will decrease the relative SLL whilst minimizing the main lobe width increase.

Desired features from the uniform and cosine weighting functions may be combined to produce a raised cosine weighting function. The raised cosine weighting function is defined as

$$w_n = i(p)\left(p + (1-p)\cos\left(\frac{\pi}{N}\left(n - \frac{N-1}{2}\right)\right)\right), \tag{3.3.7}$$

where $i(p)$ is a constant given by

$$i(p) = \frac{p}{N} + \frac{1-p}{2}\sin\left(\frac{\pi}{2N}\right). \tag{3.3.8}$$

As variable p increases the relative SLL increases, however, the main lobe width becomes narrower. For $p = 0$, the resulting beam pattern is equivalent

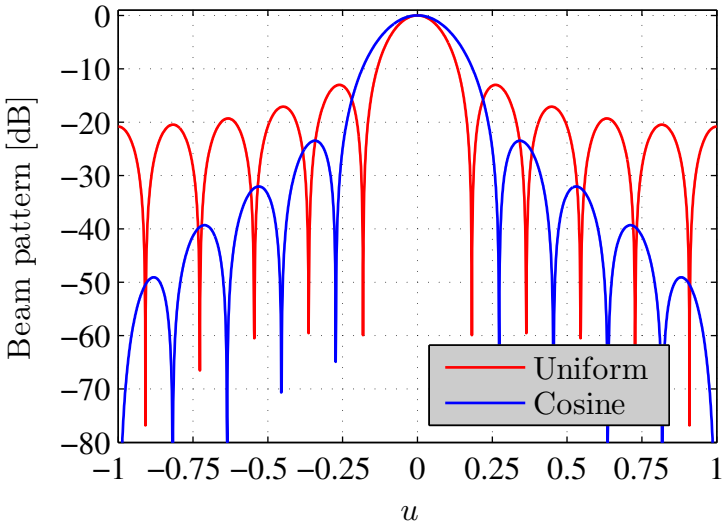

Figure 3.2: Normalized beam pattern for uniform and cosine weighting function

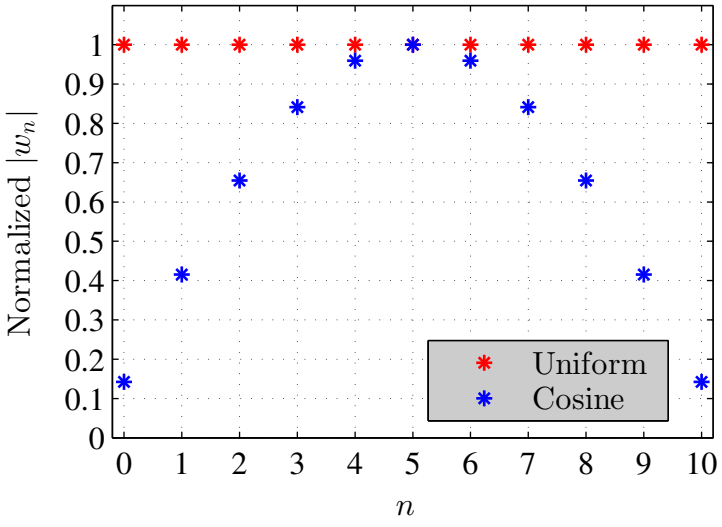

Figure 3.3: Uniform and cosine weighting functions

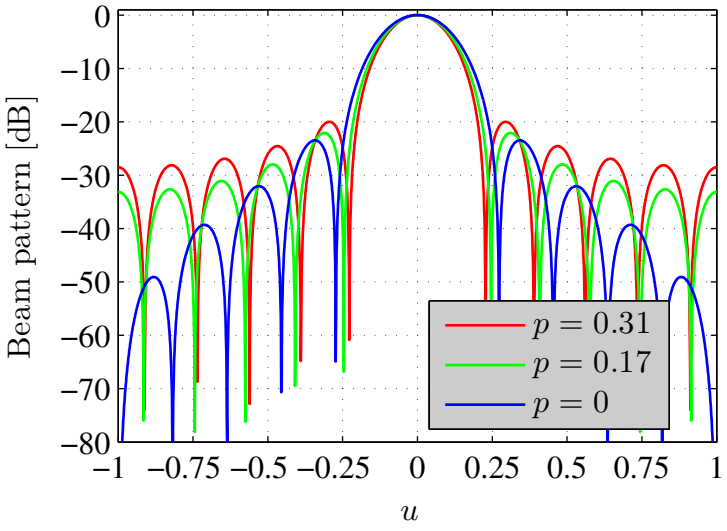

Figure 3.4: Normalized beam pattern for raised cosine weighting functions

to that produced by a cosine weighting function. Conversely, for $p = 1$ the beam pattern is equivalent to that produced by a uniformly weighted array.

Figure 3.4 shows the normalized beam pattern for three different values of p. From Figure 3.4 it is confirmed that larger and smaller value of p results in a narrower main lobe and lower side lobes respectively.

The corresponding weighting functions are depicted in Figure 3.5. From this Figure it can be seen that as p increases the weighting function starts to approximate a uniform weighting function. Additionally, it can be seen that for smaller values of p the weighting function tends toward a cosine weighting function.

Another weighting function used to reduce the SLL is the cosine^m weighting function, given by

$$w_n = i_m \cos^m\left(\frac{\pi}{N}\left(n - \frac{N-1}{2}\right)\right), \tag{3.3.9}$$

where the constant i_m is a normalization factor. A higher order m, results in a lower SLL but wider main lobe. A second order, $m = 2$, weighting function is referred to as the Hann weighting function.

The beam patterns for a second, third and fourth order cosine^m weighting function, are illustrated in Figure 3.6. Furthermore, the weights applied are depicted in Figure 3.7. From Figure 3.6 it is verified that higher orders result in lower relative SLL but increases the main lobe width.

A raised cosine-squared weighting function is described by

$$w_n = i_2(p)\left[p + (1-p)\cos^2\left(\frac{\pi}{N}\left(n - \frac{N-1}{2}\right)\right)\right], \tag{3.3.10}$$

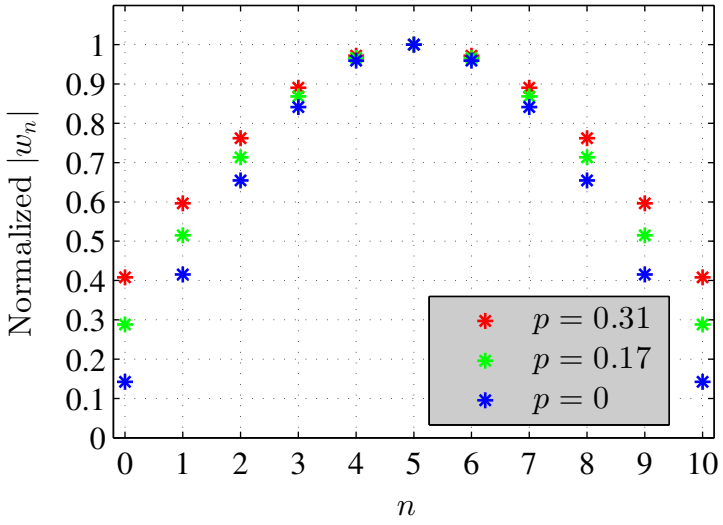

Figure 3.5: Raised cosine weighting functions

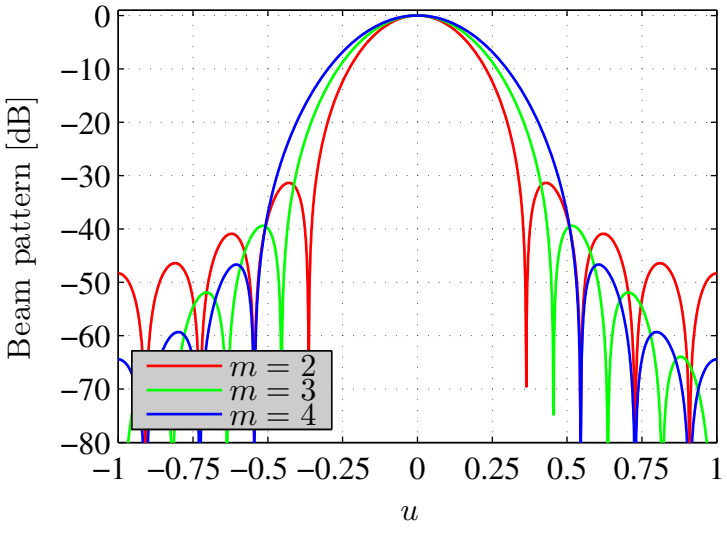

Figure 3.6: Normalized output for cosine^m weighting functions

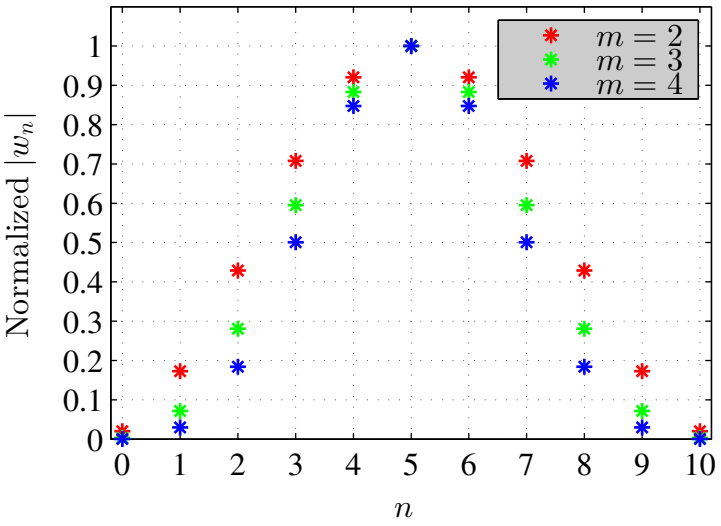

Figure 3.7: Cosine^m weighting functions

where the constant $i_2(p)$ is a normalization factor. For the specific case where $p = 0.08$, a Hamming weighting function is obtained. The Hamming function provides a null in the beam pattern at the position where a Hann function would have obtained its first side lobe peak. This concept may be extended to place nulls at higher order side lobes, by using the Blackman-Harris weighting function given by,

$$w_n = 0.42 + 0.5\cos\left(\frac{2\pi}{N}\left(n - \frac{N-1}{2}\right)\right) + 0.08\cos\left(\frac{4\pi}{N}\left(n - \frac{N-1}{2}\right)\right). \tag{3.3.11}$$

Figure 3.8 provides a comparison between the resulting beam patterns due to a Hann, Hamming, and Blackman-Harris weighting function, with the weighting functions plotted in Figure 3.9. It is observed that Hamming weights result in the narrowest main lobe output but larger higher order side lobes, while Blackman-Harris weightings results in very small relative SLL but a broad main lobe.

The above weighting functions have been extended for rectangular arrays. Figure 3.10 depicts the normalized output for a 10×10 rectangular planar array, with half wavelength spacing and a target direction at broadside.

From the discussions above it is clear there exists a definite trade-off between the relative SLL and main lobe width. Therefore, the following Subsection will discuss weighting functions to optimize this trade-off.

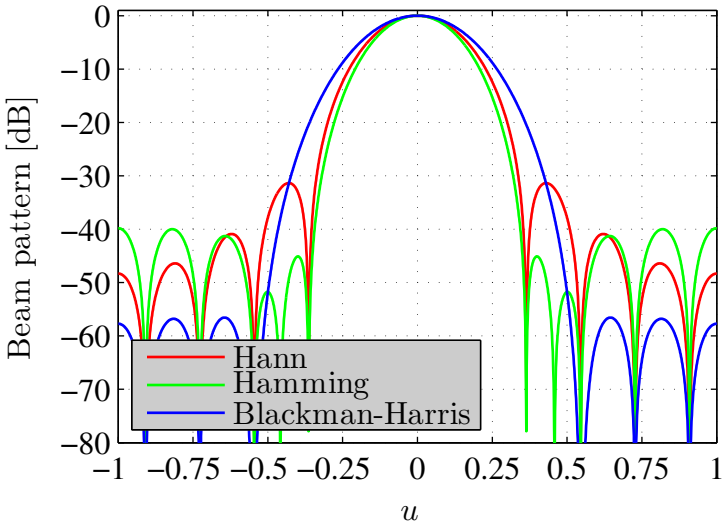

Figure 3.8: Normalized beam pattern for Hann, Hamming, and Blackman-Harris weighting functions

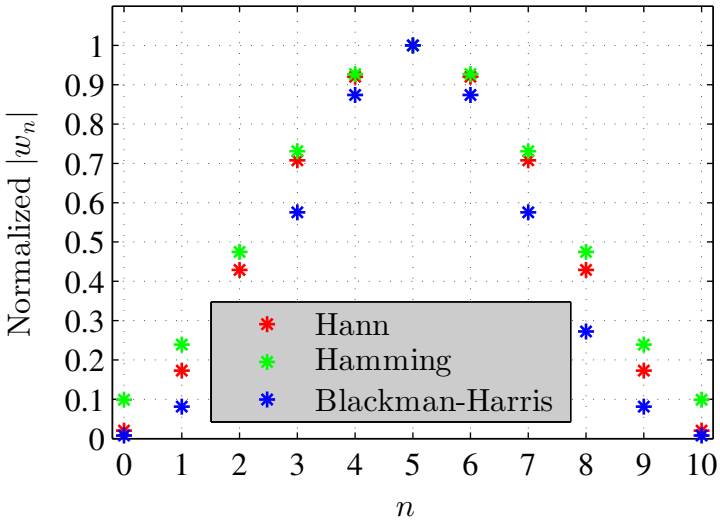

Figure 3.9: Hann, Hamming, and Blackman-Harris weighting functions

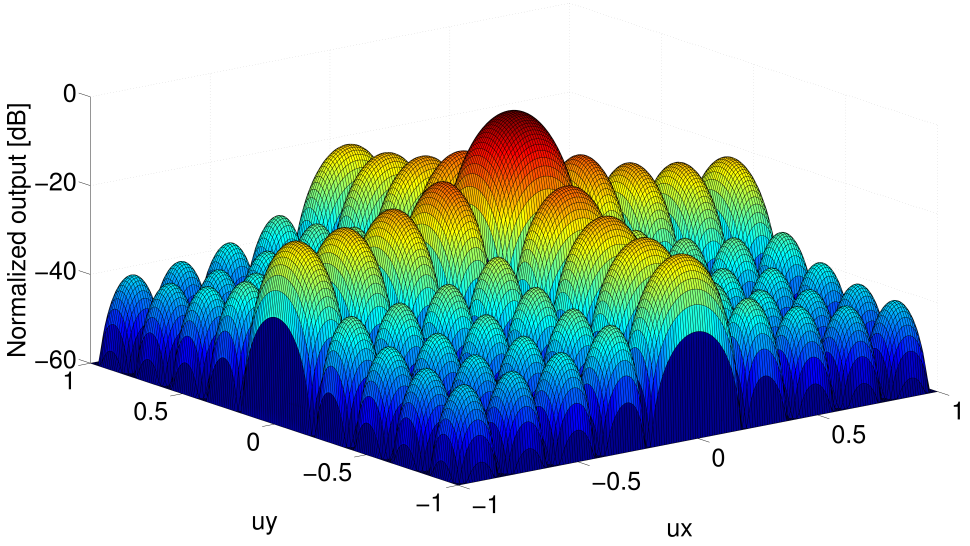

Figure 3.10: Normalized beam pattern for a rectangular array with uniform weights

3.3.2 Prolate Spheroidal Functions and Kaiser Weightings

The trade-off between SLL and main lobe width may be optimized by using prolate spheroidal functions. The functions are derived by maximizing the ratio of power in a given angular extent u_0, over the total power. The ratio will be developed in terms of the weight vector, such that the weights can be determined from the maximized ratio.

The following Equation,

$$\rho = \frac{\int_{-u_0}^{u_0} |B_u(u)|^2 \, du}{\int_{-1}^{1} |B_u(u)|^2 \, du} , \tag{3.3.12}$$

describes the function to be maximized for a linear array. By making the substitution $B_u(u) = \mathbf{w}^H \mathbf{v}_u(u)$, the numerator in Equation 3.3.12 may be expressed as,

$$\begin{aligned} \rho_N &= \int_{-u_0}^{u_0} \mathbf{w}^H \mathbf{v}_u(u) \mathbf{v}_u^H(u) \mathbf{w} \, du \\ &= \mathbf{w}^H \int_{-u_0}^{u_0} \mathbf{v}_u(u) \mathbf{v}_u^H(u) \, du \, \mathbf{w} \\ &= \mathbf{w}^H \mathbf{A} \mathbf{w} , \end{aligned} \tag{3.3.13}$$

given that the matrix $\mathbf{A}$ is,

$$\mathbf{A} = \int_{-u_0}^{u_0} \mathbf{v}_u(u) \mathbf{v}_u^H(u) \, du . \tag{3.3.14}$$

Furthermore, the denominator in Equation 3.3.12 can be written as

$$\begin{aligned}\rho_D &= \int_{-1}^{1} \mathbf{w}^H \mathbf{v}_u(u)\mathbf{v}_u^H(u)\mathbf{w}\, du \\ &= \mathbf{w}^H \int_{-1}^{1} \mathbf{v}_u(u)\mathbf{v}_u^H(u)\, du\, \mathbf{w} \\ &= 2\mathbf{w}^H \mathbf{I}\mathbf{w} \\ &= 2\mathbf{w}^H \mathbf{w}\,,\end{aligned} \tag{3.3.15}$$

by making the same substitution as for the numerator. By using the simplifications the ratio is written as,

$$\rho = \frac{\mathbf{w}^H \mathbf{A}\mathbf{w}}{2\mathbf{w}^H \mathbf{w}}\,. \tag{3.3.16}$$

The ratio is maximized by setting the weight vector $\mathbf{w}$, equal to the eigenvector, which corresponds to the largest eigenvalue λ_e in

$$2\lambda_e \mathbf{w} = \mathbf{A}\mathbf{w}\,. \tag{3.3.17}$$

The resulting weight vector is referred as a Discrete Prolate Spheroidal Sequence (DPSS).

Figure 3.11 illustrates the beam patterns obtained by maximizing the power over an angular extent of $u_0 = 0.1$, $u_0 = 0.2$, and, $u_0 = 0.4$. The corresponding weighting functions are depicted in Figure 3.12. From Figure 3.11 it is verified that a narrower beam is obtained for smaller angular extents, however the relative SLL is increased. As the angular extent increases, the relative SLL decreases but the main lobe width broadens thereby reducing the angular resolution of the array.

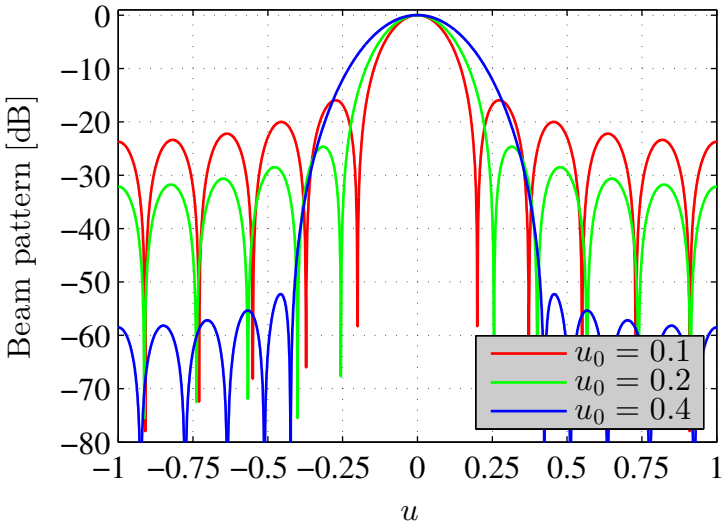

Figure 3.11: Normalized output for DPSS weighting functions

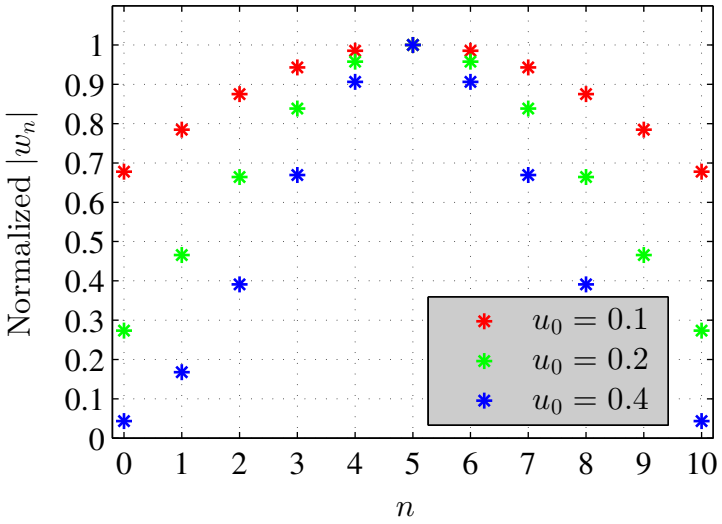

Figure 3.12: DPSS weighting functions

The DPSS weighting function may become computationally expensive for large N, relative to the other spectral weightings, as it requires the calculation of eigenvalues and eigenvectors. Therefore, Kaiser weighting functions approximate the DPSS functions by making use of the zero-order modified Bessel function of the first kind [1]. The weighting function,

$$w_n = I_0\left(\alpha\sqrt{1-\left(\frac{2}{N}\left(n-\frac{N-1}{2}\right)\right)^2}\right) \tag{3.3.18}$$

describes the Kaiser weights, where $I_0(x)$ is the zero-order modified Bessel function of the first kind and α determines the trade-off between the main lobe width and relative SLL.

The exact relationship between the Kaiser and DPSS weighting function has not been established. However, by comparing the beam patterns depicted in Figure 3.13 it is verified that the Kaiser weighting function does indeed approximate the DPSS weighting function.

[1] Refer to Appendix A.1, for the definition of a modified Bessel function of the first kind

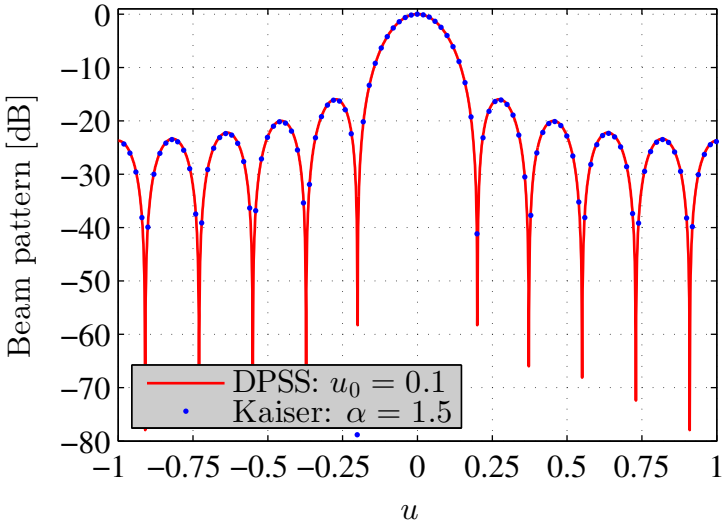

Figure 3.13: Normalized beam pattern for DPSS and Kaiser weighting functions

Additional beam patterns for Kaiser weights, corresponding to $\alpha = 3$ and $\alpha = 6$, are illustrated in Figure 3.14. From this Figure it is observed that larger α factors provide lower relative SLL and broader beams, whilst smaller α factors provide larger relative SLL with a narrower main lobe. Refer to Figure 3.15 for the corresponding weighting function.

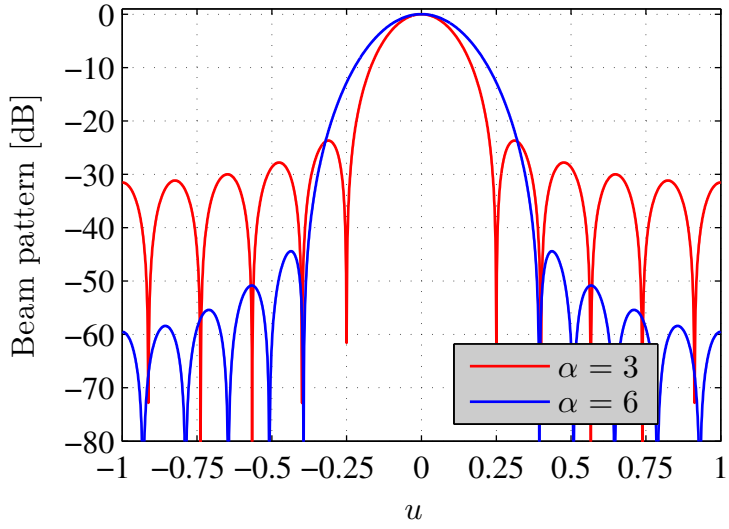

Figure 3.14: Normalized beam pattern for Kaiser weighting functions

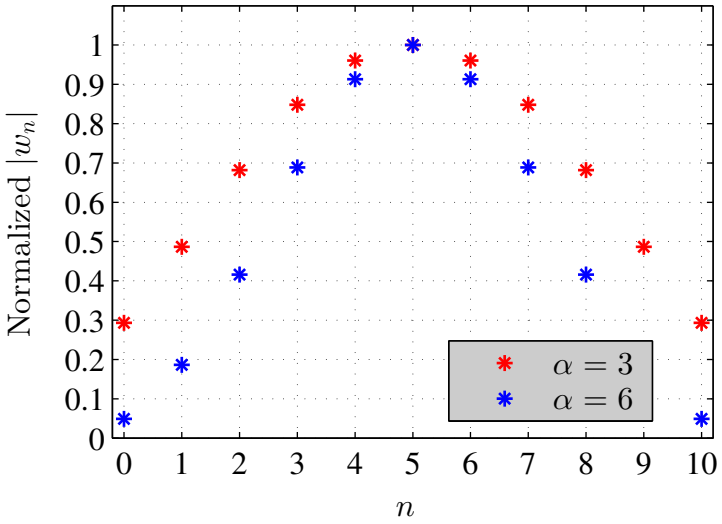

Figure 3.15: Kaiser weighting functions

3.4 Dolph-Chebychev Weighting

Another classical beamforming algorithm is the Dolph-Chebyshev weighting function. The Dolph-Chebyshev weighting function results in a constant side lobe level whilst minimizing the main lobe beamwidth. Weights are designed to explicitly control the beamwidth and SLL of a beam pattern. This section includes the derivation of the Dolph-Chebyshev weights adapted from [26, Chapter 3] and [28, Chapter 6]. This is followed by a simulation, using the MATLAB program which was written during the execution of the project.

The procedure to synthesize a Dolph-Chebyshev weighting function includes, decomposing the beam pattern into a polynomial function, followed by equating the result with a Dolph-Chebyshev polynomial, of the same order, to determine the weighting function. The Chebychev polynomial function is given by the following Equation,

$$T_m(x) = \begin{cases} \cos\left(m\cos^{-1}x\right), & |x| \leq 1, \\ \cosh\left(m\cosh^{-1}x\right), & x > 1, \\ (-1)^m\cosh\left(m\cosh^{-1}|x|\right), & x < -1, \end{cases} \tag{3.4.1}$$

where m describes the order of the polynomial and x defines the regions of the variable.

Consider the linear array configurations depicted in Figure 3.16. The antennas a_n, are placed symmetrically about the origin and are weighted symmetrically, using a real function w_n. Therefore the corresponding beam pattern will also be real and symmetric and can be written in terms of a trigonometric

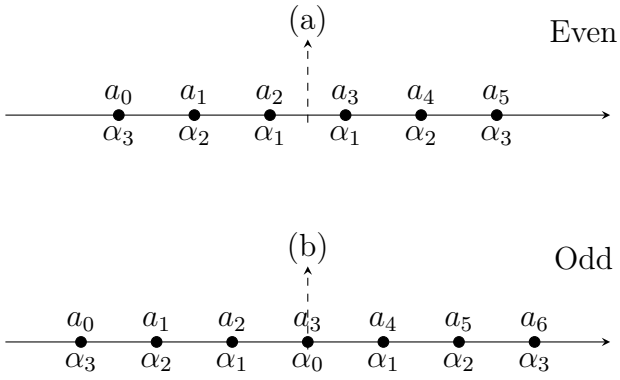

Figure 3.16: Broadside linear array with (a) even number of elements $N = 6$, and (b) odd number of elements $N = 7$

function as such,

$$B(u) = \begin{cases} \sum_{i=1}^{\frac{N}{2}} \alpha_i \cos\left[\left(\frac{\pi(2i-1)d}{\lambda}\right)u\right], & N \text{ even} \\ \sum_{i=0}^{\frac{N-1}{2}} \alpha_i \cos\left(\frac{2i\pi d}{\lambda}u\right), & N \text{ odd} \end{cases} \tag{3.4.2}$$

where α_i relates to the weights according to

$$\alpha_i = \begin{cases} 2w_n|_{n=i-1+\frac{N}{2}}, \quad i \in [1, \frac{N}{2}], & N \text{ even} \\ 2w_n|_{n=i+\frac{N-1}{2}}, \quad i \in [1, \frac{N-1}{2}], & N \text{ odd} . \end{cases} \tag{3.4.3}$$

Additionally, for an odd N, $\alpha_0 = w_{\frac{N-1}{2}}$.

Furthermore, by taking the real part of the binomial series expansion[2] of Equation 3.4.2, the result can be expressed as an m^{th} order Chebychev polynomial function. From Equation 3.4.1 and by making the substitution $x = \cos(\frac{\pi d}{\lambda}u)$, the Chebychev polynomial function is given by,

$$\begin{aligned} T_m(x)|_{x=\cos(\frac{\pi d}{\lambda}u)} &= \cos\left[m\cos^{-1}\left(\cos\left(\frac{\pi d}{\lambda}u\right)\right)\right] \\ &= \cos\left(m\frac{\pi d}{\lambda}u\right), \end{aligned} \tag{3.4.4}$$

because $|\cos(\frac{\pi d}{\lambda}u)| < 1$.

[2]Refer to Appendix A.2, for details of the binomial series expansion

However, the purpose of using Chebychev polynomials is to obtain a constant SLL, whilst minimizing the main lobe width. The procedure consists of selecting a Chebychev polynomial with order $m = N - 1$ and choosing a ratio R,

$$R = \frac{\text{main lobe maximum}}{\text{SLL}} \tag{3.4.5}$$

greater than unity. This is followed by selecting a unity SLL, such that the ratio R simplifies to the main lobe maximum. The main lobe maximum corresponds to the following Chebychev polynomial,

$$\begin{aligned} R &= T_{N-1}(x_0), \\ &= \cosh\left((N-1)\cosh^{-1} x_0\right) , \end{aligned} \tag{3.4.6}$$

where $x_0 > 1$ because $R > 1$, which follows from the properties of Chebychev polynomials that if $x > 1$ then $|T_m(x)| > 1$. Following from Equation 3.4.6, the location of the main lobe maximum x_0 can be calculated as

$$x_0 = \cosh\left(\frac{1}{N-1}\cosh^{-1} R\right) . \tag{3.4.7}$$

The normalized beam pattern, with constant SLL is then given by,

$$B(u) = \frac{1}{R} T_{N-1}\left(x_0 \cos\left(\frac{\pi d}{\lambda} u\right)\right) . \tag{3.4.8}$$

For an array steered to broadside, the corresponding weight vector is obtained by sampling the beam pattern at N intervals. The first sample is taken at the maximum, $u_0 = 0$, and the remaining $N - 1$ intervals correspond to nulls in the beam pattern. The following Equation represents the sampled beam pattern, $\mathbf{B}$

$$\begin{aligned} \mathbf{B} &= \begin{bmatrix} B(u_0) & B(u_1) & \cdots & B(u_p) & \cdots & B(u_{N-1}) \end{bmatrix} \\ &= \mathbf{w}^H \mathbf{V}(\boldsymbol{u}) \\ &= \begin{bmatrix} 1 & 0 & \cdots & 0 & \cdots & 0 \end{bmatrix} , \end{aligned} \tag{3.4.9}$$

where the $N \times N$ array manifold matrix is given by,

$$\mathbf{V}(\boldsymbol{u}) = \begin{bmatrix} \mathbf{v}(u_0) & \mathbf{v}(u_1) & \cdots & \mathbf{v}(u_p) & \cdots & \mathbf{v}(u_{N-1}) \end{bmatrix} . \tag{3.4.10}$$

Therefore the weight vector can be solved by using,

$$\mathbf{w} = [\mathbf{V}^H(\boldsymbol{u})]^{-1}\mathbf{B} , \tag{3.4.11}$$

where the nulls are located at

$$u_p = \frac{\lambda}{\pi d}\cos^{-1}\left[\frac{1}{x_0}\cos\left(\frac{(2p-1)\pi}{(N-1)2}\right)\right] , \quad p = 1, \cdots, N-1 . \tag{3.4.12}$$

Figure 3.17 depicts the beam patterns obtained for a specified SLL of −20dB, −30dB and, −40dB. The simulation uses eleven elements and implements the algorithm discussed above. Additionally, the corresponding weighting functions obtained are plotted in Figure 3.18.

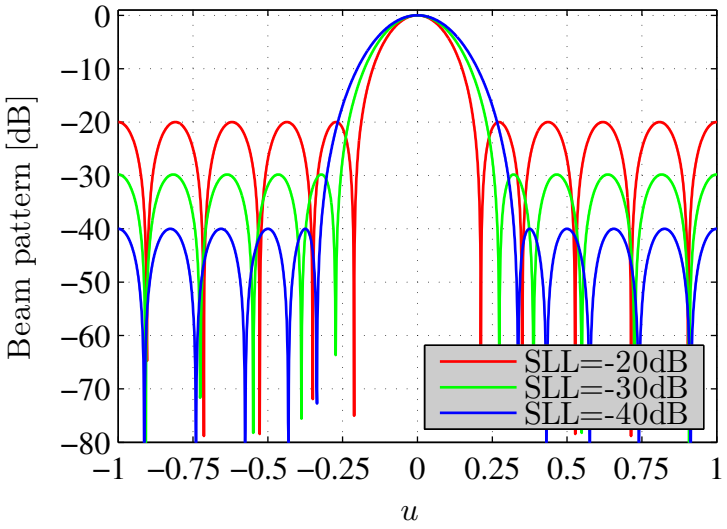

Figure 3.17: Normalized beam patterns for Dolph-Chebychev weighting functions

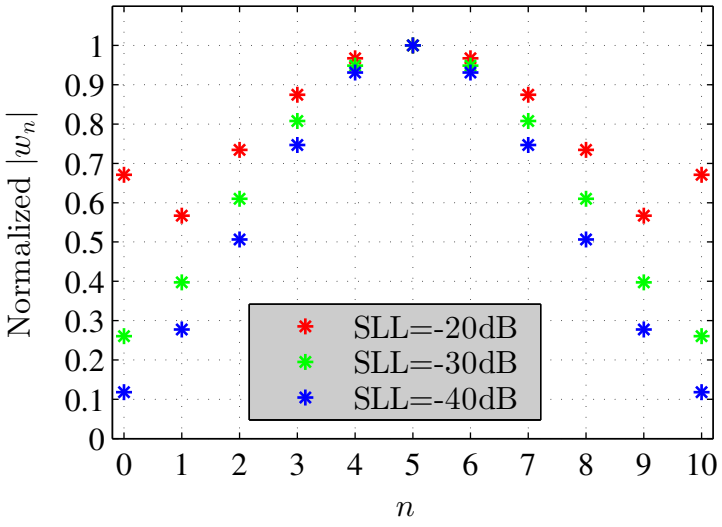

Figure 3.18: Dolph-Chebychev weighting functions

3.5 Least Square Error

The LSE algorithm depends upon the squared difference between a desired $B_d(u)$ and achieved beam pattern $\mathbf{w}^H\mathbf{v}(u)$, where $\mathbf{v}(u)$ is the $N \times 1$ array manifold vector and $\mathbf{w}$ is the $N \times 1$ weight vector. The theory discussed in this Section, is based on [26, Chapter 3].

The following error function ε_{LSE}

$$\varepsilon_{LSE} = \int_{-1}^{1} |B_d(u) - \mathbf{w}^H\mathbf{v}(u)|^2 \, du \,, \tag{3.5.1}$$

is minimized, in order to obtain the minimal error between the desired and achieved beam patterns.

In order to minimize the error function, the complex gradient[3] of Equation 3.5.1 is taken with respect to $\mathbf{w}^H$ and set to $\mathbf{0}$ as follows,

$$\begin{aligned} \mathbf{0} &= -\int_{-1}^{1} \mathbf{v}(u)B_d^*(u) \, du + \left[\int_{-1}^{1} \mathbf{v}(u)\mathbf{v}^H(u) \, du\right] \mathbf{w_o} \\ &= -\int_{-1}^{1} \mathbf{v}(u)B_d^*(u) \, du + \mathbf{A}\mathbf{w_o} \,. \end{aligned} \tag{3.5.2}$$

where the $N \times N$ matrix $\mathbf{A}$ is defined as,

$$\mathbf{A} = \int_{-1}^{1} \mathbf{v}(u)\mathbf{v}^H(u) \, du \,. \tag{3.5.3}$$

The optimized $N \times 1$ weight vector $\mathbf{w_o}$ can then be obtained,

$$\mathbf{w_o} = \mathbf{A}^{-1} \int_{-1}^{1} \mathbf{v}(u)B_d^*(u) \, du \,. \tag{3.5.4}$$

The LSE algorithm may be used in conjunction with a set of constraints, to synthesize a desirable pattern. In the following Subsection, the procedure to synthesize a desired beam pattern, subject to null constraints will be discussed.

3.5.1 Null Steering

The error function, discussed above, can also be written as

$$\varepsilon_{LSE} = |\mathbf{w}_d - \mathbf{w}|^2 \,, \tag{3.5.5}$$

[3]Refer to Appendix A.3, for the definition of a complex gradient

where $\mathbf{w}_d$ and $\mathbf{w}$ corresponds to the weighting vectors of the desired and constrained beam patterns respectively.

A zero-order constraint $\mathbf{C}_0$ matrix, is used to impose nulls in desired directions by ensuring,

$$\mathbf{w}^H \mathbf{v}(u_i) = 0, \quad i = 1, 2, \cdots, M_0\,, \tag{3.5.6}$$

where u_i is the locations for M_0 different nulls. Therefore $\mathbf{C}_0$ is defined as,

$$\mathbf{C_0} = \left[\mathbf{v_u}(u_0) \quad \mathbf{v_u}(u_1) \quad \cdots \quad \mathbf{v_u}(u_{M_0})\right]\,. \tag{3.5.7}$$

Additional constraint matrices may be imposed on the derivatives of the beam pattern. A first-order constraint $\mathbf{C}_1$ is defined,

$$\mathbf{C_1} = \left[\frac{d\mathbf{v_u}(u_0)}{du_0} \quad \frac{d\mathbf{v_u}(u_1)}{du_1} \quad \cdots \quad \frac{d\mathbf{v_u}(u_{M_1})}{du_{M_1}}\right], \quad M_1 \subseteq M_0\,, \tag{3.5.8}$$

as well as a second order constraint $\mathbf{C}_2$,

$$\mathbf{C_2} = \left[\frac{d^2\mathbf{v_u}(u_0)}{du_0^2} \quad \frac{d^2\mathbf{v_u}(u_1)}{du_1^2} \quad \cdots \quad \frac{d^2\mathbf{v_u}(u_{M_1})}{du_{M_1}^2}\right], \quad M_2 \subseteq M_1\,. \tag{3.5.9}$$

The result is a total set of constraint matrices $\mathbf{C}$,

$$\mathbf{C} = \left[\mathbf{C_0} \quad \mathbf{C_1} \quad \mathbf{C_2}\right]\,. \tag{3.5.10}$$

In order to obtain the optimized weight vector, it is required to minimize Equation 3.5.5 subject to,

$$\mathbf{w}^H \mathbf{C} = \mathbf{0}\,. \tag{3.5.11}$$

To this end Lagrange multipliers may be used, which results to

$$\Lambda = \left[\mathbf{w}_d^H - \mathbf{w}^H\right]\left[\mathbf{w}_d - \mathbf{w}\right] + \mathbf{w}^H\mathbf{C}\boldsymbol{\lambda} + \boldsymbol{\lambda}^H\mathbf{C}^H\mathbf{w}\,. \tag{3.5.12}$$

The vector $\boldsymbol{\lambda}$ is the Lagrange multiplier. Furthermore, the function Λ can be minimized by setting the complex gradient of Equation 3.5.12, to zero, where the gradient is taken with respect to $\mathbf{w}$. The result is given by,

$$\mathbf{0} = -\mathbf{w}_d^H + \mathbf{w}_o^H + \boldsymbol{\lambda}^H\mathbf{C}^H\,, \tag{3.5.13}$$

where the constrained weighting vector $\mathbf{w}$ is replaced by the optimized weighting vector $\mathbf{w}_o$. Equation 3.5.13 can be written as,

$$\mathbf{w}_o^H = \mathbf{w}_d^H - \boldsymbol{\lambda}^H\mathbf{C}^H\,, \tag{3.5.14}$$

and the constraint in Equation 3.5.11 is used to solve for $\boldsymbol{\lambda}$. It follows that,

$$\mathbf{0} = \mathbf{w}_d^H\mathbf{C} - \boldsymbol{\lambda}^H\mathbf{C}^H\mathbf{C} \tag{3.5.15}$$

and therefore,

$$\boldsymbol{\lambda}^H = \mathbf{w}_d^H\mathbf{C}\left[\mathbf{C}^H\mathbf{C}\right]^{-1}\,. \tag{3.5.16}$$

Equation 3.5.16 is substituted into Equation 3.5.14, to yield the optimized weight vector,

$$\mathbf{w}_o^H = \mathbf{w}_d^H - \left(\mathbf{w}_d^H \mathbf{C}[\mathbf{C}^H\mathbf{C}]^{-1}\right)\mathbf{C}^H . \tag{3.5.17}$$

The beam patterns for a zero, first and second order null constraint imposed on the weight vector is shown in Figure 3.19. A desired uniform weight vector, with 21 elements and a null constraint at $u_0 = 0.22$ was used to synthesize the beam patterns, using the above algorithm. From Figure 3.19 it is observed that higher order constraints reduces the beam pattern gain in the null direction. Furthermore, the corresponding weight vectors are plotted in Figure 3.20.

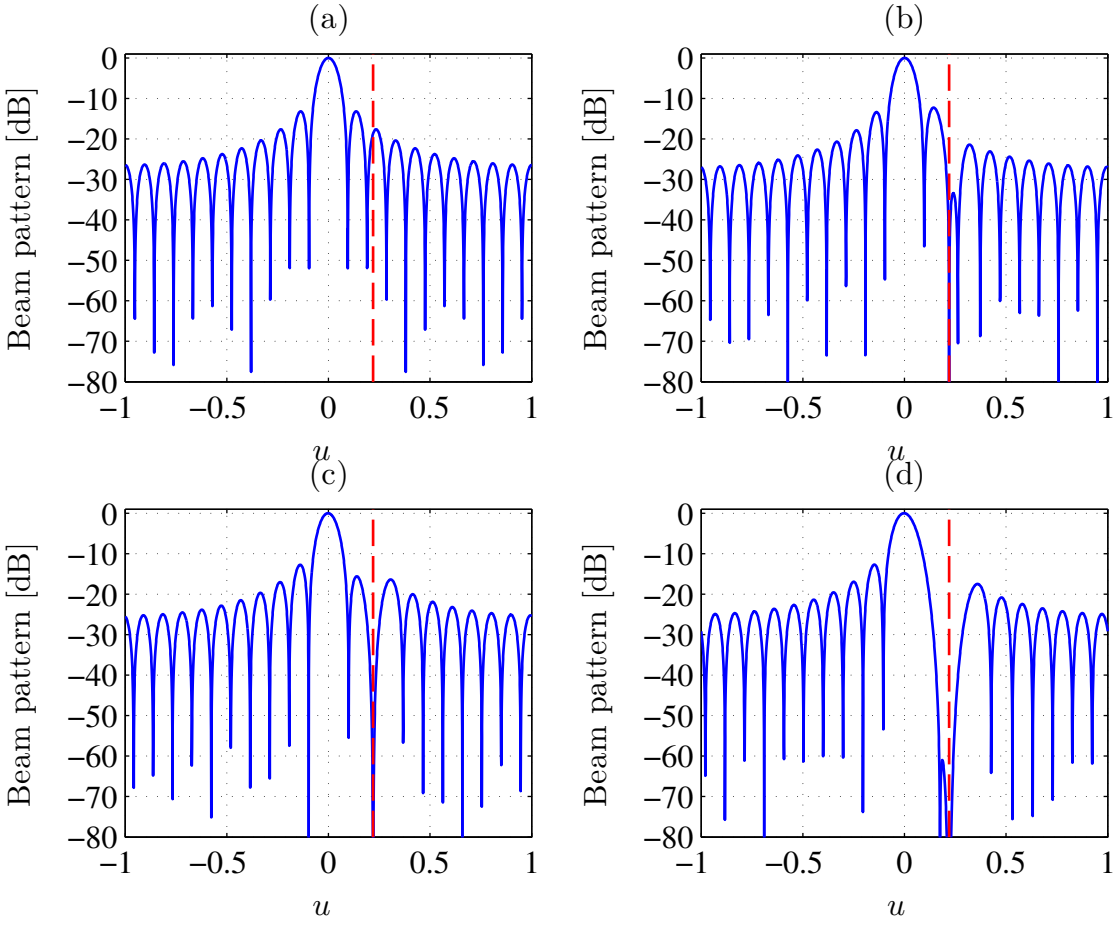

Figure 3.19: Normalized beam pattern for uniform weights with: (a) No null constraint (b) Zero-order null constraint (c) First-order null constraint (d) Second-order null constraint

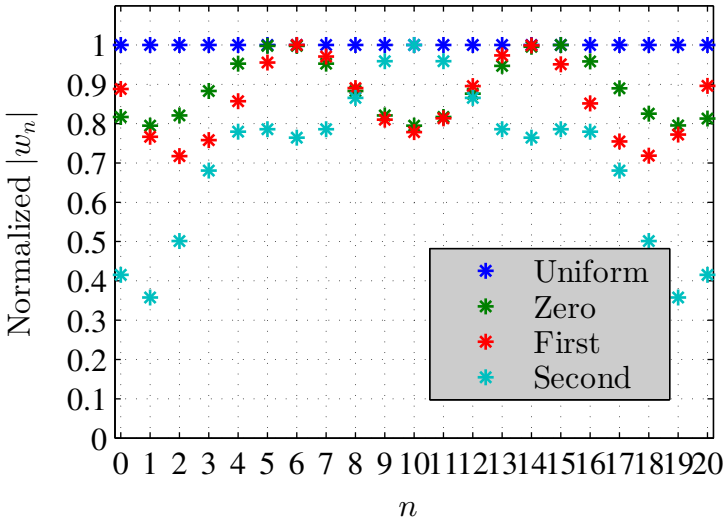

Figure 3.20: Null-steering weighting functions

3.6 Applications in Radio Astronomy

This Section provides an overview of the Radio Astronomy applications, of the beamforming techniques discussed in the previous Sections.

The steering algorithm, discussed in Section 3.2, is used to electronically steer the beam of an array, thereby creating a software radio telescope, capable of tracking Radio Astronomy sources, within scanning limit of the array. Tracking can be achieved by updating the target direction, according to the movement of the source across the sky. The spatial samples provided by an interferometric array is increased by tracking a source, which also results to an increase in integration time and is used to reduce noise [32].

At low frequencies mechanical limitations prohibit the construction of large steerable arrays. Therefore fixed aperture arrays are used at low frequencies and the beam of the aperture array is pointed electronically by using a steering algorithm.

The steering algorithm may be implemented multiple times with different target directions, thereby synthesizing multiple beams in desired directions. For a single beam, the field of view FoV_b is defined as,

$$FoV_b = \frac{\pi}{4}(\text{HPBW})^2 \,. \tag{3.6.1}$$

The total FoV is then given by

$$FoV = N_b \, FoV_b \,, \tag{3.6.2}$$

where N_b is the number of beams. Therefore, the FoV is increased by creating multiple beams. The number of beams may vary, as a function of frequency, to ensure a constant FoV across the operating band of the radio telescope [33].

Additionally, the FoV of a radio telescope is directly proportional to the survey speed SS as given by,

$$SS = \left(\frac{A_{eff}}{T_{sys}}\right)^2 \times FoV\,, \tag{3.6.3}$$

where A_{eff} is the effective area and T_{sys} is the system temperature. Therefore, given a constant system temperature a larger FoV increases the survey speed of a radio telescope [33].

Furthermore, by creating multiple beams, the instrument is capable of conducting more than one scientific experiment simultaneously. The EMBRACE aperture array has successfully demonstrated this concept. Two analog beams are produced, capable of conducting two different radio observations simultaneously [12]. During 2011, EMBRACE observed a neutral hydrogen spectral line at a frequency of 1420.406MHz whilst simultaneously observing a pulsar in another direction, at a frequency of 1200MHz [34].

The spectral and Dolph-Chebychev beamforming algorithms are used to reduce the relative SLL, whilst limiting the main lobe width increase. These techniques were discussed in Sections 3.3 and 3.4 respectively. Both algorithms are used to reduce the array temperature. During a Radio Astronomy observation, the array temperature is increased by sky noise located within the vicinity of the side lobes. By producing smaller side lobes, using these algorithms, the sky noise contribution to the array temperature is reduced [35].

However, by decreasing the SLL the main lobe width increases, which is undesirable as it decreases the resolution capabilities of the radio telescope. It has been shown by [28], that a Dolph-Chebychev results in the narrowest possible main lobe for a given SLL. A Dolph-Chebychev weighting function is therefore more frequently used within the Radio Astronomy community to produce lower SLL.

Despite the drawback, spectral weightings are used within the Radio Astronomy community for other purposes. For example, a known desired beam pattern may easily be obtained, by exploiting the Fourier relation between the beam pattern and the weighting function. The resulting beam pattern is an analytic function which can be used to simplify calibration techniques [36].

Radio Frequency Interference (RFI) poses many challenges for the Radio Astronomy community. Radio sources are very faint and terrestrial interference drown out sources of interest. The null steering algorithm, discussed in Section 3.5.1, is used to place a null in the direction of an RFI source. Thereby rejecting interference and serving as technique, to ensure observational data is not contaminated by RFI.

3.7 Conclusion

In this chapter a theoretical framework of beamforming techniques and their uses within the Radio Astronomy community were established. A MATLAB program was written to investigate the effect of various weighting functions on the beam pattern of an array.

In this Chapter, the weight vector to steer the beam of an array to a target direction was established. The technique has wide spread applications within the Radio Astronomy community and an overview of these were given.

Uniform, sinusoidal, DPSS, and Kaiser weightings are a subset of spectral weights. The spectral weighting technique exploits the Fourier relationship between the beam pattern and the weighting function. There is a trade-off between the relative SLL and width of the main lobe in the output of the beam pattern. Therefore the choice of weighting function, will depend on the specifications of the radio telescope.

Another method to explicitly control the trade-off between relative SLL and main lobe width is the Dolph-Chebychev weighting function. As the weighting function results in the narrowest beamwidth for a given SLL, it serves as the preferable method to reduce the array temperature.

Furthermore, the LSE algorithm minimizes the error between a desired and achieved beam pattern. Null constraints may be imposed on the resulting weight vector, to place a null in a specific direction in the beam pattern. Null steering serves as an RFI mitigation technique, within the Radio Astronomy community.

From this Chapter, the flexibility of a radio telescope employing beamforming techniques is evident. Therefore, subsequent Chapters will investigate frequency domain beamformer implementations.

Chapter 4

Uniform Linear Array Emulation

4.1 Introduction

In this chapter, the emulation of a uniform linear array using the UniBoard will be presented. The UniBoard is a high performance computing platform with scalable hardware developed by ASTRON, under the RadioNet-FP7 project which is led by the Joint Institute for VLBI in Europe (JIVE) [37].

A generic design strategy has been employed such that the UniBoard may be used for several Radio Astronomy signal processing applications. Correlation, digital filtering and pulsar processing are among these applications currently being developed [38].

For the purposes of this work the beamformer firmware, developed by ASTRON for the Aperture Tile In Focus (APERTIF) project, is of most interest. A UniBoard configured with the beamformer firmware will be used for the emulation of an uniform linear array.

An overview of the APERTIF project, as well as the beamformer firmware for UniBoard is given in Section 4.2. This is followed by the implementation of the emulated linear array in Section 4.3. Additionally, the verification, results, and analysis are discussed in Section 4.4.

4.2 APERTIF Project and UniBoard

4.2.1 APERTIF Project

The APERTIF project is an upgrade of the feed systems of the Westerbork Synthesis Radio Telescope (WSRT), see Figure 4.1. Twelve of the fourteen 25m dish radio telescopes will be fitted with PAF technology. The operating frequency is set to range between $1 - 1.75$GHz, with an instantaneous band width of 300MHz [39].

Figure 4.1: The WSRT in the Netherlands

The multi-beam capability of PAF technology increases the FoV of a radio telescope. For a constant T_{sys}, the FoV is directly proportional to the survey speed, as discussed in Chapter 3.6. The goal is to increase the WSRT survey speed by a factor of 20, achieved by having a FoV of $8(^{\circ})^2$. A large FoV will be obtained by producing 37 beams for each dish. Vivaldi antennas, each with their own LNA, are arranged in both horizontal and vertical polarizations. For APERTIF the computing units are able to process 64 signals per polarization which are digitized at 800MHz in the second Nyquist zone. For each polarization, four UniBoards are used to perform the beamforming operation [37] [39].

4.2.2 UniBoard Hardware and Beamformer Firmware

Figure 4.2 depicts the hardware layout for the UniBoard. The UniBoard is fitted with eight Altera StratixIV FPGAs, producing a total processing capacity of 2 Tera Multiplications and Accumulations (TMAC) per second. Furthermore, the FPGAs are arranged into two columns forming four Back Node (BN) FPGAs and four Front Node (FN) FPGAs. Each node on the UniBoard has access to two, 2GB Small Outline Dual In-line Memory Modules (SODIMM). These are accessed via two Double Data Rate (DDR) interfaces. Additionally, for high speed data transfer each node on the FPGA has access to 4×10GbE XAUI interfaces. Furthermore, each of the four BN FPGAs have interfaces to 4×8 Low-Voltage Differential Signaling (LVDS) lines for ADC data acquisition [37].

For the transpose operation discussed in Chapter 2.2, each BN is connected to each FN via a high speed mesh. The mesh lines may operate in transmit as well as receive mode. Therefore from an IO perspective the UniBoard is

symmetric. Additionally, a high speed mesh on the backplane or the XAUI interfaces are used to interconnect multiple UniBoards [37].

One UniBoard has the capability to process data from 16 incoming signals. Each BN is responsible for the channelization of four incoming signals q. A BN implements a PFB, which consists of a 16-tap filter along with a 1024-point complex FFT. Due to symmetry in the output, 512 sub-bands are produced for each input. After channelization a subset of the 512 sub-bands are selected for further processing. The selected subset of sub-bands are referred to as iblets ib.

The term iblets is introduced to make a distinction between sub-bands and the selected sub-bands, as one sub-band may be selected for processing multiple times. The iblets are then transferred to the FNs on the UniBoard. Figure 4.3 depicts a block diagram of how the BNs and FNs are interconnected. It can be seen from Figure 4.3 that each BN processes all the sub-bands of four signal paths and each FN processes 96 iblets for all the signal paths [40].

Note that an iblet contains sub-band information for 16 signals. Upon arrival at the FN the 96 iblets are split into four groups of 24 iblets. Each of these iblet groups has a dedicated beamformer unit. A FN therefore has four beamformer units, responsible for the beamforming operation. A beamformer unit implements the multiplication of each signal in an iblet with a specific weight. The output from each of the 16 multipliers are then summed to form a beamlet. Each beamformer unit can produce 256 beamlets, an average of

$$\frac{256}{24} \approx 10 \tag{4.2.1}$$

beamlets per iblet [40]. Figure 4.4 provides a summary of the signal processing chain of the beamformer firmware on the UniBoard.

The FPGAs are controlled and configured via a 1GbE connection as well as an embedded processor, referred to as a soft microprocessor. A NIOSII soft microprocessor is configured in each of the FPGA nodes and has access to the registers in the FPGA. Additionally, a generic unb_os program was developed to be compatible for all UniBoard designs and runs on the microprocessor. All BN NIOSII processors have access to sub-band statistics modules where as all the FN processors have access to the beamlet statistics modules [41]. Furthermore, the NIOSII have interfaces to the following:

- A waveform generator - used to synthesize digital signals
- A general control block - used for clock generation, system information, and Ethernet interface [41].

4.2.3 UniServer Software

UniServer is driver software for the UniBoard and can be used to communicate with the FPGA nodes on a UniBoard. UniServer physically communicates with

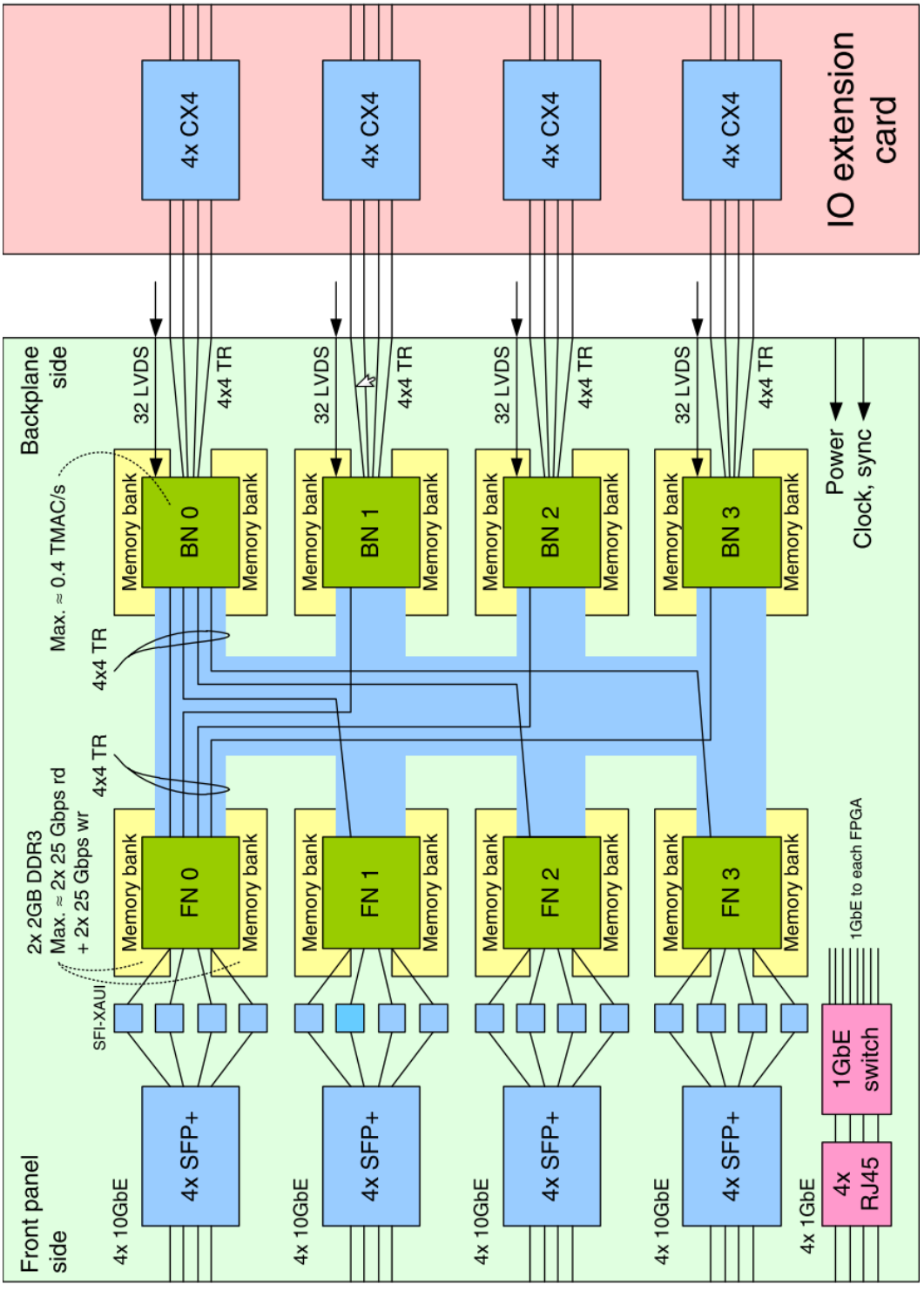

Figure 4.2: UniBoard hardware layout, taken from [37]

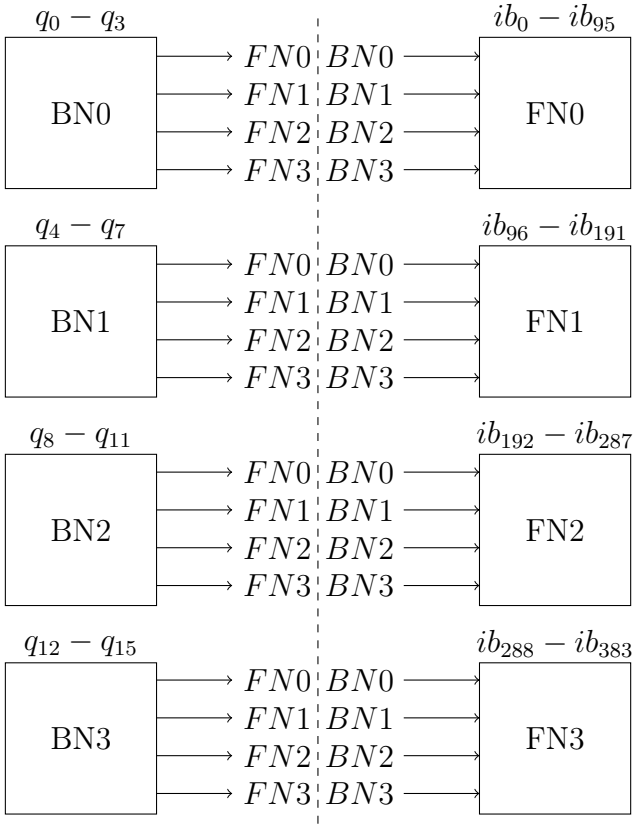

Figure 4.3: Node connections via the high speed mesh

the FPGA nodes by sending UDP packets over an Ethernet connection.

Each node on the UniBoard has a specific IP address, 10.99.*bbb.nnn*, where *bbb* is the board number and *nnn* is the node number. A Local Control Unit (LCU) with a LINUX operating system is used to run UniServer. A unique IP address must be chosen for the LCU, distinguishable from the IP addresses of the nodes on the UniBoard.

Multiple clients (maximum 10) can connect to the UniServer at the same time. Each client can connect to a TCP socket port in the range $3338 - 3347$ [42].

There are three methods, listed below, for a client to communicate with UniBoard via UniServer [42].

- Direct communication by opening a telnet connection and then using the command line
- A MATLAB control script along with the UNIclient class
- A PYTHON control script along with the UNIclientIO class

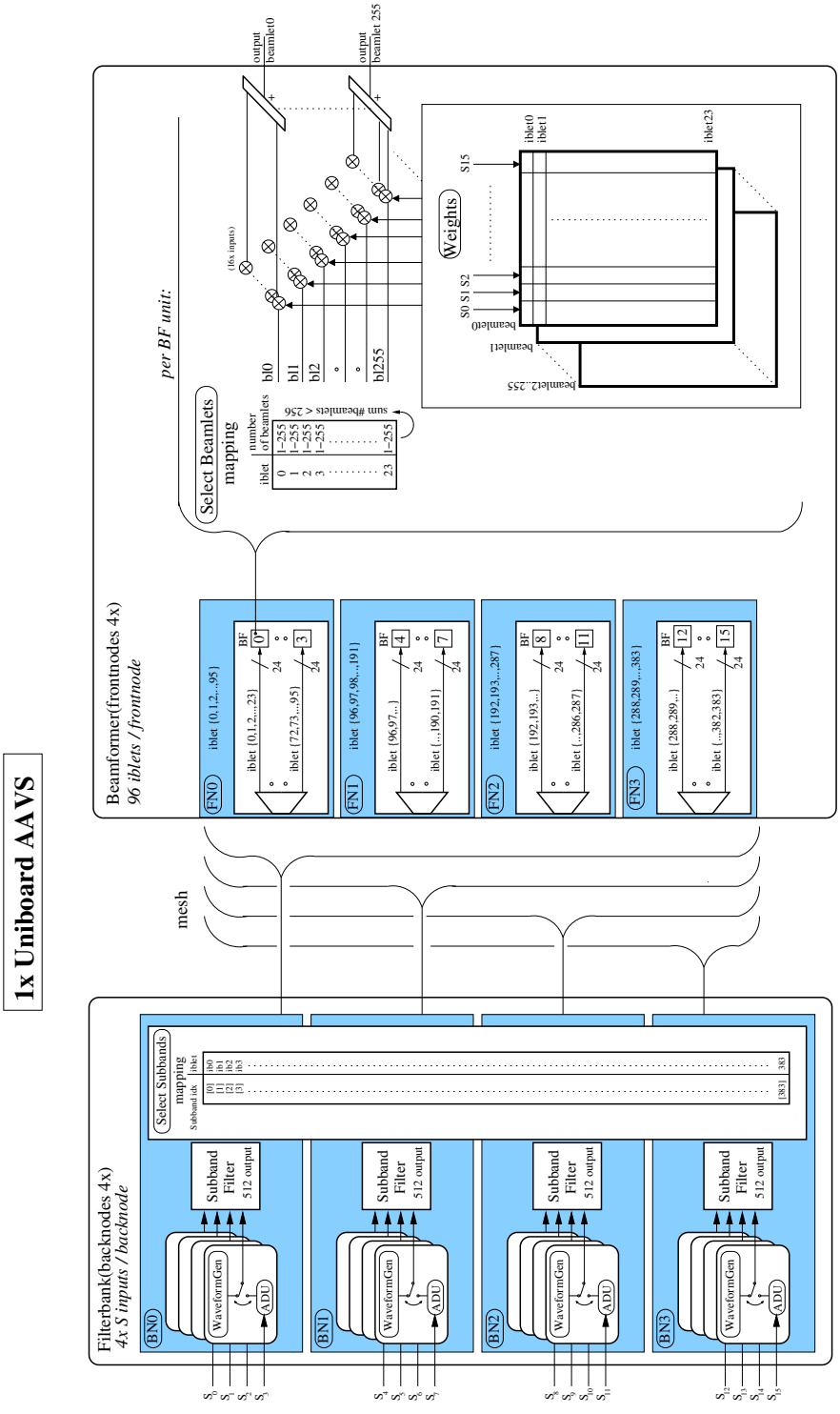

Figure 4.4: UniBoard beamformer firmware description, used with permission of the creator, Leon Hiemstra

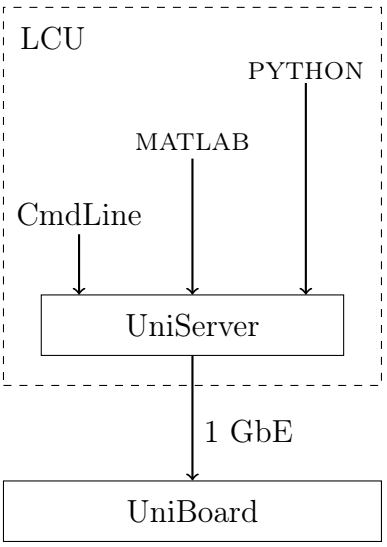

Figure 4.5: Interfaces between the client, UniServer, and UniBoard

Refer to Figure 4.5 for the interfaces between the client, UniServer, and UniBoard.

4.3 Implementation Methodology

A single UniBoard running the beamformer firmware and a PYTHON control script is used to emulate a linear array. Communication with the UniBoard is established using UniServer along with the UNIclientIO class.

The *linear array emulation* exercise provides an overview of how basic array parameters effect the beam of an array, independently of which elements are used in the array. It also focuses on the conventional beamformer topology, discussed in Chapter 3.

4.3.1 Signal, Array Models and Experimental Setup

The BN FPGAs are set to be connected to the waveform generators which are used to synthesize a source. It is assumed that the source is traveling in a homogeneous medium with no interfering signals. Additionally, the source is assumed to be a monochromatic plane wave.

The array emulation produces 181 simultaneous beams in distinct directions. Sixteen incoming signals are weighted equally and combined coherently. It is further assumed that there is no mutual coupling between the isotropic radiating elements.

A UniBoard along with a LCU, connected with a 1GbE link, were used during experimentation. The LCU runs UniServer and executes the control

Table 4.1: Hardware setup

Instrument	Setting
DC power supply	48V
Clock source	200MHz
Pulse generator	1PPS

script. A DC power supply must be used along with a clock source and a pulse generator to produce the Pulse Per Second (PPS) sync signal. Refer to Table 4.1 for the settings of the instruments.

4.3.2 Python Control Script

Figure 4.6 depicts a flowchart of the PYTHON control script. Users may set an inter-element spacing d, operating frequency f, and the direction of the incoming plane wave θ_s. The script produces 181 beams in specific directions, referred to as 181 beamlets bl. These beamlets are produced for a specific frequency, which corresponds to a sub-band which are mapped to all iblets ib. An iblet contains specific sub-band information for 16 frequency domain signals Q_d. To produce a beamlet, a weight w which is dependent on the time delay τ and corresponding phase β, needs to be calculated. This weight $w(bl, ib, Q_d)$ is specific for the beamlet, iblet and signal under consideration.

A TCP connection on port 3341 is established followed by the execution of a number of initialization procedures. Instances of the sub-band and beamlet statistics modules are created in pursuit of offloading processed data via the 1GbE.

This is followed by instantiating the Block Sequence Number (BSN), used for stamping every 1024×8 bits of data with a reference number. Objects are then created for post-processing purposes which is necessary in order to access the statistics modules.

All weights are reset to zero and the data stream is stopped. A 1s integration time is achieved by accumulating for 781 250 clock cycles. The final initialization procedure is to align the mesh between the BNs and FNs.

Sixteen signals, each with a progressive phase shift, are generated in the four BN FPGAs in order to approximate a monochromatic plane wave. After the wave generators are set the PPS is reset and the BSN is triggered. This ensures the synchronization of the waveform generators on the four BNs.

The frequency bin of interest f_b, is then mapped to all iblets. Recall that the total number of beamlets in a beamformer unit must sum to 256. Therefore the number of beamlets for the first iblet in a beamformer unit is set to 232. The remaining 23 iblets each have one beamlet per iblet, creating 256 beamlets for every beamformer unit and therefore 1 024 beamlets per FN. For the purpose of the project only 181 beamlets are needed for ib_0 and additional beamlets

Table 4.2: Default parameters

Parameter	Default
d	$\frac{\lambda}{2}$m
f	156.25MHz
θ_s	0°

are redundant.

The weights for 16 signals in 181 simultaneous distinct directions, with a 1° interval are calculated and applied. After the complex weight multiplication the 16 signals are summed and integrated for one second.

4.4 Verification, Results, and Analysis

The array response is verified by varying basic array parameters and evaluating the response. The default parameters for each experiment are listed in Table 4.2. This choice of frequency corresponds to the 200$^{\text{th}}$ frequency bin after channelization. The first experiment conducted was to verify the beam characteristics, while the remaining experiments included varying a default parameter whilst keeping the other parameters constant. Note that θ_s refers to the direction of the synthesized source whereas θ refers to the direction UniBoard is pointing the electronic beam.

The amplitude A, in dB, of the main lobe can be calculated using,

$$\mathrm{A_{dB}} = 10\log\left(\left(Nw\frac{A}{2}(2^{b_d}-1)2^{b_r}\right)^2 N_{acc}\right), \tag{4.4.1}$$

where N is the number of elements, w is the uniform weight, b_d and b_r are the number of bits used to digitized and re-quantized the signal respectively, and N_{acc} is the number of accumulations. The square arises because the beamlet statistics module measures the power of the signal. Furthermore, the factor 0.5 within the parenthesis is a result of the Fourier transform of a sinusoidal function given by,

$$A\cos(2\pi f_0 t) \iff \frac{A}{2}[\delta(f+f_0)+\delta(f-f_0)]\,. \tag{4.4.2}$$

Equation 4.4.1 is adapted from [43] and for an input signal with $N = 16$, $w = \frac{1}{16}$, $A = 0.8$, $b_d = 8$, $b_r = 7$, and $N_{acc} = 781\,250$ the calculated and measured output is 135.19dB and 135.2dB respectively.

The beam pattern characteristics which were calculated and measured are the HPBW, BW_{NN} and the amplitude of the first SLL relative to the main lobe. Definitions of the above-mentioned performance metrics were formulated in Chapter 2.3.3, and was used here for the calculations. A comparison between

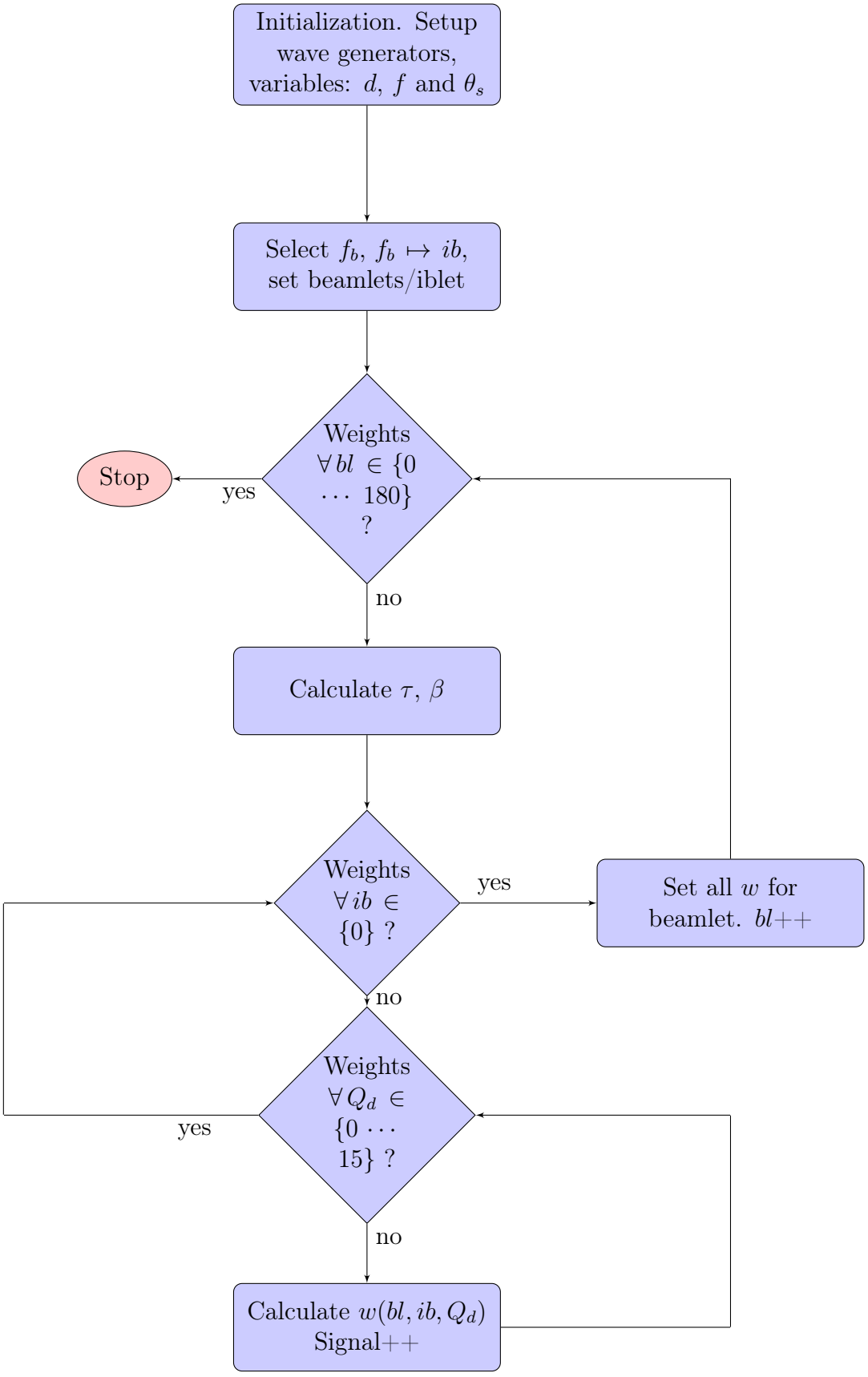

Figure 4.6: Flowchart of emulated beamformer

Table 4.3: Calculated and measured quantities

Parameter	Calculated	Measured
HPBW	6.68°	6.26°
BW$_{NN}$	14.36°	14°
Relative SLL	−13.5dB	−13.27dB

the calculated and measured beam pattern characteristics is given in Table 4.3. It was mentioned in Section 4.3.2 that the response of the array was evaluated in 181 directions, 1° apart. Hence, there is a sub-degree measurement uncertainty in the calculated and measured results listed in Table 4.3.

Whilst keeping the frequency and plane wave direction as given in Table 4.2, the inter-element spacing was varied. Inter-element spacings of $\frac{\lambda}{4}$, $\frac{\lambda}{2}$, and λ were used for the experiment.

As discussed in Chapter 2.3.3 the electrical size of an array determines the width of the main beam. For an electrically large array a narrow main beam is expected. In contrast, electrically small arrays have broader main beams. As the inter-element spacing becomes larger, the higher order side lobes become smaller and vice-versa. For inter-element spacings greater than half a wavelength, grating lobes will appear in the visible region once the array is steered. Grating lobes will also appear in the visible region if the beam is steered to broadside with an inter-element spacing equal to a wavelength.

Figure 4.7 presents the measured results of the experiment. The normalized power output against the pointing direction of the UniBoard is plotted on a dB scale. From this Figure it is verified that the main beam becomes narrower for electrically larger arrays. It is also observed that the higher order side lobes decrease if the electrical length of the array is increased. It was expected that grating lobes will appear within the visible region for an inter-element spacing of one wavelength. In Figure 4.7 the grating lobes appear in the visible region for a spacing $d = \lambda$. Therefore the measured results are as expected.

Another experiment conducted, included varying the direction of the incoming plane wave. During this experiment the frequency and inter-element spacing were set to the default parameters, given in Table 4.2. A monochromatic source with an incoming direction of $\theta_s = -45°$, $\theta_s = 0°$, and $\theta_s = 45°$ were synthesized during the experiment.

It is expected that the signals should add up constructively in the direction of the incoming plane wave and destructively in the other directions. For an incoming source at broadside relative to the array, it is expected that the output will have a maximum response in the $\theta = 0°$ direction. Furthermore, the output from UniBoard should have a maximum response at $\theta = -45°$ and $\theta = 45°$ for a source direction of $\theta_s = -45°$ and $\theta_s = 45°$ respectively.

Figure 4.8 depicts the outcome of the experiment for the three different source directions. From Figure 4.8 it is observed the beamformer emulation

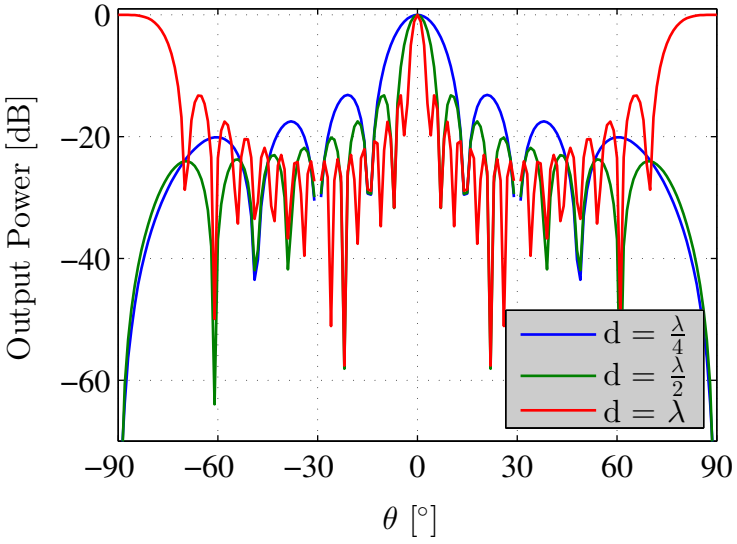

Figure 4.7: Varying the inter-element spacing

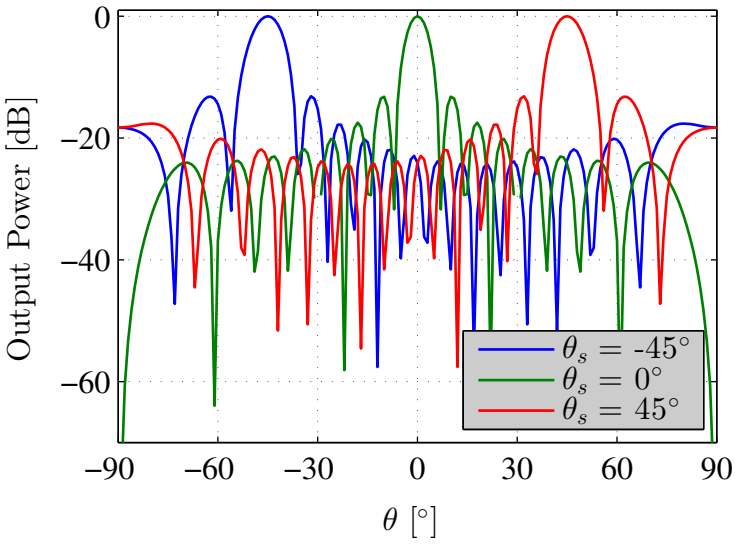

Figure 4.8: Varying the direction of the incoming signal

produces a maximum response at $\theta = 0°$ for a source at broadside. Furthermore, when the source direction is changed to $\theta_s = -45°$ and $\theta_s = 45°$ the beamformer emulation produces a maximum response at $\theta = -45°$ and $\theta = 45°$. For this experiment the predicted and measured outcomes also corresponds accurately.

The final experiment included varying the operating frequency with a constant source direction of $\theta_s = 0°$. The electrical size of an array is dependent on the operating wavelength and corresponding frequency. To investigate the

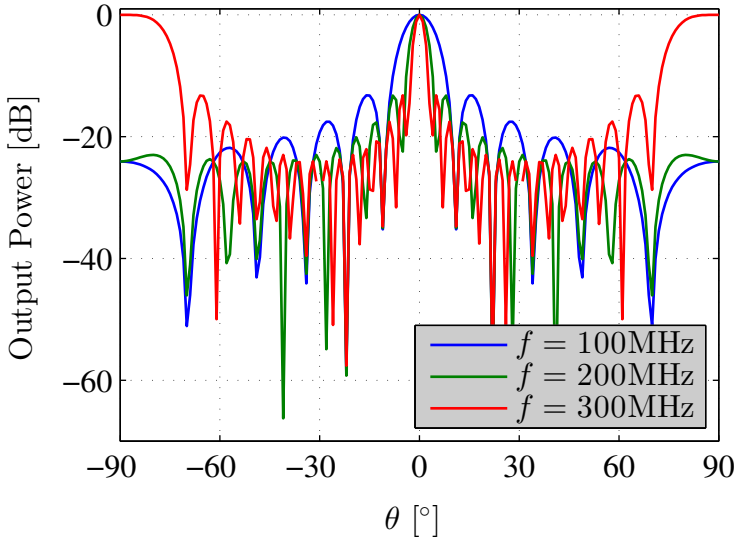

Figure 4.9: Varying the operating frequency

effect of frequency on the array response the inter-element spacing should not be specified in terms of λ. Therefore, for this experiment the inter-element spacing was kept constant at $d = 1$m.

Increasing the operating frequency of the emulated array, with a constant d, effectively increases the electrical size of the array. This is due to the Fourier relationship between a time delay and a phase shift in the frequency domain. As the frequency increases, the main lobe width and higher order side lobes are expected to decrease.

The measured results of the experiment is depicted in Figure 4.9. It is observed that the higher frequency results in a narrower main lobe as well as smaller higher order side lobes. As the electrical size (frequency) of the emulated array increase, grating lobes appear within the visible region and this is verified from Figure 4.9.

4.5 Conclusion

The UniBoard is high performance computing platform with various applications in the Radio Astronomy community. A specific application and motivation for its design is the APERTIF project. By using PAF technology and high speed parallel processors such as the UniBoard, the FoV along with the survey speed of the WSRT will be increased.

A uniformly weighted linear array was successfully emulated using the UniBoard and communication was established using the UniServer. Verification of the array response included evaluating the output power and beam characteristics. Additionally the inter-element spacing, plane wave direction, and

frequency was varied and the response was as predicted.

Chapter 5

Digital Beamformer Implementation

5.1 Introduction

In this chapter, the implementation of a four-element digital frequency domain beamformer will be described. The beamformer is implemented on the ROACH board, which was developed by the MeerKAT team in conjunction with the National Radio Astronomy Observatory (NRAO) [44]. Both research institutions are associates of the Collaboration for Astronomy Signal Processing and Electronics Research (CASPER) group.

The CASPER group provides hardware and open source software libraries to develop Radio Astronomy signal processing instruments [45]. These libraries were used to implement the beamformer on ROACH.

Additionally, a four-element antenna array was built to verify the electronic steering operation of the beamformer.

The design of the antenna array is discussed in Section 5.2. This is followed by an overview of the tools provided by the CASPER group in Section 5.3. A detailed explanation of the beamformer design will be given in Section 5.4. Lastly, the verification, results, and analysis of the antenna array, DBE, and their combined operation are provided in Section 5.5.

5.2 Antenna Array Design

The constructed array is based on the design considerations discussed in this Section. The array consists of four half wavelength dipole antennas with half wavelength spacing. Additionally, the antennas are situated a quarter wavelength above a ground plane, each with a quarter wavelength balun. The operating frequency of the array was chosen to be 600MHz.

The antenna array design choice is based on simulation results, obtained by using the electromagnetic simulation software package FEKO [46]. FEKO

provides a wide range of numerical methods, as well as a hybrid option to solve Maxwell's equations. The Method of Moment (MoM) solver, which is a full-wave solution in the frequency domain, was used during the simulations. MoM is ideal for investigating coupling effects and radiation in free space [47]. Furthermore, the antenna wires and ground plane was simulated using Perfect Electrical Conductors (PEC) and the effects of finite conductivity were not accounted for.

5.2.1 Antenna Element

Due to their ease of construction both the helix and dipole antenna were considered as possible elements for the array. The performance metrics which were considered in choosing an element for the array were the antenna gain, HPBW and ease by which matching circuitry can be constructed.

As discussed in Chapter 2.3.3, the scan angle of the array is limited by the radiation pattern of a single element in the array. An array will not be able to effectively steer the beam past half the HPBW of a single element in the array. The HPBW is therefore important when considering an element for the array.

The antenna gain is of interest as the instrument is not accompanied by a low noise front-end for initial amplification. Antenna elements radiate both in the forward and backward directions. The radiation is reflected by obstacles such as the ground and the effect thereof is modeled using image theory [1]. By including a ground plane the reflected radiation from the back lobe can be controlled in a desirable manner and used to increase gain [28].

Another important figure of merit for antennas is the VSWR, which was discussed in Chapter 2.3.3 and depends on whether the antenna is matched at the feed. Matching techniques for maximum power transfer to a coaxial cable with a characteristic impedance of $Z_0 = 50\Omega$ for both antennas will be discussed.

The Helix Antenna

A helix is a broad-band antenna which can operate in both normal (broadside) and axial (end-fire) mode, however the latter is much easier achieved. Only the axial mode helix antenna will therefore be considered.

The optimal design of a helix antenna has been determined by [28] and is summarized below. It requires the circumference C of the wire to be equal to

$$C = \lambda_0 \,, \tag{5.2.1}$$

where λ_0 is the operating frequency of the antenna. Furthermore, the pitch angle α of the wire should range between $12° - 14°$.

[1] Refer to Appendix B.1, for a refresher on image theory

Table 5.1: Helix antenna dimensions

Parameter	Value
Helix diameter	159mm
Ground plane diameter	499mm
Pitch angle	13°
Number of turns	10

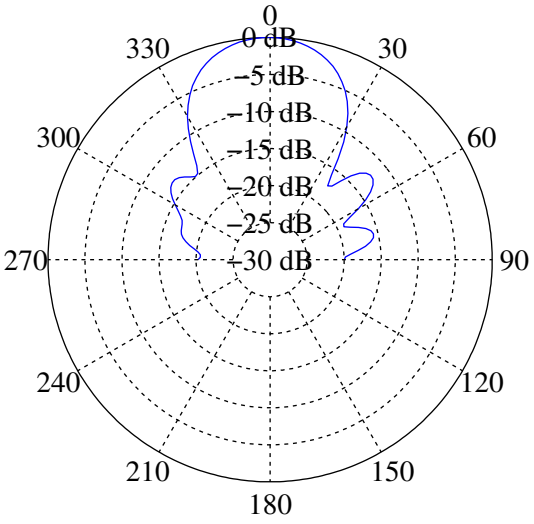

Figure 5.1: Helix antenna radiation pattern at 600MHz in $\phi = 90°$ direction

The gain of a helix antenna can be increased by increasing the number of turns on the helix. As a helix antenna radiates along both axes a ground plane with a diameter larger than $\frac{\lambda_0}{2}$ can be used to ensure radiation along one axis, thereby increasing the gain.

A helix antenna has a resistive input impedance determined by

$$R \approx 140 \frac{C}{\lambda_0} \tag{5.2.2}$$

and can be matched to a $Z_0 = 50\Omega$ coaxial cable as follows. The conducting wire of the first quarter wave turn should be made of a flat strip and gradually transition to normal circular wire. This method improves the VSWR but decreases the bandwidth of the antenna.

An optimum axial mode helix antenna was designed using ANTENNA MAGNUS [48], where Table 5.1 provides a summary of the dimensions. The design was exported to and further simulated using FEKO. The gain of the antenna was found to be 12.58dBi at the operating frequency of 600MHz. Furthermore, the HPBW of the helix antenna was found to be 40.03°. A polar plot of the radiation pattern of the helix antenna is depicted in Figure 5.1.

The Half Wavelength Dipole Antenna

A half wavelength dipole is a resonant antenna which is easy to construct and radiates its energy at broadside.

A horizontal dipole should be placed a quarter wavelength above a conducting ground plane to ensure constructive interference with reflected radiation from the ground plane. By including an infinite ground plane the phase center of the dipole is situated on the ground plane. As the size of the ground plane is decreased the phase center moves upward, toward the dipole. Therefore, no ground plane implies a phase center situated on the dipole. A square ground plane with $l_g = 2\lambda$ is sufficient to ensure a phase center located approximately on the ground plane [49].

The input impedance of a dipole antenna is dependent on the length l and radius a_r of the wire and has been determined by the induced emf method by [28]. For a dipole antenna with a length to radius ratio equal to 10^4, the input impedance is given by

$$Z_{in} = 73 + j42.5\,. \tag{5.2.3}$$

To compensate for the reactance, the length of the dipole can be shortened according to

$$l = 0.48\lambda F\,, \tag{5.2.4}$$

where F is given by

$$F = \frac{\frac{l}{2a_r}}{1 + \frac{1}{2a_r}}\,. \tag{5.2.5}$$

The current distribution on a dipole is balanced but when fed with a coaxial cable the system becomes unbalanced. An unbalance in the system is created by a current flow i_o on the outside of the outer conductor of the coaxial cable. The current results because the inner and outer conductor of the coaxial cable are not coupled to the dipole in a similar manner. This can be corrected for by using a balun. Due to its relative simplicity only the $\frac{\lambda}{4}$ coaxial balun will be considered, refer to Figure 5.2. The current i_o is canceled by connecting the inner conductor arm of the dipole, to the outer conductor of the coaxial cable, as depicted in Figure 5.2. The length should be a quarter wavelength long, so as to not short-circuit the current at the antenna feed which would prohibit radiation [28].

A $\frac{\lambda}{2}$ horizontal dipole antenna above a ground plane was simulated using FEKO, where the dimensions for the simulation are listed in Table 5.2. Furthermore, the $\frac{\lambda}{4}$ coaxial balun was not included in the simulation as FEKO provides a balanced feed. The gain and HPBW of the antenna was found to be 7.48dBi and 72.86° respectively. Figure 5.3 illustrates the radiation pattern of the dipole antenna.

There is a trade-off between the gain and HPBW for both antennas. The helix antenna has a higher gain but a narrower HPBW and the dipole antenna has a lower gain but a wider HPBW. For this application of an antenna array,

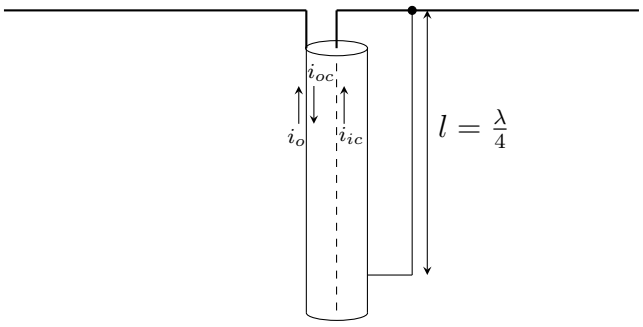

Figure 5.2: Dipole with $\frac{\lambda}{4}$ balun

Table 5.2: Half wavelength dipole antenna dimensions

Parameter	Value
Length	249mm
Conductor radius	0.255mm
Height above ground plane	124mm
Ground plane length	1m
Ground plane width	0.5m

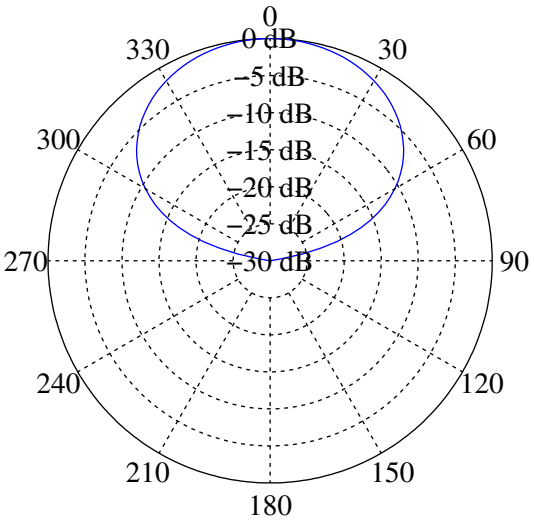

Figure 5.3: Half wavelength dipole antenna radiation pattern at 600MHz in $\phi = 90°$ direction

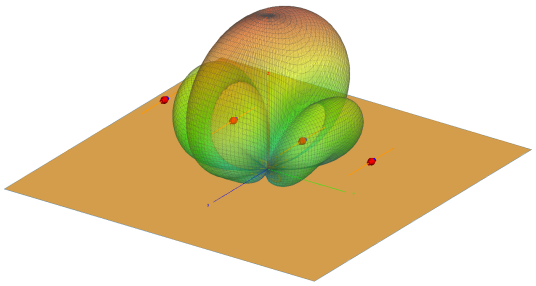

Figure 5.4: Three dimensional radiation pattern of the antenna array

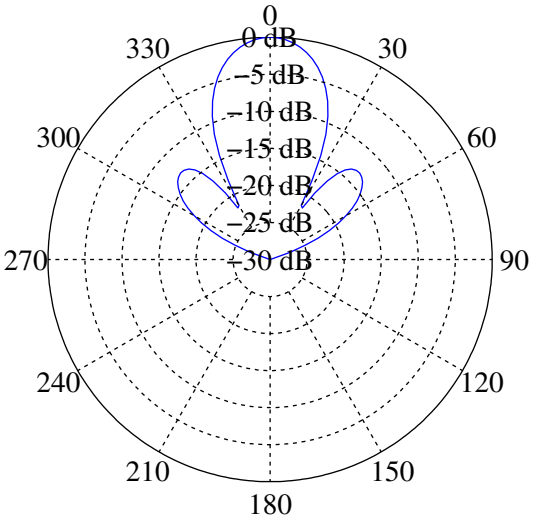

Figure 5.5: Antenna array radiation pattern at 600MHz in $\phi = 90°$ direction

the wider HPBW is a more important figure of merit than the higher gain. Additionally, the matching procedure for the dipole antenna is relatively simple, compared to that of the helix [28]. Therefore it was decided to use the $\frac{\lambda}{2}$ dipole antenna for the antenna array.

5.2.2 The Antenna Array

In Chapter 2.3.3 it was shown that the inter-element spacing must be $d \leq \frac{\lambda}{2}$ to avoid grating lobes appearing in the visible region, once the array is steered. Also recall that a larger inter-element spacing produces a narrower beam. The inter-element spacing was therefore chosen to be $d = \frac{\lambda}{2}$. Figure 5.4 depicts a three dimensional view of the array simulated using FEKO, along with the radiation pattern produced at broadside. The gain of the array at 600MHz was found to be 12.83dBi and the HPBW to be 20.02°. The normalized radiation pattern of the array is plotted in Figure 5.5.

The theoretical scan limit imposed on the array by the $\frac{\lambda}{2}$ spacing is $\pm 90°$.

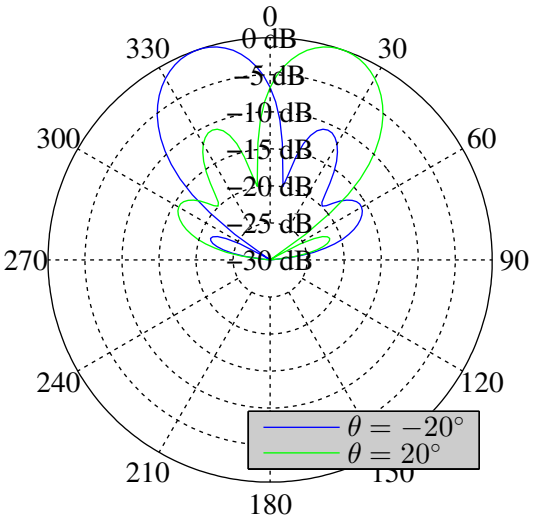

Figure 5.6: Antenna array steered towards $\theta = \pm 20°$

Table 5.3: Antenna array dimensions

Parameter	Symbol	Value
Length	l	250mm
Inner conductor radius	a_r	0.255mm
Inter-element spacing	d	250mm
Height above ground plane	h	125mm
Length of ground plane	l_g	1m
Width of ground plane	w_g	0.5m

It is also known that the array would not be able to scan effectively past half the HPBW of its individual elements. Additionally, mutual coupling between the elements cause the main lobe to deviate from the intended direction. When simulated, the array can scan across a 40° range with an angle distortion of less than 1°. For larger scan angles the limiting factors are the HPBW of individual elements and mutual coupling effects. Figure 5.6 shows the normalized radiation pattern of the array when the array is steered towards ±20°.

The antenna length l, inter-element spacing d, and the height h above the ground plane as well as its dimensions $l_g \times w_g$ are depicted in Figure 5.7. A UT-85-Form wire was used for the construction of the antenna array, where the final dimensions are listed in Table 5.3.

According to Equation 5.2.4 and Figure 5.7 the length should be trimmed to $0.479\lambda = 239$mm for the specified length and wire radius. This is necessary in order to compensate for the input reactance. However, the length of the dipole was kept at approximately half a wavelength. It is therefore expected that the elements will resonate at a lower frequency. This approach was taken

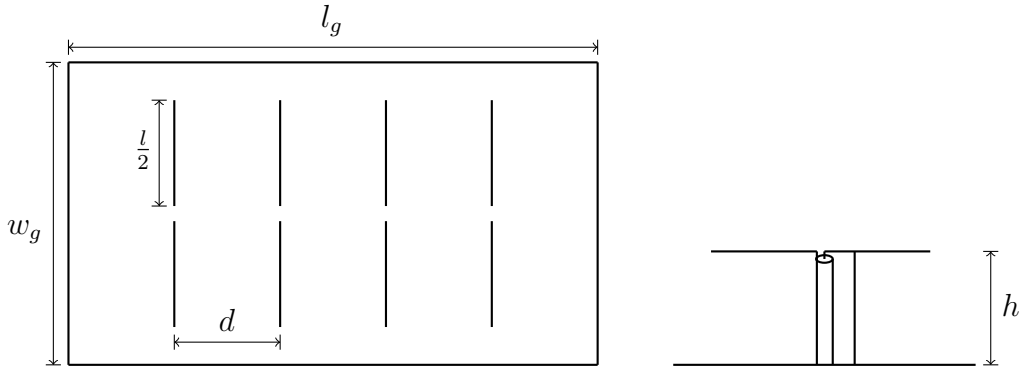

Figure 5.7: Antenna array configuration

as there is a difference between calculated, simulated and measured values. Upon completion of initial antenna measurements, the lengths were shortened to ensure resonance at 600MHz. During the trimming process all elements of the array were connected and fed by a Vector Network Analyzer (VNA). This was done to ensure that mutual coupling effects would be accounted for.

5.3 CASPER Tools for Developing Radio Astronomy Instrumentation

The CASPER group is an international community established to streamline the development of Radio Astronomy instrumentation.

CASPER provides reconfigurable hardware along with platform independent, software, and gateware libraries. In addition, CASPER provides various high speed ADC boards with bandpass sampling capability for data acquisition.

The approach taken by CASPER is to ship hardware with a test design, which users could easily replace with a unique design specific to their high performance signal processing needs.

5.3.1 CASPER Hardware Employed

As mentioned in Chapter 2.2.2, Radio Astronomy instrumentation have the need for high performance parallel processors. Therefore, majority of the CASPER processing boards are based around Xilinx FPGAs.

The Berkeley Emulation Engine (BEE2) was developed in 2005 and have five Virtex-II FPGAs available for data processing. The Interconnect Break-Out Board (IBOB) has one Virtex-II FPGA and was designed to obtain and pre-process digitized signals before the data is transfered to BEE2 boards.

Table 5.4: KATADC component details

Component	Manufacturer	Part number
RF Switch	Peregrine semiconductor	PE4246
Attenuator	Mini-Circuits	LAT-0 series
Variable Attenuator	Hittite	HMC624LP4
RF Amplifier	Sirenza Microdevices	SBB-2089Z
RF Translator	Pulse Engineering	CX2156
ADC	Texas Instruments	ADC08D1520

Favorable features from both these boards were combined in 2009 to produce the ROACH processing board [45].

The ROACH board along with two KATADC digitizers were used during the execution of the project. An overview of the key features of both the KATADC and ROACH board are provided below. The following hardware specifications were obtained from [45, Hardware section].

KATADC

Figure 5.8 depicts a block schematic of the KATADC digitizer. The KATADC digitizer is fitted with a low power, CMOS, differential ADC along with preceding analogue circuitry.

The ADC has 8 bits of resolution, with a dual input of which the maximum sampling rate is 1.5GHz per data stream. The two converters in the ADC can optionally be interleaved to sample at 3GHz. Due to the high sampling rates provided by the ADC, it can be used for bandpass sampling applications.

There are four SMA connectors for single-ended inputs to the KATADC: a clock, two RF signals, and sync pulse. A Z-DOK+ connector outputs the digitized signals along with a digital clock to the ROACH board.

The first component in the RF chain on the KATADC, is a 50Ω non-reflective RF switch. This is followed by a variable attenuator which can provide up to 31.5dB attenuation. The attenuation can be adjusted in 0.5dB steps and operates from DC − 6GHz. To provide further control over the power levels, the KATADC is also fitted with an amplifier. The amplifier is fixed and has a 20dB gain over a frequency range of 50 − 850MHz. An RF translator transforms the single-ended signals into differential signals in order to cancel common mode noise. Since the input impedance of the ADC is 100Ω, the differential signal propagates through the matching circuitry before digitization. Refer to Table 5.4 for a list of the components on the KATADC.

ROACH

A block diagram of the ROACH board is depicted in Figure 5.9. The ROACH board provides up to 400 Giga Operations per Second (GOPS) of processing

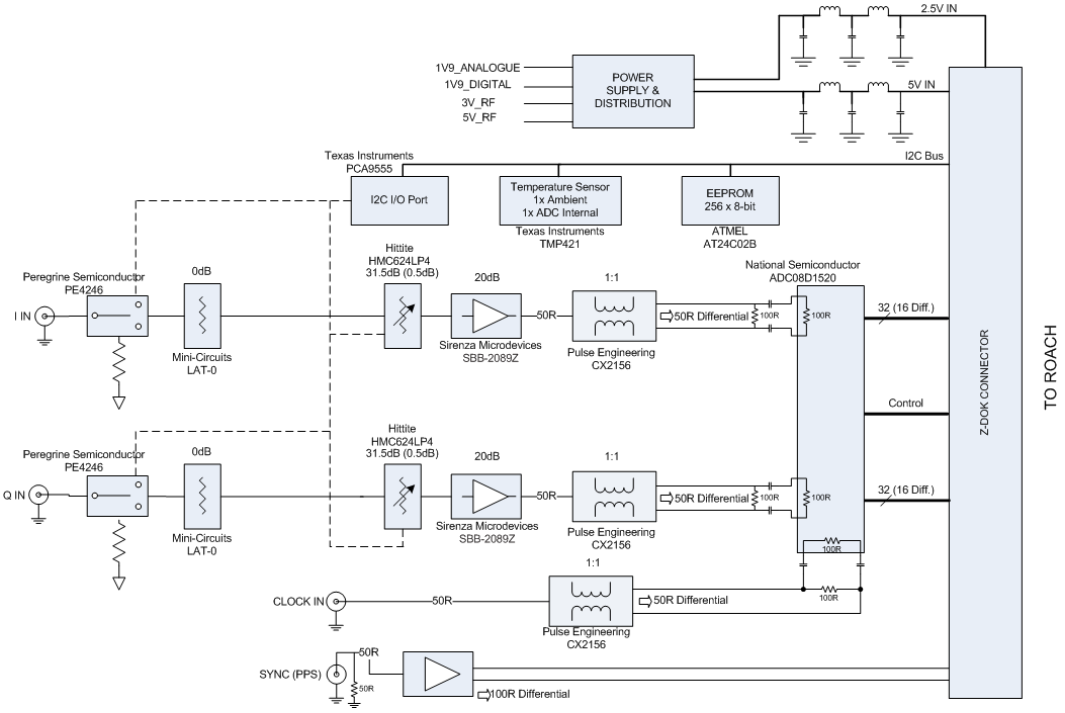

Figure 5.8: Block diagram of the KATADC, adapted from [50]

Table 5.5: ROACH component details

Subsystem	Core	Part number
Signal Processing	Virtex-V Xilinx FPGA	XC5VSX95T-1FF1136
Embedded Processor	AMCC PowerPC	PPC440 EPx
Monitor/Management	Actel FPGA	AFS600

power and has three subsystems. The core of the signal processing subsystem is an Xilinx Virtex-V FPGA. Interfacing with and programming the FPGA is the objective of the embedded processor subsystem. The third subsystem monitors and manages the temperature and power supplies on the board. Table 5.5 lists the core of the three subsystems on ROACH and provides their respective part numbers.

The FPGA is equipped with Configurable Logic Blocks (CLB) as well as embedded logic and memory, for optimization. The FPGA has 640 DSP48E slices, which are dedicated 25×18 bit multipliers. Additionally, each DSP48E slice contains an adder and accumulator. There are 14 720 Virtex-V slices arranged in two 160×46 array cells. A maximum memory capacity of 1 520Kb may be used as distributed RAM. Each Virtex-V slice contains four Look Up Tables (LUT) and four flip-flops. Furthermore, the FPGA is equipped with 8 784Kb of dedicated Block RAM (BRAM). There are 244, 36Kb BRAM blocks which can optionally be split into 488, 18Kb BRAM blocks [51]. In addition

to the on-chip memory the FPGA has access to Static RAM (SRAM) via two Quad Data Rate (QDR) lines and Dual In-line Memory Modules (DIMM) via a DDR line.

Along with the interfaces mentioned above, the FPGA has sixteen General Purpose Input Outputs (GPIO), of which four are connected to external LED lights. Two 40 differential pair, Z-DOK+ connectors are used for data transfer from the ADCs to the ROACH board. Additionally, the FPGA also has four CX4 10GbE serial connectors, used for offloading data or interconnecting multiple boards. A PowerPC embedded processor communicates with the ROACH via an External Bus Controller (EBC). The processor runs a LINUX based operating system and has an Ethernet connection for external communication with ROACH. The BRAMs and software registers of the FPGA can be accessed through the PowerPC.

For clock distribution and management the FPGA has six Clock Management Tiles (CMT). Each CMT has two Digital Clock Managers (DCM) and one Phase Locked Loop (PLL). A 100MHz on-board crystal can be used to clock the FPGA which can optionally be PLL to multiples of 100MHz by the DCM. An external clock can be provided via a SMA connection, which can also be PLL to another frequency. Another clocking option for the FPGA is to use the digital clock provided by the ADC. This should be used to sync data from the ADC with the FPGA. Only one ADC provides a clock signal to ROACH if two ADCs are used. The two ADCs will either start-up in phase or in integer values of 90° out of phase.

5.3.2 CASPER Software Employed

CASPER provides users with software to easily communicate and design instrumentation for ROACH. Details of the software provided are found in [45, Software section] and is summarized below. The Berkeley Operating system for Re-Programmable Hardware (BORPH) was developed specifically for interfacing with FPGA based architectures. BORPH executes a hardware design on the FPGA and allows users to interface with the design as if it were software executing on a CPU. The PowerPC on ROACH runs BORPH and users can directly communicate with the FPGA using BORPH .

Communication with ROACH can also be established through a network by using the Karoo Array Telescope Control Protocol (KATCP). KATCP is a daemonized server that runs under BORPH and listens for TCP connections. KATCP supports multiple connections and can be used by opening a Telnet connection on port 7147. CASPER also developed the *corr* package which contain PYTHON wrappers for KATCP, further simplifying interaction with ROACH.

The MATLAB, SIMULINK, System Generator, Embedded development kit (MSSGE) toolflow [45, Toolflow section], is a highlevel design tool for developing designs for the ROACH board. In SIMULINK a toplevel schematic is

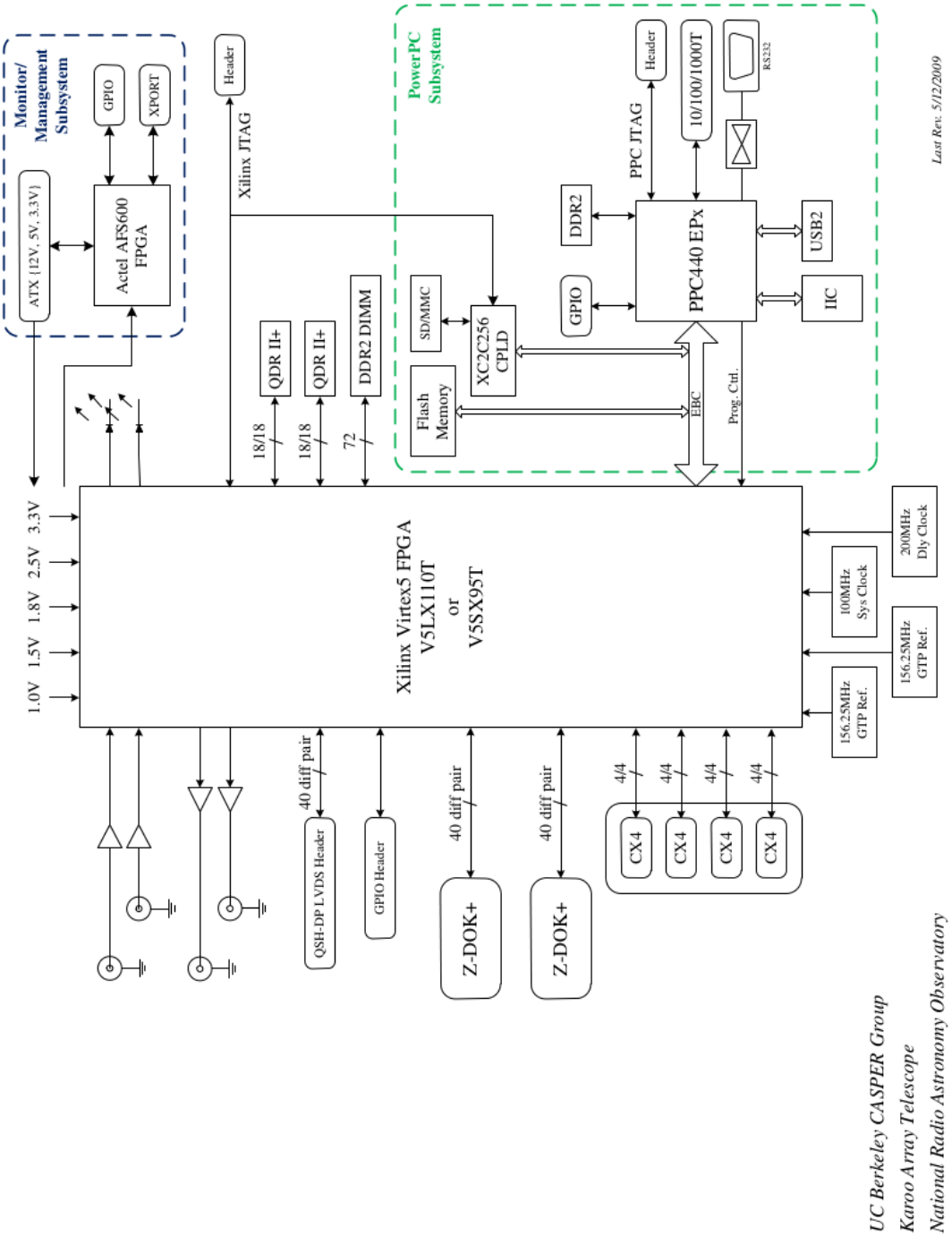

Figure 5.9: Block diagram of ROACH, adapted from [52]

created using the libraries provided by CASPER and sub-blocks can be created in SIMULINK by using MATLAB masking scripts. The schematic is then compiled into HDL code by the Xilinx System Generator tool. The System Generator tool also allows the user to simulate a design using SIMULINK. A bitstream, used to program the FPGA, is generated by the Xilinx Embedded Development Kit (EDK). The MSSGE toolflow combines these environments and the user can obtain a bitstream with one-click to compile a schematic design into a bitstream.

The SIMULINK based CASPER DSP and Xilinx Platform Studio (XPS) libraries were developed to aid in design transfer when the hardware is upgraded. This reduces the development time for Radio Astronomy instrumentation. The DSP blockset contains all necessary DSP related functions for Radio Astronomy purposes. All hardware related blocks such as the KATADC, form part of the XPS blockset. General logic blocks can be found under the Xilinx System Generator blockset. Color is used to easily differentiate between the different functionalities of each blockset. All DSP related blocks are green, yellow is reserved for XPS blocks, and the Xilinx blocks are blue, this is in reference to the beamformer design depicted in Figure 5.11, which will be discussed in the following Section.

5.4 Beamformer Design

A digital beamformer was designed and implemented on the ROACH processing board. The beamformer coherently combines four incoming data streams in the frequency domain. Uniform weighting is applied to the four elements of an arbitrarily spaced linear array. Digitization is performed at $f_s = 800$MHz using two KATADC boards. This provides a 400MHz bandwidth with Nyquist zones as indicated in Figure 5.10. The instrument operates over the entire band and produces one beam per sub-band. The design of the beamformer is detailed in Section 5.4.1 and the control scripts to configure and communicate with ROACH will be described in Section 5.4.2.

5.4.1 Gateware

Figure 5.11 illustrates a block diagram of the implemented beamformer pipeline on ROACH. The number of bits at each processing block is indicated by $nb.bp$, where nb is the number of bits and bp represents the position of the binary point.

Two KATADC yellow blocks are included in the design for digitizing the four incoming signal paths. ROACH is clocked at 200MHz which is a demux of the 800MHz clock signal from KATADC 0. Four parallel time samples are therefore available from four data paths on every ROACH clock cycle.

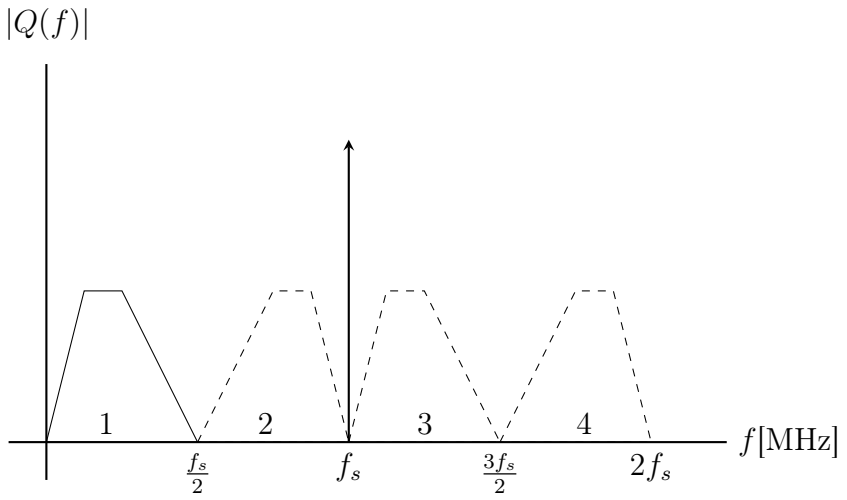

Figure 5.10: Nyquist zones for $f_s = 800$MHz sampling rate

A digitally synthesized sync pulse is generated on ROACH to ensure synchronization throughout the design. The calculation of the sync pulse period will be discussed after the overview of the gateware design.

After digitization, the signals are channelized by using a real PFB. The PFB consists of a four-tap Hamming windowing function and a 512-point radix-2 FFT. This provides a frequency resolution of 1.5625MHz. Due to the symmetrical output of a real PFB, only half of the frequency bins produced requires further processing. The PFB outputs even and odd frequency bins, in parallel on each FPGA clock cycle.

Subsequent to channelization, the phase of each frequency bin can optionally be rotated by applying a fine delay. As this forms the heart of the beamformer design it is discussed in more detail below.

Once the phase has been rotated, the signals are decomposed into their real and imaginary parts. To provide user control over the beamformer output the data paths are then either nulled or uniformly weighted. The decomposition and weighting is indicated as a joint operation by the multiplication symbol in Figure 5.11.

After the weighting, the signals are summed in order to calculate the output power. The signals are not re-quantized before accumulation, thereby retaining the signal dynamic range. In practice signals are re-quantized before accumulation to limit bit growth. For a FPGA clocked at 200MHz the bit growth for a one second integration time is 28 bits. For this reason, the accumulated data is written into 64 bit BRAMs.

The implemented design contains nine input registers. Each KATADC has a control register from which the two data paths on each board can be enabled or disabled. The attenuation of each signal path can also be set using

these registers. A general control register is included for resetting counters, enabling fine delay offsets, and triggering snapshot captures of ADC data. Four fine delay and a weights register are included to set the phase rotation and weighting of each signal path. An accumulation register is also included to be able to set the accumulation length from software.

Furthermore, the design includes five output registers. Four registers are used to control the LED lights on ROACH. LED lights 0 and 1 correspond to a sync and new accumulation pulse generation and LED lights 2 and 3 are reserved for KATADC 0 and 1 clipping. The design includes an accumulation counter which is also written to an output software register.

The design employs 97% of the slices and 57% of the DSP48Es available on the FPGA. A total of 4 968kB memory is in use and 67% of the available BRAM blocks are occupied. The beamforming operation easily fitted onto the FPGA architecture. However, not enough processing power remains to implement a cross correlation of the antennas. An adaptive beamforming architecture can be implemented if the correlation between the antennas can be measured [13]. Hence, the design is based on a conventional beamformer topology, where phase is rotated and the outputs are summed.

Fine Delay

The fine delay is implemented using the *finedelay_fstop_prog* block, available from the CASPER DSP library. A linear phase rotation, which increases monotonically, is applied over the entire frequency band. Furthermore, the gradient of the linear line can optionally be set by using the fine delay software registers.

A sine and cosine LUT with a 10 bit depth provides a phase resolution β_{res} as given by,

$$\begin{aligned} \beta_{res} &= \frac{360^\circ}{2^{10}} \\ &= 0.35^\circ , \end{aligned} \tag{5.4.1}$$

for frequency bin 1. This limits the phase resolution of the higher frequency bins.

To increase the phase resolution over the entire band, a binary point was enforced at bit 5 of the fine delay software registers. By enforcing the binary point, the amount of phase rotation β applied to each signal path is modified to

$$\beta = f_b f_d 2^{-5} \frac{360^\circ}{1024} \tag{5.4.2}$$

where the factor f_d is the integer value written to the fine delay software register, f_b is the frequency bin, and the constant 2^{-5} accounts for the binary point. The corresponding pointing direction θ of the beamformer is calculated

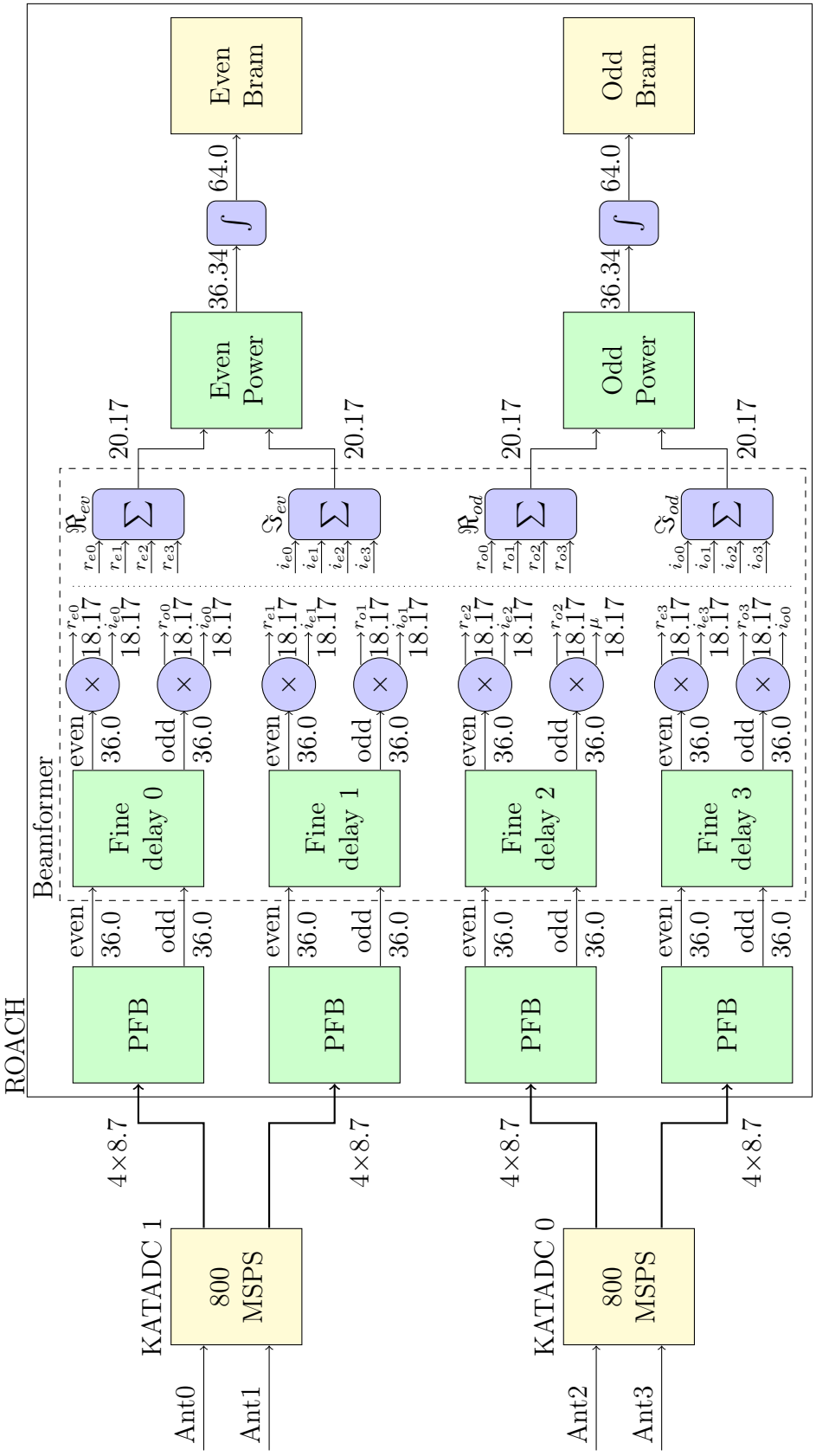

Figure 5.11: Beamformer pipeline design

as follows,

$$\theta = \sin^{-1}\left(\frac{\lambda\beta}{2\pi d}\right) . \tag{5.4.3}$$

Sync Pulse

A digitally synthesized sync pulse is used to manage the data stream throughout the design. The pulse acts as a reset and can also be used for timing. A sync pulse arrives at a DSP block one clock cycle prior to a valid data frame. The DSP block can then reset to its initial state in time for the arrival of the first data sample in the data frame. Furthermore, the sync pulse undergoes the same amount of latency as the data within a DSP block, thereby managing the entire data stream. The pulse width should be equal to one clock cycle and the sync must be periodic [53].

The periodicity can be determined by the number of clock cycles it takes to process a data frame. Every process in the design that affects a frame of data needs to be accounted for when the periodicity is calculated. This is to ensure that a sync pulse is not issued whilst valid data is being processed.

The minimum sync period T_{sync} can be calculated using,

$$T_{sync} = N_{acc} \cdot N_{tap} \cdot \text{LCM}\,(\text{reorder orders}) \cdot \frac{\text{FFT size}}{\text{Simultaneous inputs}} , \tag{5.4.4}$$

where the reorder orders refers to the reorder blocks in the FFT. These are used to perform the bit-reversal operation. Furthermore, it is seen that the number of accumulations N_{acc}, number of taps in the PFB FIR filter N_{tap}, and the size of the FFT should also be accounted for. Another factor influencing the sync period is the number of simultaneous inputs. Any integer multiple of the minimum sync period may be used to synchronize the design [53]. For the design implemented on ROACH, the minimum sync period was scaled by 512 to produce a sync pulse every 3 670 016 clock cycles.

5.4.2 Software Control Scripts

PYTHON control scripts were written to initialize, configure and control the design on ROACH. An initialization script programs the ROACH board and performs a calibration algorithm. A second script is used to measure the output of the beamformer.

Cable length and phase differences between the ADCs can be compensated for by calibration. The calibration technique is based on incoming signals from a known source, with a known position. For the purposes of the project, the calibration technique assumes a source at broadside. During the calibration process, three sets of two data path comparisons are made. The output of the beamformer is continuously logged whilst the phase of one of the two data paths are rotated through all possible phase rotations. The position of

the maximum beamformer output determines the signal path that requires a phase offset during an observation. The three sets of comparisons made during calibration are *a*) the two data paths on KATADC 0; *b*) the two data paths on KATADC 1; and *c*) the two longest path lengths on each KATADC. Each data path is then assigned an offset based on the calibration technique and the offset is applied when an observation is made.

The operating frequency must be set during an observation. Additionally, it must be specified whether the beamformer is operating in the first or second Nyquist zone; if it is not specified a first Nyquist zone is assumed. The inter-element spacing and accumulation length can also be set in software, a default of $d = \frac{\lambda}{2}$ and 125ms is used respectively if the parameters are not set. Operating modes for the script can be set and may include one or a combination of the following *a*) observe the frequency output; *b*) display snapshots of ADC data; *c*) steer the beam in a specific direction and log the output *d*) steer the beam in all possible directions whilst logging the output.

For steering the digital beam in one or all possible directions the following applies: The antenna used as the reference point depends on the direction of the incoming signal. As only delays can be inserted into the signal paths, the reference antenna should be the antenna furthest from the source. When the source crosses the array at broadside the reference antenna position changes. This is accounted for in the script.

A flowchart of the section in the script for steering the beam in all directions is depicted in Figure 5.12. ROACH steers the beam and evaluates the output in directions ranging from $-90° \leq \theta \leq 90°$. It is first determined whether the pointing direction of ROACH is to the left, right, or at broadside. This is necessary in order to select the appropriate reference antenna. Due to the relationship between the phase applied and the steering direction, ROACH cannot point in 181 distinctive directions over the entire frequency band. The script ensures ROACH only directs and evaluates directions relating to a unique phase rotation.

5.5 Verification, Results, and Analysis

The antenna array and DBE were verified separately and in combination.

Subsection 5.5.2 discusses the procedures undertaken to verify the antenna array. Additionally the results obtained and the analysis thereof will be discussed.

An anechoic chamber was used to measure the gain and beam pattern of the antenna array. A two port VNA, four way 0° power divider, and a broadband 0.3−6GHz Log-Periodic Dipole Antenna (LPDA) were used during the antenna array measurements.

The active reflection coefficient of individual antenna elements were measured using a four port VNA, outside the anechoic chamber. Before the mea-

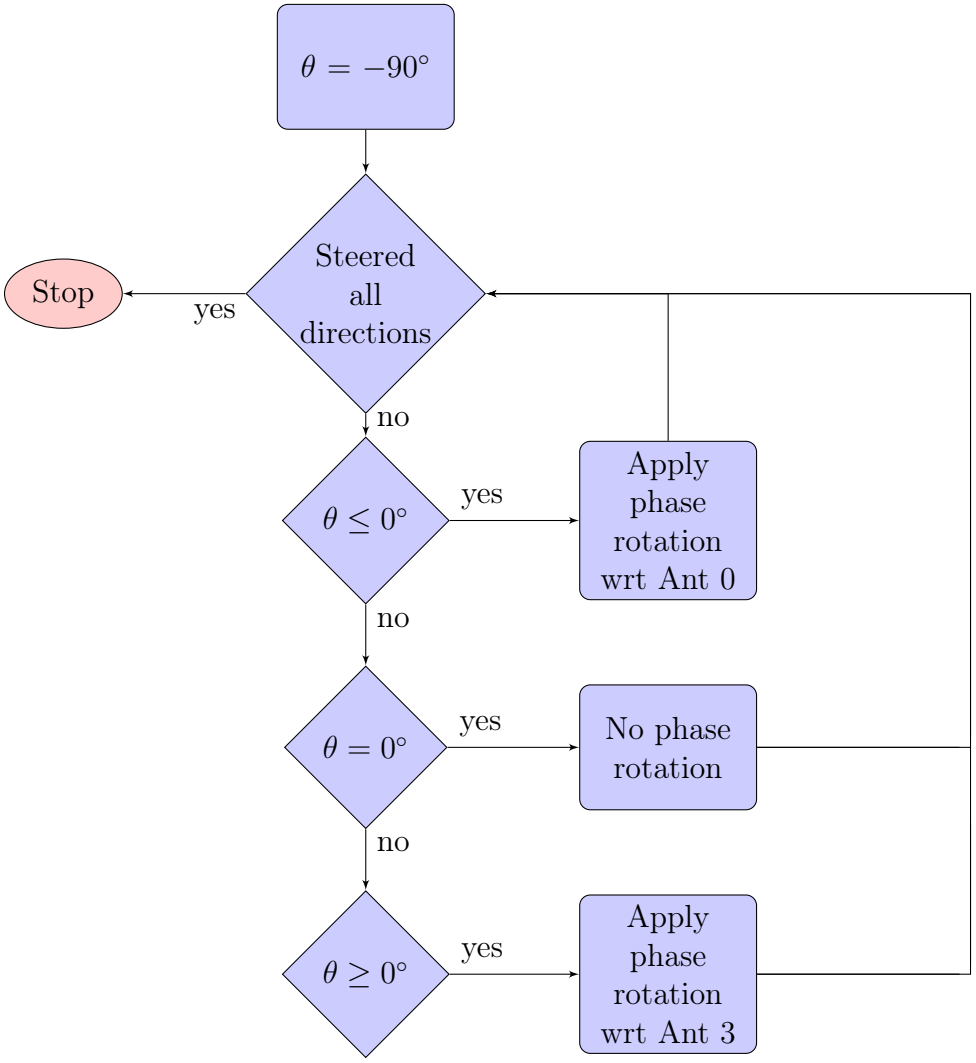

Figure 5.12: Flowchart of beamformer steering

surements took place, it was established that the environment would not effect the results.

Whilst the antennas were connected to the VNA, metallic structures were placed in front of the antennas. The metallic structures were positioned at various distances from the antennas until no variation in the output of the VNA were observed.

The Spurious Free Dynamic Range (SFDR), gain and beam steering capability of the DBE were measured. A noise generator, signal generator, custom made cables, and a four way 0° power divider were used during the measurements. Subsection 5.5.3 discusses the results and analysis of the DBE verification procedures.

Furthermore, the antenna array along with the DBE were verified in the

anechoic chamber. The experiments conducted and the results obtained are discussed in Subsection 5.5.4. The mechanical tolerances and dimensions of the anechoic chamber affected the results obtained. Therefore, the anechoic chamber and the limitations it posed are first discussed in Subsection 5.5.1.

5.5.1 Anechoic Chamber

The anechoic chamber has two antenna positioners indicated by A and B in Figure 5.13. Antennas at either of the positioners can be connected to either port 1 or port 2 of the VNA, situated outside the anechoic chamber.

Antenna positioner A is a rotary pedestal and can rotate 360° about its axis. The pedestal can be moved forward, decreasing the distance between the two positioners. The maximum distance between the two positioners is 5.289m. Antenna positioner B is movable in a horizontal (indicated by x in Figure 5.13) and vertical (out of the page) direction. The room has a walkway to the left of the pedestal and the rest of the room is filled with a foam pyramidal absorbent material. Note that during experimentation the antennas at positioners A and B were separated by a distance greater than their far-field distance, which for the antenna array is calculated to be 2.25m at 600MHz.

The absorber has a pyramidal structure which transforms the input impedance of free space (at pyramidal tip) to that of a lossy material (at pyramidal base). Incident radiation is then attenuated by scattering and absorption. The frequencies absorbed by the pyramids is based on the physical size of the absorbers. For low frequencies (longer wavelengths) large absorbent material is needed and for higher frequencies (shorter wavelengths) smaller absorbent material is needed [54]. The pyramidal absorber in the anechoic chamber has a base of 102mm × 95mm and a height of 300mm. For the dimensions specified, the material optimally absorbs incident radiation above 2GHz. The operating frequency of the antenna array is 600MHz which is less than the lower cut-off frequency of the absorbers in the anechoic chamber.

As the chamber has been designed for operation above 2GHz, the room has not been characterized for low frequencies. Therefore, the quiet zone for the room at 600MHz has not been determined. For reasons stated above, it is expected that reflections will occur in the room during experimentation.

Ambiguities in the results also occur due to the rotational capability of positioner A. The rotational capability of positioner A has a tolerance which causes an angular error of 0.76° with respect to positioner B. The error was calculated by directing a laser to positioner B from the pedestal. A marker was placed and positioner A was manually rotated to its tolerated rotational capability. The new position of the laser light was marked at position B. The difference between the markers were measured to be 70mm, which over a 5.289m distance results in a 0.76° angular difference at positioner B.

The alignment of the antennas at positioner A and B is important in order to obtain accurate results. This should ideally be done with laser shaft

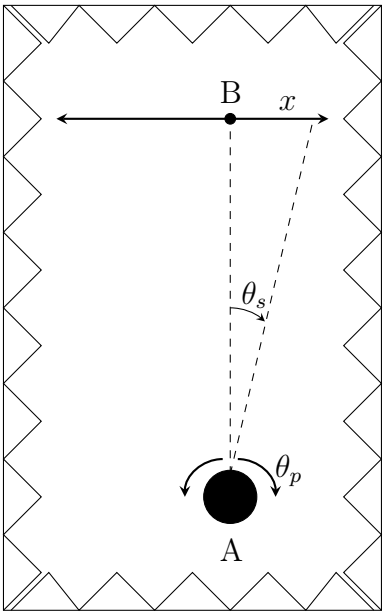

Figure 5.13: Top view of anechoic chamber

alignment equipment, which was not available. However, it is known that the midpoint of the pedestal is aligned with the midpoint of the tracks used to move positioner A. The slots of the tracks continue up to and are visible at positioner B. The midpoint of the slots were determined and positioner B was moved to the center point of the slots.

A weight hanger was made use of to as far possible accurately align positioner B with the midpoint of the slots of the tracks. The alignment was conducted to the best efforts but errors could persist due to alignment errors. By making this alignment the positioners are closer to one wall of the anechoic chamber, as depicted in Figure 5.13. It is therefore expected that more reflections will occur from this wall.

From here forth, the following conventions θ_s, θ_p, and θ are used to denote source direction, pedestal orientation, and beamformer pointing direction respectively.

5.5.2 Antenna Array

Reflection Coefficient and Mutual Coupling

The active reflection coefficient and coupling between the elements in the array were measured using a four port VNA. This is necessary to account for the presence of mutual coupling when all antennas are excited. As expected, Figure 5.14 illustrates that the antennas in the array resonated at a lower frequency of 545MHz. Figure 5.15 depicts the measured mutual coupling be-

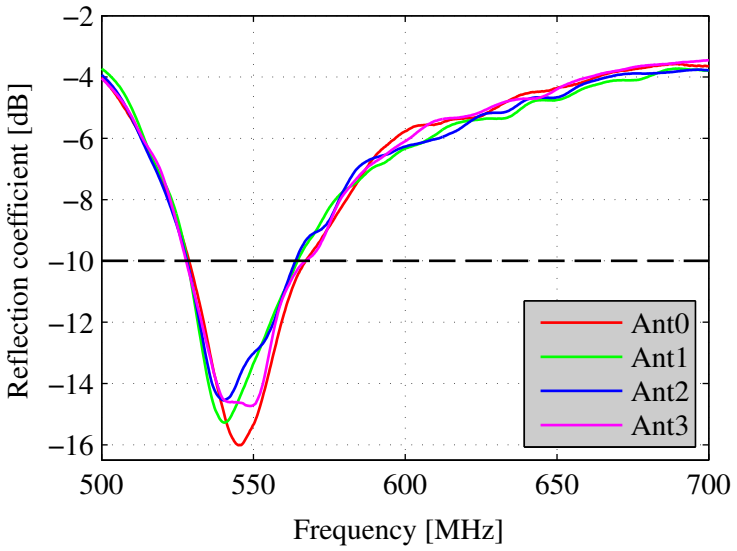

Figure 5.14: Active reflection coefficient of elements with $l = 250$mm

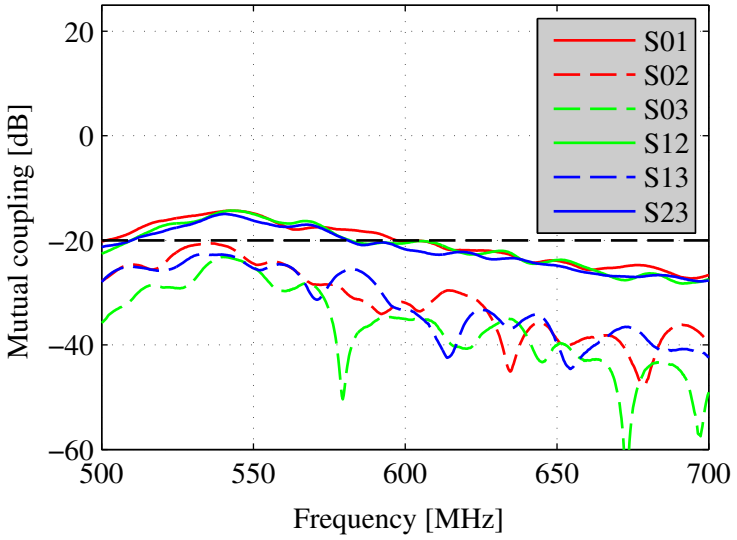

Figure 5.15: Coupling between elements with $l = 250$mm

tween the elements. Strong mutual coupling effects are observed for adjacent elements at the resonant frequency. This is undesirable as it will effect the steering capability of the array.

The individual antennas were shortened until the reflection coefficient of each antenna at 600MHz was below -10dB. Each individual antenna was trimmed by 20mm to $l = 230$mm to achieve this. Figures 5.16 and 5.17 depict the reflection coefficient of each element, and mutual coupling between elements of the array.

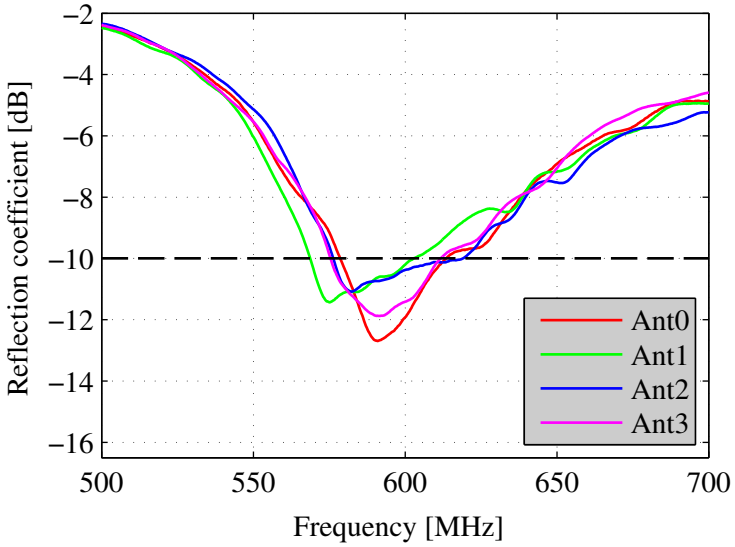

Figure 5.16: Active reflection coefficient of elements with $l = 230$mm

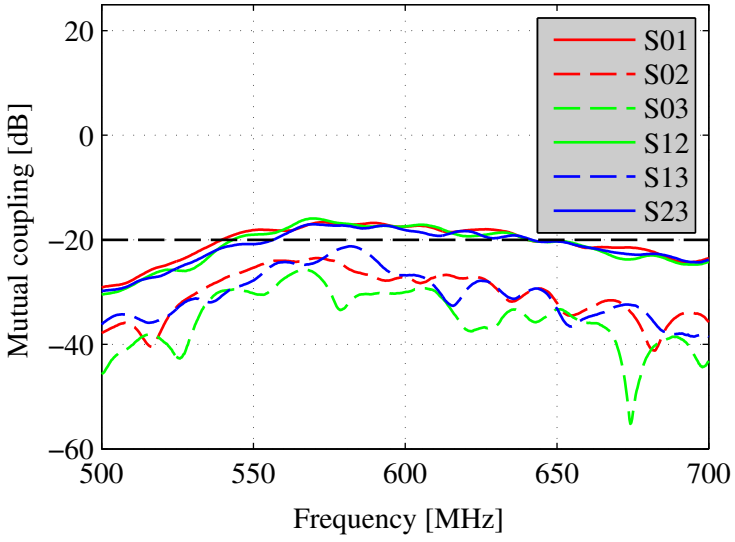

Figure 5.17: Coupling between elements with $l = 230$mm

Table 5.6: Gain measurement setup

TX Positioner A (VNA port: 1)	**RX** Positioner B (VNA port: 2)
Antenna array	LPDA 1
Antenna array	LPDA 2
LPDA 1	LPDA 2

From the discussion above it is noted that the theoretical, simulated and measured length to achieve resonance at 600MHz greatly vary. This is due to the theoretical models not accounting for the finite conductivity of the type of wire which was used to construct the antennas.

By comparing Figures 5.14 and 5.16, it can be seen that as the antenna lengths are shortened the active reflection coefficient increases. On average the active reflection coefficient increased by 3.8dB at the resonant frequencies.

Both Figures 5.15 and 5.17 depict strong mutual coupling between adjacent elements. However, mutual coupling between the adjacent elements in the array decrease by 3dB if the antenna lengths are trimmed. For both cases, the strongest coupling exist between the two inner elements.

Gain and Beam Pattern

For the gain and beam pattern measurements the antenna array was used as the transmit antenna (TX). The four antennas were fed from port 1 of the VNA by using a four-way power splitter. The array was positioned on the pedestal in the anechoic chamber. Additionally, two identical LPDAs were used as a receive antenna (RX) and TX antenna during the measurements.

A three antenna measurement was done to calculate the gain as follows: The transmit and receive combination of antennas for the gain measurement is summarized in Table 5.6. The gain is determined using the Friss Transmission formula, given by

$$\frac{P_{\mathrm{RX}}}{P_{\mathrm{TX}}} = \left(\frac{\lambda}{4\pi d_a}\right)^2 G_{\mathrm{TX}} G_{\mathrm{RX}} \,. \tag{5.5.1}$$

A ratio between the received power P_{RX} and transmitted power P_{TX} is measured by the VNA. The equation accounts for the distance d_a between the transmit and receive antennas. By conducting three measurements the gain of the transmit G_{TX} and receive G_{RX} antennas can be calculated.

Before measurements are made, a calibration procedure is executed. The calibration procedure is conducted using a high precision 8m RF cable, for which the loses need to be accounted during the gain calculation.

Figure 5.18 depicts the gain of the antenna array for both lengths over a frequency range of $500-635$MHz. The gain for antenna lengths $l = 250$mm and $l = 230$mm is 13.9dBi and 13.2dBi respectively, at the resonant frequencies.

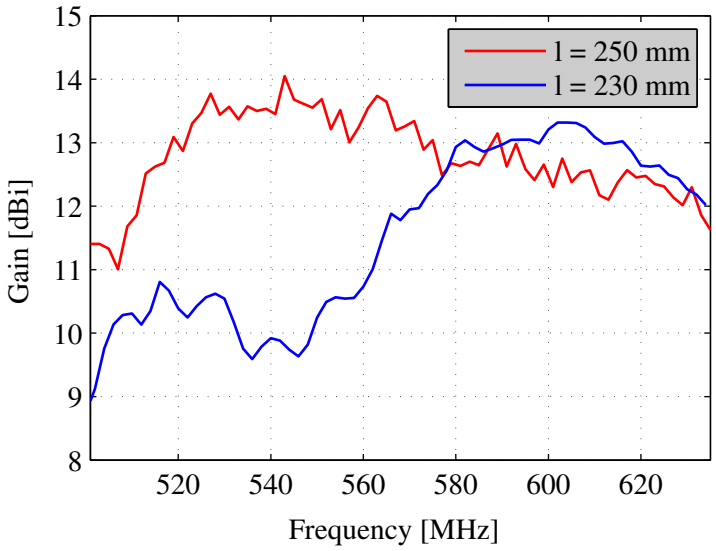

Figure 5.18: Measured gain of antenna array

Table 5.7: Measured beam pattern results

Parameter	l **=250** f_r **=545 MHz**	l **=230** f_r **=600 MHz**
HPBW	36.86°	36.42°
BW$_{NN}$	63°	66°
Relative SLL	−4.8dB	−7.5dB

The beam pattern of the antenna array was measured by rotating the antenna array through 180° on the pedestal. The power was measured in 3° intervals ranging between $-90° \leq \theta \leq 90°$.

Figure 5.19 shows the measured beam patterns of the antenna array for $l =$ 250mm and $l = 230$mm. The beam patterns were measured at the respective resonant frequencies of 545MHz and 600MHz for the two lengths. The main lobe of the antenna array with $l = 250$mm is squinted toward $-3°$, whereas the antenna array with $l = 230$mm has its maximum radiation at 0°. For both patterns the side lobes are asymmetric about the main lobe. The side lobes of the antenna array with $l = 250$mm exhibit greater asymmetry as well as a higher relative SLL. Table 5.7 lists the measured beam pattern results.

5.5.3 Digital Back-End Verification

The beam characteristics and steering capability of the design implemented on ROACH was verified for both a narrow and wide-band source. A four way 0° power divider with equal cable lengths were used to synthesize a source at broadside. To synthesize a source from another direction different cable

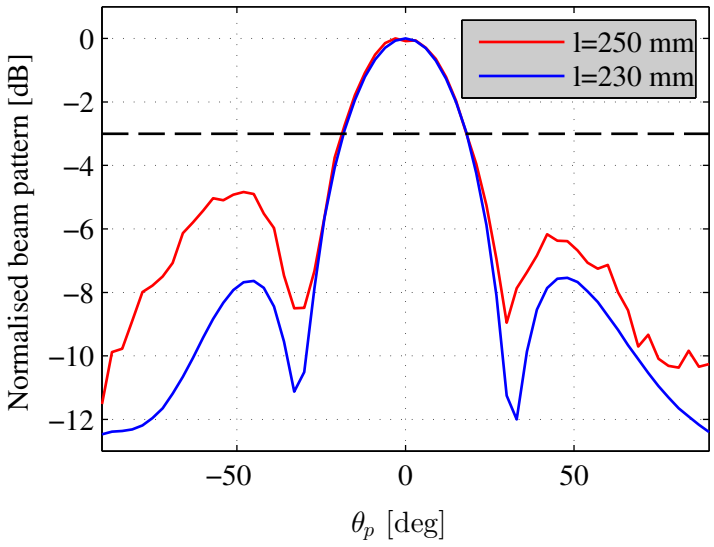

Figure 5.19: Measured beam pattern of antenna array

lengths were inserted into the signal paths to introduce delays.

Additionally, the gain and SFDR of the implemented design on ROACH were measured.

DBE Gain and SFDR

The gain and SFDR of the design depends on the operating frequency and has been experimentally measured for a frequency range of $0.25 - 1$GHz. The beamformer output was measured and logged at 25MHz intervals with an input power of -25dBm from the signal generator. The cable losses and power splitter output has also been measured and accounted for. Theoretically a four way power divider should provide a 6dB reduced power output at each port over the specified operating frequencies. Experiments have shown that although the loss at all the ports remain constant, the losses increased for higher frequencies. This was accounted for during the gain and SFDR calculations of the beamformer design.

The gain through the DBE can be determined as follows: The voltage into the ADC is first determined by,

$$v = \sqrt{2Z_{in}10^{-3}10^{\frac{P_{sg}-L+G_a}{10}}}\,, \tag{5.5.2}$$

where $Z_{in} = 50\Omega$, P_{sg} is the input power from the signal generator, L accounts for the cable and splitter losses, and G_a is the gain of the KATADC amplifier. Thereafter, the digitized voltage is calculated from

$$v_{adc} = 2v\left(2^{b_d-1}\right)\,, \tag{5.5.3}$$

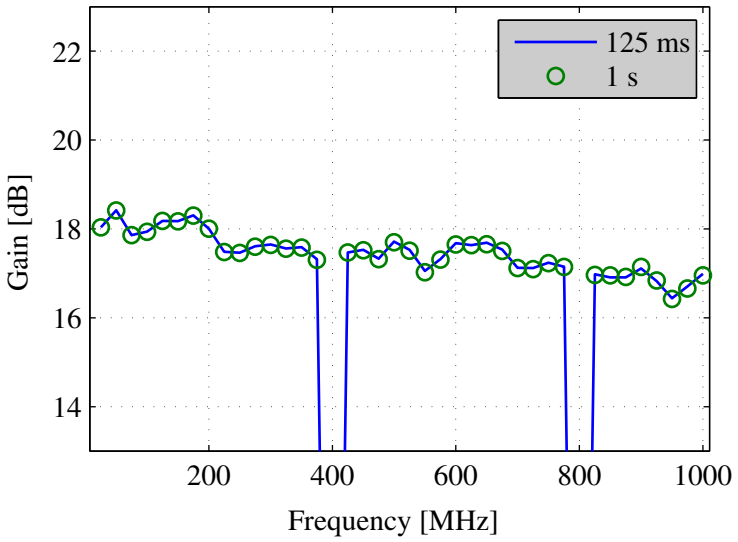

Figure 5.20: Measured DBE gain

where b_d is the number of bits with which the signal is digitized. The doubling factor is introduced to account for the conversion from a single-ended to a differential signal by the RF translator on the KATADC board. The gain of the beamformer G_b is then determined from the output of the beamformer which is the measured quantity given by,

$$Y = (4v_{adc}G_b)^2 N_{acc}\,, \tag{5.5.4}$$

where N_{acc} is the number of accumulations.

Figure 5.20 plots the calculated gain of the beamformer design. To verify the fidelity of the calculation, the experiment was repeated for two different accumulation lengths.

Figure 5.21 depicts the SFDR over the same frequency range for both accumulation lengths. This is obtained by calculating the difference in dB between the maximum and second maximum (worst spur) of the beamformer output. It can be seen from Figure 5.21 that the SFDR for an accumulation length of 1s is higher than that of an accumulation length of 0.125ms. This is expected since noise components and signal harmonics produced by the ADC are integrated out by using longer accumulation lengths.

It should be noted that both the gain and SFDR of the design reflect a cut-off for signals at 400MHz and 800MHz. This is because these frequencies are integer multiples of half the sampling rate $\frac{f_s}{2}$, where the sampling rate is 800MHz. Also note that only the gain calculation is normalized against the accumulation length.

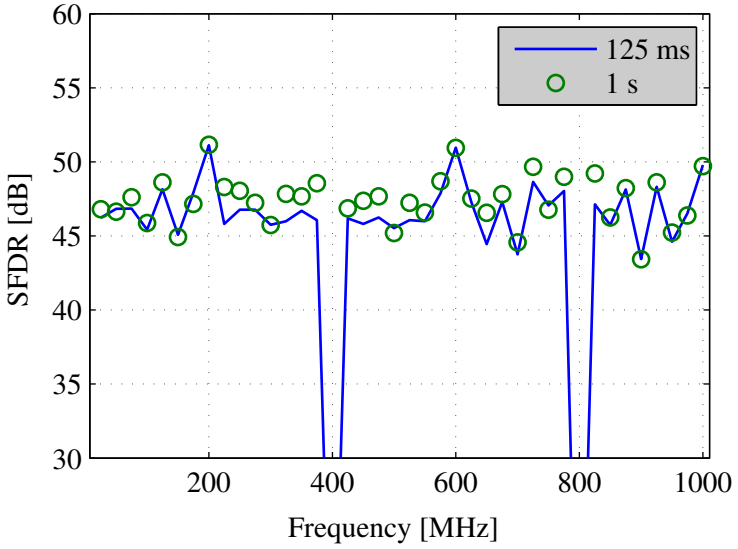

Figure 5.21: Measured DBE SFDR

Table 5.8: Beamformer output results

Parameter	Calculated	Measured
HPBW	25.77°	26.13°
BW$_{NN}$	60°	58.97°
Relative SLL	−11.35dB	−11.1dB

Beam Characteristics and Steering Capability

The narrow-band capability of the design was tested at 600MHz using a signal generator with an input power of −25dBm. Table 5.8 lists the calculated and measured relative SLL, HPBW and BW$_{NN}$ of the main lobe when the beam is steered to broadside.

As discussed in Chapter 2.3.3, grating lobes will appear in the visible region when an inter-element spacing equal to a wavelength is used. Additionally, by increasing the electrical length of the array the main lobe becomes narrower.

For the DBE, the inter-element spacing is specified in software and the beamformer output has been measured for three different spacings d. Figure 5.22 depicts the beamformer output for $d = \frac{\lambda}{4}$, $d = \frac{\lambda}{2}$, and $d = \lambda$. From Figure 5.22, it can be seen that the beamformer output corresponds to expected values.

Due to manufacturing simplicity of the cables, a source direction of $\theta_s = \pm 28.82°$ was synthesized by making use of different cable lengths. A coaxial cable with a PTFE dielectric was chosen to introduce the path length differences.

A list of the calculated phase and cable lengths are given in Table 5.9. Also

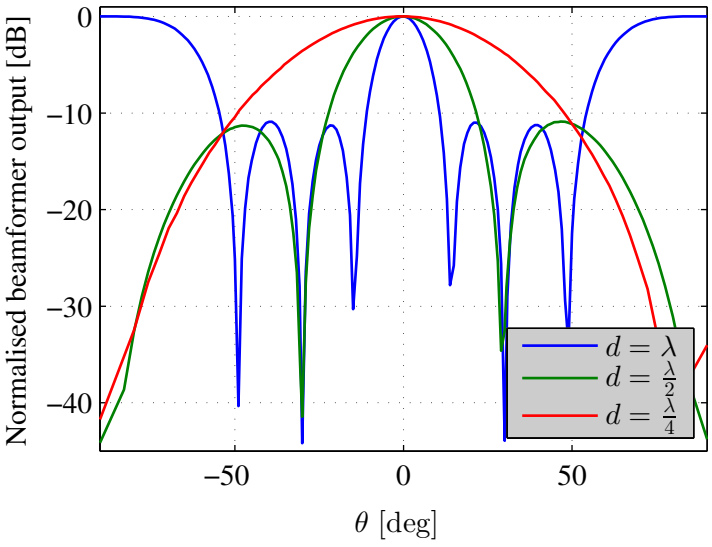

Figure 5.22: Beamformer output for different inter-element spacings

Table 5.9: Cable phase introduced with corresponding lengths

Parameter	Phase	Cable length
l_0	0°	0mm
l_1	86.66°	83mm
l_2	173.32°	166mm
l_3	259.98°	250mm

note that l_0 is introduced to illustrate a direct connection for the experimental setup depicted Figure 5.23. Nodes 0 - 3 indicated on the horizontal axes in Figure 5.23 correspond to the four inputs to the beamformer. The experiment was conducted with an input frequency of 600MHz with $\frac{\lambda}{2}$ spacing between the apparent antennas.

The experimental outcome is depicted in Figure 5.24. For the configuration shown on the left hand side of Figure 5.23, the beamformer output reaches a maximum at $\theta = -28.97°$ and for the configuration shown on the right, a maximum is reached at $\theta = 28.97°$. The small angular difference between the synthesized source and the beamformer output is due to the design only being able to steer in specific directions as discussed in Subsection 5.4.1.

The wide-band capability of the design was also verified. The experiment made use of a noise generator with a 300MHz bandwidth and equal cable lengths to all beamformer inputs, effectively synthesizing a wide-band source at broadside. Figure 5.25 shows the frequency profile of the noise source. The center frequency for the experiment was chosen at 200MHz with $\frac{\lambda}{2}$ spacing. It is therefore expected that the beam becomes narrower for higher frequencies

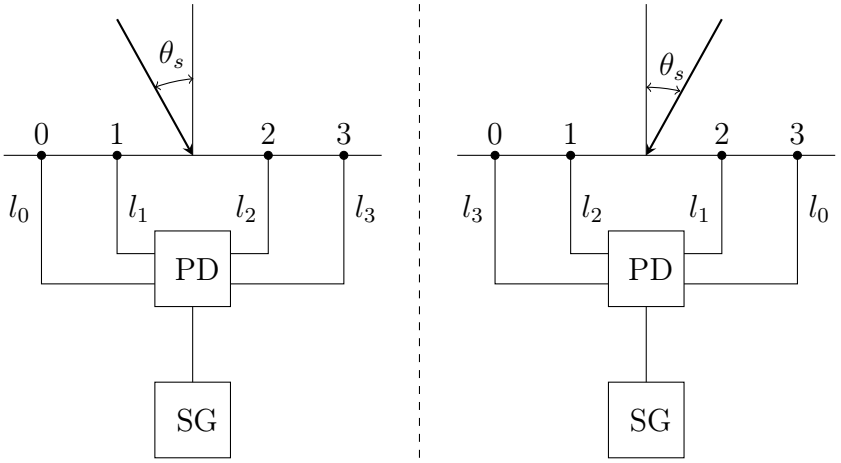

Figure 5.23: Experimental setup using a signal generator (SG) and power divider (PD) for design verification (Left: $\theta_s = -28.82°$ Right :$\theta_s = 28.82°$)

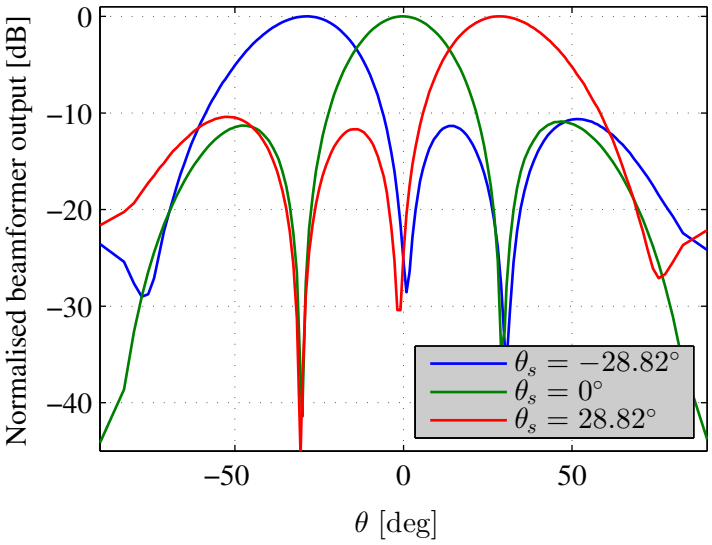

Figure 5.24: Beamformer output for different source directions

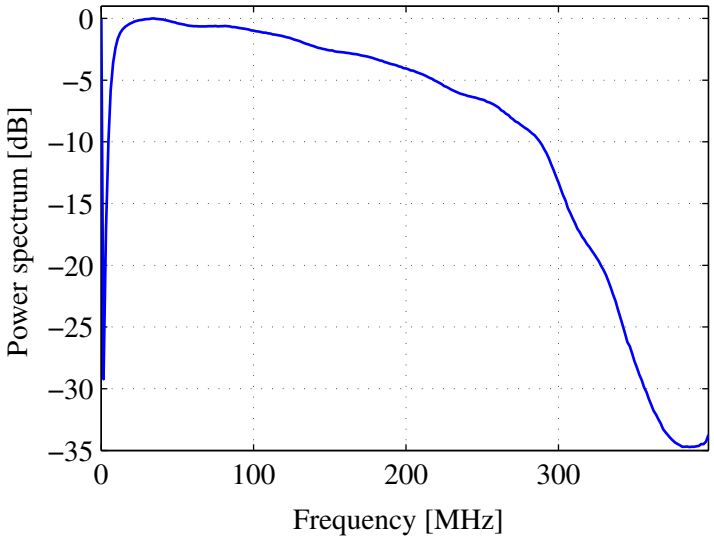

Figure 5.25: Wide-band frequency profile of noise source

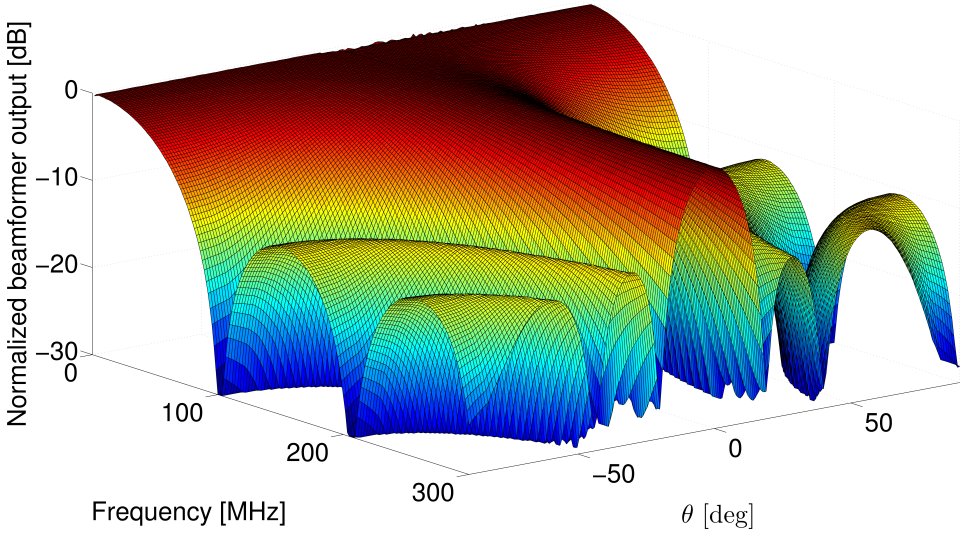

Figure 5.26: Wide-band beamformer output

and wider for lower frequencies. It is also expected that the beamformer reach a maximum at $\theta = 0°$ across the entire frequency range. Figure 5.26 illustrates the results of the wide-band experiment, which corresponds to the expected output.

5.5.4 Antenna Array and DBE

As discussed in Chapter 3.2, a beamformer can steer the main beam of an antenna array in various directions. In order to verify the beamformer de-

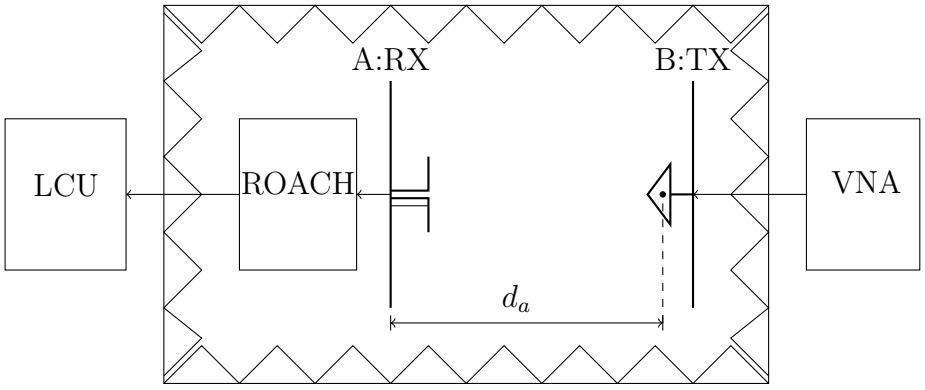

Figure 5.27: A side view of the experimental setup in the anechoic chamber

sign it must therefore be shown that the design can apply the phase rotation necessary to steer the array beam in different directions. Two experiments were conducted in the anechoic chamber, each with the aim of electronically pointing the beam of the array in specified directions.

During both experiments the antenna array was positioned on the pedestal at positioner A in the anechoic chamber and used as the receiver. Additionally, an LPDA was placed at positioner B and used as a transmitting source. Port 1 of the VNA was connected to the LPDA, with the VNA output set to generate a 0dBm, 600MHz CW source.

A side view of the experimental setup is depicted in Figure 5.27. In Subsection 5.5.1 it was mentioned that the perpendicular separation of the antennas is 5.289m. The distance between the phase centers of the receiver and transmitter however, is $d_a = 5.218$m, as indicated in Figure 5.27.

Results and Analysis: Experiment One

During the first experiment the antenna array remained fixed on the pedestal with antenna 0 positioned to the right and antenna 3 positioned to the left of positioner A, from a view as depicted in Figure 5.13. The LPDA at positioner B was moved horizontally between $-1.51\text{m} \leq x \leq 1.51\text{m}$ to synthesize source directions $-16.13^\circ \leq \theta_s \leq 16.13^\circ$. The source direction is calculated using,

$$\theta_s = \tan^{-1}\left(\frac{x}{d_a}\right) . \tag{5.5.5}$$

Figure 5.28 depict the beamformer output for a source direction $\theta_s = -14.29^\circ$, $\theta_s = 0^\circ$, and $\theta_s = 14.29^\circ$. For these source directions, the beamformer steered the main beam of the antenna array to $\theta = -14.94^\circ$, $\theta = 0^\circ$, and $\theta = 14.94^\circ$ respectively.

Various reasons account for the error observed. Mutual coupling between the antenna elements in the array causes a deviation in the direction of the

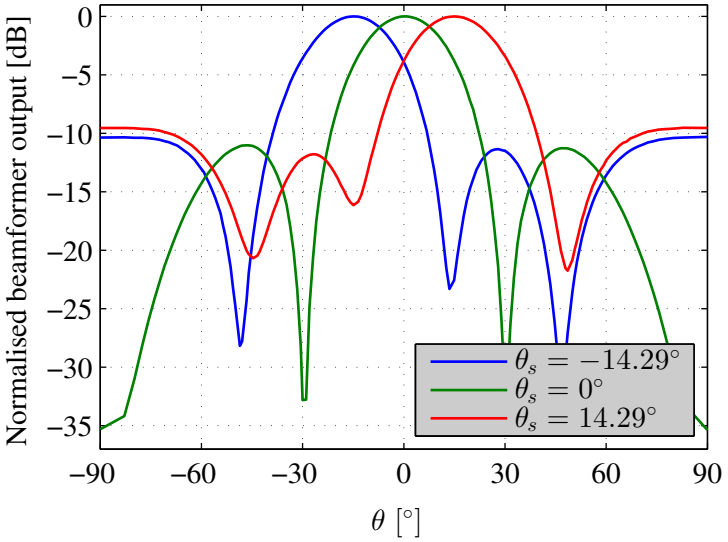

Figure 5.28: Beamformer output for three source directions

main lobe. Moreover, mutual coupling and the effects thereof increase for larger scan angles as discussed in Chapter 2.3.3. Reflections in the room also contribute towards the error.

The maximum possible error for each source position has been determined. It is expected that the error would increase as the source is moved to either side of the anechoic chamber. This is due to more reflections occurring as the source is positioned closer to the anechoic chamber wall, as well as the effect of mutual coupling increasing for larger scan angles. It is also expected that an error would arise quicker for a source synthesized with a positive x direction. This is due to the asymmetric configuration of the transmit and receive antennas to ensure proper alignment.

Figure 5.29 illustrates a summary of the results obtained for this experiment. The maximum possible error for each source position is plotted with error bars along the expected output. The error bar takes into account mutual coupling effects as obtained by FEKO for the different scan angles. It also takes into account a 1° error for reflected radiation, with the source positioned at $x = 0$m. The error to account for reflections increase linearly to 2° and 1.9° for a source position at $x = 1.51$m and $x = -1.51$m respectively.

Results and Analysis: Experiment Two

During the second experiment the LPDA remained stationary and the antenna array was rotated on the pedestal. The beamformer directs the main beam of the array in steps of 5° ranging between $-45° \leq \theta \leq 45°$.

For each specific θ direction, the antenna array was rotated on the pedestal through 180° ranging between $-90° \leq \theta_p \leq 90°$.

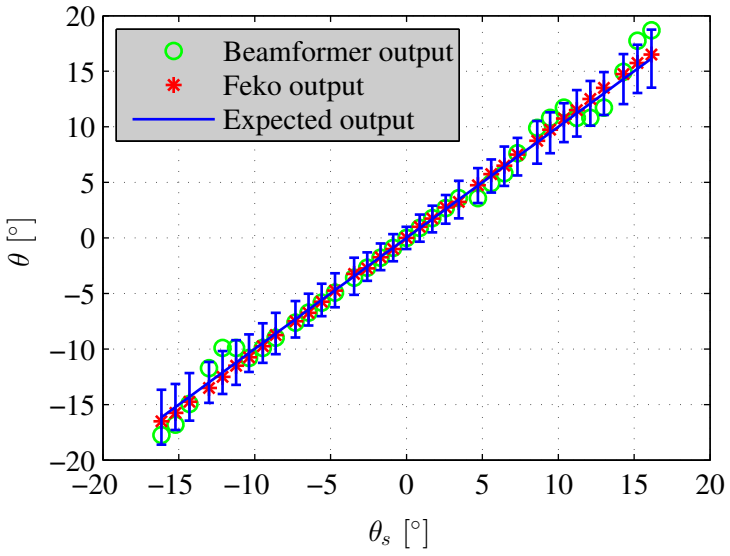

Figure 5.29: Experiment one results

At each pedestal direction θ_p for a specific beamformer pointing direction θ, the output of the beamformer was measured and logged. For a beamformer pointing direction of $\theta = -5°$, it is therefore expected that the maximum beamformer output should be obtained when the pedestal is positioned at $\theta_p = 5°$.

The results obtained for $\theta = -14.94°$, $\theta = 0°$, and $\theta = 14.94°$ is shown in Figure 5.30. For these pointing directions, the beamformer reached a maximum with the pedestal orientated at $\theta_p = 15°$, $\theta_p = 0°$, and $\theta_p = -15°$.

Figure 5.31 summarizes the results of the experiment. The figure depicts the position θ_p for a maximum beamformer output whilst the beamformer is pointing in a specific θ direction. Errors are also expected during the experiment due mutual coupling effects and the rotational error introduced by the pedestal.

An error bar has been placed along the expected outcome in Figure 5.31. The error for each θ direction was determined by taking into account the mutual coupling effects as was done in experiment one above. Further, the error bar also includes a constant 1° error for reflections due to a source position at $x = 0$. Additionally, the error bar takes into account an angular error of 0.76° to account for the rotational instability of the pedestal.

5.6 Conclusion

During the execution of the project, a four element antenna array was designed and constructed. The antenna array resonates at 600MHz with sufficient performance metrics to act as supporting instrumentation to verify the

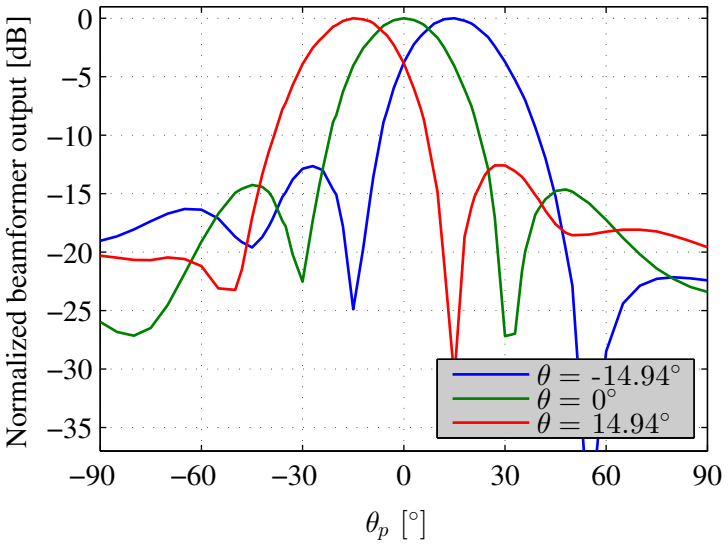

Figure 5.30: Beamformer output for three beamformer pointing directions

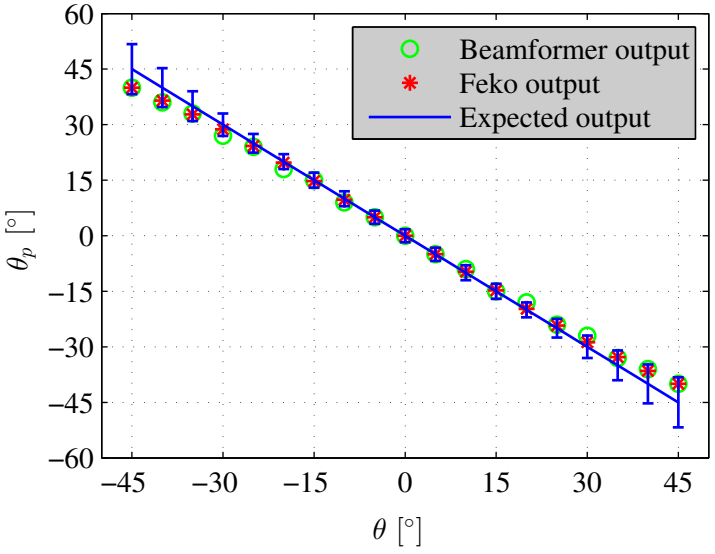

Figure 5.31: Experiment two results

beamformer capabilities.

A four element beamformer has been designed and implemented on the ROACH processing platform. The design successfully rotates the phase and sums four incoming data streams. It has been tested for three different synthesized source directions. Further, the beamformer operation for a narrow-band as well as a wide-band source has been tested and verified.

Numerous challenges, discussed throughout the previous Section, were faced in order to design acceptable experiments for the verification of the antenna array in combination with the DBE. However, the beam steering capability of the DBE could be demonstrated and verified. Measured results depicted small variations from the expected outcome due to the various factors discussed.

Furthermore, it is observed that experiment one deviates from the expected outcome quicker than experiment two. This is due to the stationary position of the transmit antenna at positioner B during the second experiment. Therefore less reflections occurred from the anechoic chamber walls during this experiment, resulting in more accurate measurements.

Chapter 6

Conclusion

6.1 Summary

During the execution of the project, both the theoretical and implementation aspects of beamforming were addressed. The theory required to investigate these aspects were developed in Chapter 2. Furthermore, the motives for limiting the scope of the thesis to investigating digital frequency domain beamformers, implemented on FPGA based architectures, were highlighted.

In Chapter 3 an investigation was conducted with respect to deterministic beamforming algorithms. Various beamformers were implemented in a MATLAB program, specifically the steering vector, spectral weightings, Dolph-Chebychev, and the LSE algorithm were investigated. This was then followed by a discussion on the various Radio Astronomy applications of the algorithms.

The focus of the thesis then shifted to beamformer implementations. First, an emulation of a linear array was implemented in PYTHON, using the UniBoard to process digitally synthesized data. During the experiment the UniBoard was configured with beamformer firmware and a total of 181 beams were produced simultaneously, to determine the response of the emulated array. The experiment was the first of its kind to be conducted using the UniBoard beamformer firmware which will be used for the APERTIF project.

Second, a digital frequency domain beamformer was designed and implemented on the ROACH processing board. This was the primary focus of Chapter 5, however the design and verification of a four element array were also discussed. The antenna array was used to verify the steering capability of the DBE. Measurements took place in an anechoic chamber and produced reasonable results. The errors were expected as the operating frequency of the instrument was much less than the lower cut-off frequency of the facility.

6.2 User Perspective on ROACH and UniBoard

The ROACH and UniBoard are at the forefront of current technology available in the Radio Astronomy community. It has been suggested by [55] that the DSP needs for the SKA aperture arrays will be achieved by successors of either the ROACH or UniBoard. Therefore, these architectures were the primary focus of the real-time processing aspect to beamforming.

From a user perspective there are many similarities and differences between the ROACH and UniBoard. Both hardware platforms are FPGA based architectures. The core of a ROACH board is an Xilinx FPGA, whereas UniBoards are fitted with Altera FPGAs. Memory mapped software registers on the UniBoard are accessed via the NIOSII embedded processor, whereas ROACH is fitted with an external PowerPC for communicating with the FPGA.

Furthermore, the processing boards have custom made servers which may optionally be used for interfacing with a design via a TCP connection. Compatible PYTHON wrappers exist for both servers, which greatly simplifies the communication procedure. The ROACH board runs the KATCP daemon which listens for connections, whereas the UniServer program is executed on an external LCU and is used for communicating with the beamformer firmware on UniBoard.

Both processing boards were designed to be scalable, such that the processing capacity can easily be increased by interconnecting multiple boards. UniBoards are interconnected via backplanes or standardized 10GbE links. Standardized 10GbE links are also used to interconnect multiple ROACH boards.

The number of sub-bands to be processed, beams to be produced, and weighting functions to be applied are easily reconfigurable using the UniBoard beamformer firmware. However, to change functionalities such as the frequency resolution requires additional VHDL code. The CASPER software and gateware libraries allows users to reconfigure the complete FPGA design using high-level tools such as the MATLAB/SIMULINK environment. This makes the CASPER toolflow accessible to a broader audience.

From the discussions above, it is evident that both processing boards are flexible and scalable. These attributes along with their parallel processing capability makes them excellent platforms to meet the challenging processing requirements set by the SKA.

6.3 Contributions

Given the work discussed in Chapters 2, 3, 4, and 5 it is established that the thesis investigates Radio Astronomy beamforming techniques in its entirety. The following list of contributions were made during the execution of the project:

1. The minimum bandpass sampling rate was determined for both integer and non-integer positioned spectra.
2. A comparison between GPU and FPGA technology with respect to the signal processing requirements in Radio Astronomy.
3. The channelized response of a signal was investigated using both a FFT and PFB implementation.
4. It was established that symmetry in the FFT and PFB output can be exploited to half the processing cost.
5. The effect of the array configuration on the resulting beam pattern was determined and investigated.
6. The various steering effects on the beam pattern was established.
7. The steering algorithm was implemented to steer the beam of an simulated array.
8. Uniform, sinusoidal, DPSS, and Kaiser spectral weighting functions were implemented and their effect on the beam pattern was established.
9. A Dolph-Chebychev weighting vector was determined and implemented.
10. The LSE algorithm was used to implement null steering.
11. Uses of the implemented algorithms within Radio Astronomy community were established.
12. The UniBoard architecture was investigated.
13. A PYTHON script was implemented to emulate a linear array using the UniBoard to process the data. This was the first experiment to be conducted using signals with a phase variation in conjunction with the UniBoard beamformer firmware which will be used for the APERTIF project.
14. The ROACH architecture was investigated.
15. A four element coherent frequency domain beamformer was implemented on the ROACH processing board.
16. An antenna array was designed to verify the beamformer design.
17. Experiments were invented to verify the steering capability of the beamformer using the antenna array.
18. Measurements were conducted in an anechoic chamber and the results showed small deviations from the expected values.
19. The causes of the deviations were investigated, and acceptable error ranges were established.

6.4 Recommendations for Future Work

Optimum and Adaptive Beamformer Simulator

A program that simulates beamforming techniques to optimize array performance metrics such as the SNR and noise variance. This can be achieved by implementing optimum and adaptive beamforming algorithms. The simulator must have the capability to generate noise and signal models which will be required to implement adaptive algorithms.

The program should simulate the response to an arbitrary array configuration. Additionally to obtain the total array response, the program must account for the beam pattern of an individual element in the array.

Adaptive Array Emulator

In Chapter 4, an uniform linear array emulation using the UniBoard to process data, was discussed. This emulator can be extended to incorporate the weighting functions discussed in Chapter 3 as well as optimum and adaptive algorithms.

The emulator must process a wide-band signal model as well as a narrow-band signal model. Furthermore, the emulator should be robust and compatible with both digitally synthesized and actual data.

Software Defined Radio Instrument

A complete Software Defined Radio (SDR) instrument may be designed, incorporating the existing DBE.

However, the DBE may be optimized to use less resources, such that a cross correlator may be fitted onto the fabric. This may then be used to implement a more efficient calibration strategy. It will also provide the possibility of implementing adaptive beamforming techniques.

It will be required to design an AFE consisting of a LNA and bandpass filter with a steep roll-off. The sensitivity of the instrument will suffice to observe true celestial sources. Additional control scripts may be implemented to increase functionality, for example a tracking function.

Appendices

Appendix A

Mathematical Definitions

A.1 Modified Bessel Function of the First Kind

The modified Bessel function of the first kind is given by,

$$I_m(x) = \left(\frac{x}{2}\right)^m \sum_{p=0}^{\infty} \frac{\left(\frac{x^2}{4}\right)^p}{p!\,(p+m)!} \tag{A.1.1}$$

A.2 Binomial Series Expansion

The beam pattern,

$$B(u) = \begin{cases} \sum_{i=1}^{\frac{N}{2}} \alpha_i \cos\left[\left(\frac{\pi(2i-1)d}{\lambda}\right)u\right], & N \text{ even} \\ \sum_{i=0}^{\frac{N-1}{2}} \alpha_i \cos\left(\frac{2i\pi d}{\lambda}u\right), & N \text{ odd} \end{cases} \tag{A.2.1}$$

is repeated here for clarity. In order to write the beam pattern in terms of a polynomial the $\cos\left(m\frac{\pi d}{\lambda}u\right)$ terms must be written in terms of a polynomial $\cos^m\left(\frac{\pi d}{\lambda}u\right)$. The real part of the binomial series expansion is given as,

$$\begin{aligned} \cos\left(m\frac{\pi d}{\lambda}u\right) &= \cos^m\left(\frac{\pi d}{\lambda}u\right) \\ &\quad - \frac{m(m-1)}{2!}\cos^{m-2}\left(\frac{\pi d}{\lambda}u\right)\sin^2\left(\frac{\pi d}{\lambda}u\right) \\ &\quad + \frac{m(m-1)(m-2)(m-3)}{4!}\cos^{m-4}\left(\frac{\pi d}{\lambda}u\right)\sin^4\left(\frac{\pi d}{\lambda}u\right) - \cdots, \end{aligned} \tag{A.2.2}$$

where

$$\sin^2\left(\frac{\pi d}{\lambda}u\right) = 1 - \cos^2\left(\frac{\pi d}{\lambda}u\right). \tag{A.2.3}$$

Therefore, if x is defined as given in Chapter 3,

$$x = \cos\left(\frac{\pi d}{\lambda}u\right), \tag{A.2.4}$$

repeated here for clarity, then by using Equation A.2.2 becomes,

$$\begin{aligned} \text{for } m = 0 \quad &, \cos\left(m\frac{\pi d}{\lambda}u\right) = 1 \\ \text{for } m = 1 \quad &, \cos\left(m\frac{\pi d}{\lambda}u\right) = x \\ \text{for } m = 2 \quad &, \cos\left(m\frac{\pi d}{\lambda}u\right) = 2x^2 - 1\,, \end{aligned} \tag{A.2.5}$$

which are the Chebychev polynomials.

A.3 Complex Gradient

The complex gradient, of a vector $\mathbf{w}$ is defined as,

$$\nabla_{\mathbf{w}} = \left[\frac{\partial}{\partial w_0} \quad \frac{\partial}{\partial w_1} \quad \cdots \quad \frac{\partial}{\partial w_{N-1}}\right]^T \tag{A.3.1}$$

where $\frac{\partial}{\partial w_n}$ is given by,

$$\frac{\partial}{\partial w_n} = \frac{\partial}{\partial \Re w_n} - j\frac{\partial}{\partial \Im w_n}, \quad n = 0, 1, \cdots, N-1\,. \tag{A.3.2}$$

Similarly, the complex gradient, with respect to hermitian transpose of a vector $\mathbf{w}$, is defined as

$$\nabla_{\mathbf{w^H}} = \left[\frac{\partial}{\partial w_0^*} \quad \frac{\partial}{\partial w_1^*} \quad \cdots \quad \frac{\partial}{\partial w_{N-1}^*}\right] \tag{A.3.3}$$

where $\frac{\partial}{\partial w_n^*}$ is given by,

$$\frac{\partial}{\partial w_n^*} = \frac{\partial}{\partial \Re w_n} + j\frac{\partial}{\partial \Im w_n}, \quad n = 0, 1, \cdots, N-1\,. \tag{A.3.4}$$

Appendix B

Electromagnetic Theory

B.1 Image Theory

Radiation from an antenna element is reflected at an interface. The behavior of the reflected waves depends on the orientation and polarity of the source, as well as the constitutive parameters of the media. For the purposes of the thesis only electric sources above an infinite PEC interface will be considered. Image theory states that a source above a conducting plane can be replaced by an equivalent system. The equivalent system consists of the actual source and an image source to account for the reflected the waves. The polarity of the image source is determined by the boundary conditions. The boundary condition for a PEC states that the tangential components of an electric field along a PEC is zero. Also the normal components of the electric flux density is discontinuous by the amount of surface charge density on the boundary. If there is no surface charge density on the boundary then this boundary condition ensures the continuity of the normal components of the electric flux density and therefore the electric field[56].

The image of a vertical dipole above a PEC, as indicated in Figure B.1, has the same polarity as the actual source. For a horizontal dipole above a PEC the image must have opposite polarity to adhere to the boundary conditions. The total radiation from an observation point is the superposition of the radiation from the actual and image source. Refer to [28] for more information about image theory and radiating antennas above planes.

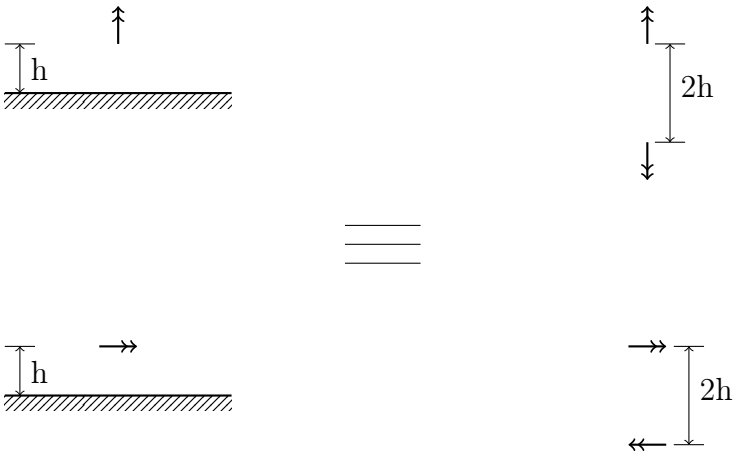

Figure B.1: Electric sources above a PEC and their equivalent systems

List of References

[1] K. G. Jansky, "Electrical Disturbances Apparently of Extraterrestrial Origin," *Proceedings of the IRE*, vol. 21, no. 10, pp. 1387–1398, 1933.

[2] S. Ransom and J. Condon, "Essential Radio Astronomy," 2010. [Online]. Available: http://www.cv.nrao.edu/course/astr534/ERA.shtml

[3] J. Liu, J. Ma, J. Tian, Z. Kang, and P. White, "Pulsar navigation for interplanetary missions using CV model and ASUKF," *Aerospace Science and Technology*, vol. 22, no. 1, pp. 19–23, Oct. 2012.

[4] "Atacama Large Millimeter/submillimeter Array (ALMA)." [Online]. Available: http://www.almaobservatory.org/

[5] M. de Vos, A. Gunst, and R. Nijboer, "The LOFAR Telescope: System Architecture and Signal Processing," *Proceedings of the IEEE*, vol. 97, no. 8, pp. 1431–1437, Aug. 2009. [Online]. Available: http://dx.doi.org/10.1109/JPROC.2009.2020509

[6] W. a. Imbriale, "The Square Kilometre Array: Engineering opportunities," in *2010 IEEE International Conference on Wireless Information Technology and Systems*. IEEE, Aug. 2010, pp. 1–1. [Online]. Available: http://dx.doi.org/10.1109/ICWITS.2010.5611857

[7] J. Jonas, "MeerKAT: The South African Array With Composite Dishes and Wide-Band Single Pixel Feeds," *Proceedings of the IEEE*, vol. 97, no. 8, pp. 1522–1530, Aug. 2009. [Online]. Available: http://dx.doi.org/10.1109/JPROC.2009.2020713

[8] "SKA Telescope webpage," 2014. [Online]. Available: https://www.skatelescope.org

[9] D. R. DeBoer, R. G. Gough, J. D. Bunton, T. J. Cornwell, R. J. Beresford, S. Johnston, I. J. Feain, A. E. Schinckel, C. A. Jackson, M. J. Kesteven, A. Chippendale, G. A. Hampson, J. D. O'Sullivan, S. G. Hay, C. E. Jacka, T. W. Sweetnam, M. C. Storey, L. Ball, and B. J. Boyle, "Australian SKA Pathfinder: A High-Dynamic Range Wide-Field of View Survey Telescope," *Proceedings of the*

IEEE, vol. 97, no. 8, pp. 1507–1521, Aug. 2009. [Online]. Available: http://dx.doi.org/10.1109/JPROC.2009.2016516

[10] A. et al Faulkner, "Aperture Arrays for the SKA: The SKADS White Paper,SKA Memo 122," no. March, pp. 1–146, 2010.

[11] C. Lonsdale, R. Cappallo, M. Morales, F. Briggs, L. Benkevitch, J. Bowman, J. Bunton, S. Burns, B. Corey, L. DeSouza, S. Doeleman, M. Derome, A. Deshpande, M. Gopala, L. Greenhill, D. Herne, J. Hewitt, P. Kamini, J. Kasper, B. Kincaid, J. Kocz, E. Kowald, E. Kratzenberg, D. Kumar, M. Lynch, S. Madhavi, M. Matejek, D. Mitchell, E. Morgan, D. Oberoi, S. Ord, J. Pathikulangara, T. Prabu, A. Rogers, A. Roshi, J. Salah, R. Sault, N. Shankar, K. Srivani, J. Stevens, S. Tingay, A. Vaccarella, M. Waterson, R. Wayth, R. Webster, A. Whitney, A. Williams, and C. Williams, "The Murchison Widefield Array: Design Overview," *Proceedings of the IEEE*, vol. 97, no. 8, pp. 1497–1506, Aug. 2009. [Online]. Available: http://dx.doi.org/10.1109/JPROC.2009.2017564

[12] G. W. Kant, P. D. Patel, S. J. Wijnholds, M. Ruiter, and E. van der Wal, "EMBRACE: A Multi-Beam 20,000-Element Radio Astronomical Phased Array Antenna Demonstrator," *IEEE Transactions on Antennas and Propagation*, vol. 59, no. 6, pp. 1990–2003, Jun. 2011. [Online]. Available: http://dx.doi.org/10.1109/TAP.2011.2122233

[13] B. D. Jeffs, K. F. Warnick, J. Landon, J. Waldron, D. Jones, J. R. Fisher, and R. D. Norrod, "Signal Processing for Phased Array Feeds in Radio Astronomical Telescopes," *IEEE Journal of Selected Topics in Signal Processing*, vol. 2, no. 5, pp. 635–646, Oct. 2008. [Online]. Available: http://ieeexplore.ieee.org/lpdocs/epic03/wrapper.htm?arnumber=4705793

[14] M. V. Ivashina, O. Iupikov, R. Maaskant, W. a. van Cappellen, and T. Oosterloo, "An Optimal Beamforming Strategy for Wide-Field Surveys With Phased-Array-Fed Reflector Antennas," *IEEE Transactions on Antennas and Propagation*, vol. 59, no. 6, pp. 1864–1875, Jun. 2011. [Online]. Available: http://dx.doi.org/10.1109/TAP.2011.2123865

[15] K. Zarb-Adami, A. Faulkner, J. G. Bij de Vaate, G. W. Kant, and P. Picard, "Beamforming techniques for large-N aperture arrays," in *2010 IEEE International Symposium on Phased Array Systems and Technology*. IEEE, Oct. 2010, pp. 883–890. [Online]. Available: http://dx.doi.org/10.1109/ARRAY.2010.5613258

[16] A. Sclocco, A. L. Varbanescu, J. D. Mol, and R. V. van Nieuwpoort, "Radio Astronomy Beam Forming on Many-Core Architectures," in *2012 IEEE 26th International Parallel and Distributed Processing*

Symposium. IEEE, May 2012, pp. 1105–1116. [Online]. Available: http://dx.doi.org/10.1109/IPDPS.2012.102

[17] V. Nagpal and T. Filiba, "Beamforming for Antenna Arrays BEE2 vs DSP Processors," pp. 1–9, 2007. [Online]. Available: https://casper.berkeley.edu/wiki/Papers

[18] F. Kapp, "The MeerKAT Digital Back End," in *High-performance Signal and Data Processing Workshop*, 2014. [Online]. Available: http://indico.tlabs.ac.za/getFile.py/access?contribId=31&sessionId=1&resId=0&materialId=slides&confId=48

[19] D. Werthimer, "Petaflop Radio Astronomy Signal Processing and the CASPER Collaboration," in *CASPER Workshop*, 2014. [Online]. Available: http://insidehpc.com/2014/05/petaflop-radio-astronomy-signal-processing-casper-collaboration/

[20] J. D. Mol and J. W. Romein, *Euro-Par 2011 Parallel Processing*, ser. Lecture Notes in Computer Science, E. Jeannot, R. Namyst, and J. Roman, Eds. Berlin, Heidelberg: Springer Berlin Heidelberg, 2011, vol. 6853, no. PART 2.

[21] R. Vaughan, N. Scott, and D. White, "The theory of bandpass sampling," *IEEE Transactions on Signal Processing*, vol. 39, no. 9, pp. 1973–1984, 1991. [Online]. Available: http://dx.doi.org/10.1109/78.134430

[22] D. Akos, M. Stockmaster, J. Tsui, and J. Caschera, "Direct bandpass sampling of multiple distinct RF signals," *IEEE Transactions on Communications*, vol. 47, no. 7, pp. 983–988, Jul. 1999. [Online]. Available: http://dx.doi.org/10.1109/26.774848

[23] F. Kapp, "Welcome to CASPER," in *CASPER Workshop*, 2014. [Online]. Available: https://casper.berkeley.edu/2014_presentations/Monday/kapp_casper2014.pdf

[24] J. Manley, "Meeting MeerKATs signal processing challenges," in *High-performance Signal and Data Processing Workshop*, 2014. [Online]. Available: http://indico.tlabs.ac.za/getFile.py/access?contribId=91&sessionId=6&resId=0&materialId=slides&confId=48

[25] J. Chennamangalam, "The Polyphase Filter Bank Technique," pp. 1–6, 2014. [Online]. Available: https://casper.berkeley.edu/wiki/The_Polyphase_Filter_Bank_Technique

[26] H. L. V. Trees, *Optimum Array Processing*. John Wiley & Sons, 2002.

[27] D. M. Pozar, *Microwave Engineering*, 4th ed. John Wiley & Sons, 2012.

[28] C. A. Balanis, *Antenna theory Analysis and design*, 3rd ed. John Wiley & Sons, 2005.

[29] D. M. Pozar, *Microwave and RF Design of Wireless Systems*. John Wiley & Sons, 2001.

[30] D. Davidson, "Private discussion," 2014.

[31] R. Armstrong, J. Hickish, K. Adami, and M. Jones, "A digital broadband beamforming architecture for 2-PAD," in *SKADS Conference 2009*, A. F. SA Torchinsky, A van Ardenne, T van den Brink, AJJ van Es, Ed., no. November, Chateau de Limelette, Belgium, Dec. 2009, pp. 273–278.

[32] A. R. Thompson, J. M. Moran, and G. Swenson, *Interferometry and Synthesis in Radio Astronomy*, 2nd ed. Wiley-VCH, 2004.

[33] S. J. Wijnholds and R. Jongerius, "Computing cost of sensitivity and survey speed for aperture array and phased array feed systems," in *2013 Africon*. IEEE, Sep. 2013, pp. 1–4. [Online]. Available: http://dx.doi.org/10.1109/AFRCON.2013.6757826

[34] P. Benthem and G. W. Kant, "EMBRACE: Results from an aperture array for radio astronomy," in *2012 6th European Conference on Antennas and Propagation (EUCAP)*. IEEE, Mar. 2012, pp. 629–633. [Online]. Available: http://dx.doi.org/10.1109/EuCAP.2012.6206634

[35] N. R. G. A Brown, P Alexander, A El-Makadema, E de Lera Acedo, "Analysis of Phased Aperture Array Geometries for Low Frequency Radio Astronomy," in *SKADS Conference 2009*, A. F. e. S.A. Torchinsky, A. van Ardenne, T. van den Brink-Havinga, A.J.J. van Es, Ed., no. November, Chateau de Limelette, Belgium, 2009, pp. 149–152.

[36] O. A. Iupikov, M. V. Ivashina, and O. M. Smirnov, "Reducing the complexity of the beam calibration models of phased-array radio telescopes," in *Antennas and Propagation (EUCAP), Proceedings of the 5th European Conference*. IEEE, 2011, pp. 930–933.

[37] A. Gunst, A. Szomoru, G. Schoonderbeek, E. Kooistra, D. V. D. Schuur, and H.-J. Pepping, "The application of UniBoard as a beam former for APERTIF," *Experimental Astronomy*, vol. 37, no. 1, pp. 55–67, Dec. 2013. [Online]. Available: http://dx.doi.org/10.1007/s10686-013-9366-x

[38] "UniBoard," 2011. [Online]. Available: http://www.radionet-eu.org/fp7/uniboard.html

[39] T. Oosterloo, M. Verheijen, W. V. Cappellen, L. Bakker, G. Heald, and M. Ivashina, "Apertif - the focal-plane array system for the WSRT," in *SKADS Conference 2009*, A. F. SA Torchinsky, A van Ardenne, T van den

Brink, AJJ van Es, Ed., no. November, Chateau de Limelette, Belgium, 2009, pp. 397–404.

[40] Harm Jan Pepping, "Singleboard Beamformer Firmware Description," ASTRON, Tech. Rep. ASTRON-RP-1429, 2014.

[41] ——, "UniBoard Beamformer module for APERTIF," ASTRON, Tech. Rep. ASTRON-RP-1291, 2012.

[42] L. Hiemstra, "Private discussion," 2014.

[43] Daniel van der Schuur, "APERTIF Beamformer Firmware Description," ASTRON, Tech. Rep. ASTRON-RP-1377, 2014.

[44] A. Parsons, D. Backer, A. Siemion, H. Chen, D. Werthimer, P. Droz, T. Filiba, J. Manley, P. McMahon, A. Parsa, D. MacMahon, and M. Wright, "A Scalable Correlator Architecture Based on Modular FPGA Hardware, Reuseable Gateware, and Data Packetization," *Publications of the Astronomical Society of the Pacific*, vol. 120, no. 873, pp. 1207–1221, Nov. 2008.

[45] "CASPER main page." [Online]. Available: https://casper.berkeley.edu/wiki/Main_Page

[46] "FEKO User Manual," no. July, 2011. [Online]. Available: http://www.feko.info

[47] "FEKO Numerical Methods," 2014. [Online]. Available: https://www.feko.info/product-detail/numerical_methods

[48] "Antenna Magnus." [Online]. Available: http://www.antennamagus.com/

[49] T. A. Milligan, *Modern Antenna Design*, 2nd ed. John Wiley & Sons., 2005.

[50] "KATADC." [Online]. Available: https://casper.berkeley.edu/wiki/KatADC

[51] "Xilinx DS100 Virtex-5 Family Overview," 2009. [Online]. Available: www.xilinx.com

[52] "ROACH," 2013. [Online]. Available: https://casper.berkeley.edu/wiki/ROACH

[53] H. Chen, P. McMahon, and A. Parsons, "Sync Pulse Usage in CASPER DSP Blocks," pp. 1–4, 2008. [Online]. Available: https://casper.berkeley.edu/wiki/Memos

[54] "RF Absorber." [Online]. Available: http://www.djmelectronics.com/rf-absorber.html

[55] J. G. B. de Vaate, E. de Lera Acedo, G. Virone, A. Jiwani, N. Razavi, F. Perini, K. Zarb-Adami, J. Monari, S. Padhi, G. Addamo, O. Peverini, S. Montebugnoli, A. Gunst, P. Hall, A. Faulkner, and A. van Ardenne, "Low frequency aperture array developments for phase 1 SKA," in *2011 XXXth URSI General Assembly and Scientific Symposium*, vol. 10. IEEE, Aug. 2011, pp. 1–4. [Online]. Available: http://dx.doi.org/10.1109/URSIGASS.2011.6051197

[56] C. A. Balanis, *Advanced Engineering Electromagnetics*, two ed. John Wiley & Sons, 2012.